NAVAL POSTGRADUATE SCHOOL
Monterey, California

DISSERTATION

OBSERVATIONAL/NUMERICAL STUDY OF THE
UPPER OCEAN RESPONSE TO HURRICANES

by

Lynn K. Shay

December 1987

Dissertation Supervisor: R. L. Elsberry

Approved for public release; Distribution Unlimited

Unclassified
TY CLASSIFICATION OF THIS PAGE

REPORT DOCUMENTATION PAGE

PORT SECURITY CLASSIFICATION nclassified	1b RESTRICTIVE MARKINGS
CURITY CLASSIFICATION AUTHORITY	3 DISTRIBUTION/AVAILABILITY OF REPORT Approved for public release; Distribution Unlimited
CLASSIFICATION/DOWNGRADING SCHEDULE	

FORMING ORGANIZATION REPORT NUMBER(S)	5. MONITORING ORGANIZATION REPORT NUMBER(S)

ME OF PERFORMING ORGANIZATION al Postgraduate School	6b. OFFICE SYMBOL (If applicable) 68	7a. NAME OF MONITORING ORGANIZATION Naval Postgraduate School
DRESS (City, State, and ZIP Code) terey, CA 93943-5000		7b. ADDRESS (City, State, and ZIP Code) Monterey, CA 93943-5000

ME OF FUNDING/SPONSORING GANIZATION R	8b. OFFICE SYMBOL (If applicable)	9. PROCUREMENT INSTRUMENT IDENTIFICATION NUMBER

DRESS (City, State, and ZIP Code)	10 SOURCE OF FUNDING NUMBERS			
	PROGRAM ELEMENT NO.	PROJECT NO.	TASK NO	WORK UNIT ACCESSION NO.

LE (Include Security Classification)
servational/Numerical Study of the Upper Ocean Response to Hurricanes

RSONAL AUTHOR(S)
ay, L. K.

PE OF REPORT .D. dissertation	13b TIME COVERED FROM _____ TO _____	14. DATE OF REPORT (Year, Month, Day) 1987 December	15. PAGE COUNT 151

PLEMENTARY NOTATION

COSATI CODES			18 SUBJECT TERMS (Continue on reverse if necessary and identify by block number)
LD	GROUP	SUB-GROUP	Near-inertial Free-surface Model Hurricanes Green's Function Normal Modes Upper Ocean Currents

STRACT (Continue on reverse if necessary and identify by block number)
The time evolution and the vertical structure of the ocean current is examined using ored current meter observations from hurricane Frederic in 1979 and data acquired by rborne eXpendable Current Profilers (AXCP) in hurricane Norbert in 1984. Energetic ar- inertial oscillations excited by the passage of these hurricanes have frequencies at are shifted by 1-20% above the local inertial frequency. These oscillations are ident in the upper 1000 m of the water column and are primarily due to the excitation low-order vertical modes.   .. .. ..
The first five free vertical modes are calculated from the Brunt-Vaisala frequency l the Sturm-Liouville problem. The horizontal velocity eigenfunctions for a flat bottom l sloping bottom are fit to the demodulated amplitudes observed in Frederic. In the xe of the hurricane, the time evolution of the depth-averaged component plus the first baroclinic modes explain about 60% and 68% of the near-inertial current variance ing the flat- and sloping-bottom models, respectively. Since the AXCP observations

TRIBUTION/AVAILABILITY OF ABSTRACT NCLASSIFIED/UNLIMITED ☐ SAME AS RPT. ☐ DTIC USERS	21. ABSTRACT SECURITY CLASSIFICATION Unclassified	
ME OF RESPONSIBLE INDIVIDUAL L. Elsberry	22b TELEPHONE (Include Area Code) (408) 646-2373	22c. OFFICE SYMBOL Code 63Es

RM 1473, 84 MAR   83 APR edition may be used until exhausted.   SECURITY CLASSIFICATION OF THIS PAGE
All other editions are obsolete
☆ U.S. Government Printing Office: 1986—606-24.
1
Unclassified

19.

were acquired in the high wind regime, the near-inertial response for the 3-dimensional velocities is simulated by projecting a hurricane-like wind stress field onto the first five baroclinic modes. The divergence and curl of the wind stress are also convolved with the Green's function (J_o) for each baroclinic mode. In hurricane Norbert, the sum of the first four near-inertial modes explains over 70% of the observed current variance on the right side of the storm track. Most of this current variability can be accounted for by the curl terms, although the divergent and Ekman terms do contribute to the observed current variance within 30-60 km of the storm center. The effect of the stress divergence and Ekman terms on the ocean current response rapidly diminished after one inertial period.

The role of depth-averaged velocity component is assessed using numerical simulations from a 17-level, primitive equation model with a free-surface boundary condition. The slope of the sea-surface induces a depth-averaged velocity that is comparable to that observed in Frederic. The simulated modal amplitudes for the first two baroclinic modes are within 10-15% of those derived from the Frederic data.

Observational/Numerical Study of the Upper Ocean Response to
Hurricanes

by

Lynn K. Shay
B.S., Florida Institute of Technology, 1976
M.S., Naval Postgraduate School, 1983

Submitted in partial fulfillment of the
requirements for the degree of

DOCTOR OF PHILOSOPHY IN PHYSICAL OCEANOGRAPHY

from the

NAVAL POSTGRADUATE SCHOOL
December 1987

ABSTRACT

The time evolution and the vertical structure of the ocean current is examined using moored current meter observations from hurricane Frederic in 1979 and data acquired by Airborne eXpendable Current Profilers (AXCP) in hurricane Norbert in 1984. Energetic near-inertial oscillations excited by the passage of these hurricanes have frequencies that are shifted by 1-20 % above the local inertial frequency. These oscillations are evident in the upper 1000 m of the water column and are primarily due to the excitation of low-order vertical modes.

The first five free vertical modes are calculated from the Brunt-Väisälä frequency and the Sturm-Liouville problem. The horizontal velocity eigenfunctions for a flat bottom and sloping bottom are fit to the demodulated amplitudes observed in Frederic. In the wake of the hurricane, the time evolution of the depth-averaged component plus the first two baroclinic modes explain about 60% and 68% of the near-inertial current variance using the flat- and sloping-bottom models, respectively. Since the AXCP observations were acquired in the high wind regime, the near-inertial response for the 3-dimensional velocities is simulated by projecting a hurricane-like wind stress field onto the first five baroclinic modes. The divergence and curl of the wind stress are also convolved with the Green's function (J_o) for each baroclinic mode. In hurricane Norbert, the sum of the first four near-inertial modes explains over 70 % of the observed current variance on the right side of the storm track. Most of this current variability can be accounted for by the curl terms, although the divergent and Ekman terms do contribute to the observed current variance within 30-60 km of the storm center. The effect of the stress divergence and Ekman terms on the ocean current response rapidly diminishes after one inertial period.

The role of the depth-averaged velocity component is assessed using numerical simulations from a 17-level, primitive equation model with a free-surface boundary condition. The slope of the sea-surface induces a depth-averaged velocity that is comparable to that observed in Frederic. The simulated modal amplitudes for the first two baroclinic modes are within 10-15 % of those derived from the Frederic data.

4

TABLE OF CONTENTS

LIST OF TABLES

LIST OF FIGURES

11

ACKNOWLEDGEMENTS

LIST OF SYMBOLS

A	vertical aspect ratio
α_n	inverse deformation radius of mode n
α_s	slope of the bottom
$\alpha.$	thermal expansion coefficient of seawater
b	thickness of the thermocline
C	air/sea aspect ratio
CW	clockwise rotating current amplitudes
CCW	counter-clockwise rotating current amplitudes
c_0	phase speed of the barotropic mode
c_n	phase speed of the nth baroclinic mode and eigenvalue
c_{gv}	vertical group velocity
c_{gh}	horizontal group velocity
d/dt	$\partial/\partial t + u\partial/\partial x + v\partial/\partial y$
∇	$i\partial/\partial x + j\partial/\partial y + k\partial/\partial z$
∇_h	$i\partial/\partial x + j\partial/\partial y$
D	depth of the ocean
Δ	change in a variable
KE	kinetic energy
ε_o	external Froude number (U_h/c_o)
ε_1	internal Froude number (U_h/c_1)
ξ	WKBJ stretched vertical (z) coordinate
f	Coriolis parameter
f_{eff}	effective frequency shift ($\zeta/2f$)
g'	reduced gravity ($g\Delta\rho/\rho_o$)
h	mixed layer depth
IP	inertial period
J_o	Green's function for the hyperbolic (baroclinic) operator
k_r	non-dimensional storm speed (Greatbatch)
l	wavenumber in along-track direction
k	wavenumber in cross-track direction
L	horizontal scale of the wind stress curl ($2R_{max}$)

16

Λ	wavelength of the nth mode in a fixed frame
λ	wavelength of the nth free mode moving with the storm
M	mixed layer Burger number $(1 + 1/S^2)\varepsilon_1$
n	mode number
N^2	Brunt-Väisälä frequency $(-g'/\Delta z)$
η	isopycnal displacment
η_s	sea-surface height perturbations
p	total pressure
p'	pressure perturbation
p_a	atmospheric pressure at the sea surface
p_n	horizontal structure function of the pressure
R	Rossby number
r_n	radius where the wind stress curl is zero
R_{max}	radius of maximum wind
φ_n	eigenfunction of Sturm-Liouville problem
Θ	CW-phase of the wave
ρ	ocean density
ρ_o	reference ocean density
S	large scale limit (L/α_1^{-1})
S_t	non-dimensional storm translational speed (Price)
σ	angular wave frequency
T	thermocline Burger number
T'	temperature perturbation
τ_m	maximum hurricane wind stress
u'	wave-induced horizontal velocity
u_*	atmospheric friction velocity (τ/ρ_a)
δv	velocity shear $(\Delta v/\Delta z)$
U_h	storm translation speed
ζ	vorticity of the mean flow $(\partial v/\partial x - \partial u/\partial y)$
u_n	horizontal structure function of the east-component of velocity
v_n	horizontal structure function of the north-component of velocity
w	vertical velocity
w_n	horizontal structure function of the vertical velocity

I. INTRODUCTION

" Thought breeds thought."............ Thoreau, *Walden*

As a hurricane moves over the ocean, the wind stress curl causes a divergence of upper ocean currents from the storm track, which induces the upwelling of cooler water from the thermocline. The magnitude of the ocean's thermal and momentum response depends on the scales of the applied atmospheric forcing and the initial ocean stratification. Farther back in the wake (rear) of the hurricane, the upper ocean currents converge toward the storm track and surface water is downwelled into the thermocline. This pattern of upwelling and downwelling regimes in the wake is thus part of a time-dependent, three-dimensional response problem. According to linear theory, the horizontal wavelength between these cells is proportional to the product of the translation speed of the hurricane and the local inertial period.

The strong atmospheric forcing and the displacement of the isopycnals during the upwelling and downwelling phase tend to excite large-scale internal waves in the upper ocean. As these waves propagate away from the storm track, the ocean's mass and current fields adjust geostrophically to form a ridge along the periphery of the upwelling and downwelling regimes. This ridge in the isopycnals and the internal waves are part of the ocean's baroclinic response to the passage of a hurricane. The wind stress curl also causes a mean mass divergence that depresses the sea-surface height relative to the undisturbed height. This depression in the free surface height, which is called a barotropic trough, can excite a depth-independent component.

The forced internal waves are characterized as having large horizontal wavelengths, fairly signficant amplitudes, periods close to the inertial period and are clockwise rotating. Because the period of the forced waves is so close to the inertial period, these oscillations are also called near-inertial. Early theoretical studies suggested that the near-inertial response to strong atmospheric forcing should be confined to the upper ocean layers (200-300 m). However, recent observations indicate that the excitation of the large scale near-inertial waves are associated with low-order modes that have vertical wavelengths of 500-1000 m.

This study focuses on the time-dependent, three-dimensional current response to hurricane passage. The emphasis here is on isolating the near-inertial response from

the ocean currents and expanding these data into free or forced modes to better understand the vertical structure of the ocean response to strong atmospheric forcing.

A. BACKGROUND

1. Observations

One of the first experiments to examine the ocean's thermal response to hurricane forcing was during the passage of hurricane Hilda in 1964 (Leipper, 1967). Several hydrographic cruises were made to measure the ocean's temperature changes using mechanical bathythermographs. The upwelling of cooler water from the thermocline was the dominant mechanism along the track, whereas mixing and downwelling appeared to have been important outside R_{max}. These measurements prompted numerical and analytical investigations of the oceanic response to hurricane passage (O'Brien and Reid, 1967; Geisler, 1970). More recently, Black (1983) completed an exhaustive 10-year study of ocean temperature observations acquired during the passage of hurricanes. Each hurricane was classified according to the storm translation speed (U_h), storm intensity (τ_m), radius of maximum winds (R_{max}), initial ocean stratification and mixed layer depth. One key feature that is relevant to this study is that the horizontal wavelength in the thermocline wake was typically 100 - 200 km instead of 300 - 500 km as predicted by linear theory (Geisler, 1970). Furthermore, Black showed that the thermal response directly under the hurricane, which he could observe with Airborne eXpendable BathyThermographs (AXBT), was different from that previously observed in the wake. Specifically he found a cresent-shaped pattern of maximum temperature decreases of 1-4 °C that extended from the right side of the storm to the wake region. There have also been several instances in which the ocean's thermal response to hurricane passage has been observed by NOAA data buoys (Withee and Johnson, 1976; Johnson and Renwick, 1981). These buoys have measured meteorological parameters as well as ocean temperatures, which has contributed to the understanding of the upper ocean thermal response.

Observations of the ocean's current response to the passage of hurricanes have been from a few "fortuitous" encounters with current meter moorings that have been deployed in support of other experiments. The ocean current speeds have maximum amplitudes approaching 100 cm/s and oscillate with frequencies close to the inertial period (IP). For example, moored current meter measurements on the continental shelf of the mid-Atlantic Bight (100 m) revealed fairly strong current oscillations of 50 - 70 cm/s (Mayer *et al.*, 1981). A deeper ocean response was observed during the

19

passage of hurricanes Allen (Brooks, 1983) and Frederic (Shay and Elsberry, 1987a). Maximum current amplitudes at 700 m were about 15 cm/s in the Allen measurements, whereas the ocean current amplitudes at 950 m in Frederic were 10 cm/s. These sets of measurements were acquired on the right side of the storm track where the maximum ocean current response is predicted to be the largest (Chang and Anthes, 1978; Price, 1983). None of the current meter moorings had sufficient vertical resolution to observe higher order baroclinic modes in the ocean response to hurricanes.

Vertical profiles of the ocean current were acquired during the passage of midlatitude atmospheric fronts in the Storm Response and Transfer Experiment (STREX) using eXpendable Current Profilers (XCP) (D'Asaro, 1985). Maximum ocean currents were about 25 cm/s in the mixed layer, and the current vector rotated clockwise with depth in the upper 800 m. This clockwise polarization with depth is associated with near-inertial processes and internal waves with large vertical wavelengths O(1000 m). These large vertical wavelengths are part of the low-mode dominance as energy propagates into the interior of the fluid from the wind-forced mixed layer. Lai and Sanford (1986) provided a more complete picture of the vertical structure of the currents in the far-field after the passage of hurricanes Carrie and Dawn in 1972. Moored current meter measurements were augmented with velocity profiles in the "Site D" region. They found that over 50 % of the current variability could be described using the first three baroclinic modes.

For the first time, Airborne eXpendable Current Profilers (AXCP's) were deployed within the directly forced or near-field (the positive wind stress curl region) during the passage of hurricanes Norbert and Josephine in 1984 and during hurricane Gloria in 1985 (Sanford et al., 1987). Not since the early experiments of Leipper (1967) has there been such an organized scientific effort to study the ocean response to hurricane passage. For the first time, these AXCP's provide a synoptic snapshot of the ocean currents with sufficient vertical resolution to adequately describe the hurricane-forced baroclinic structure. As will be demonstrated below (see also Shay et al., 1987b) over 70 % of the observed current variance in the profiles acquired during hurricane Norbert can be explained by a sum of only the first four, forced baroclinic modes.

2. **Analytical and Numerical Modelling**

As the storm translation speed increases, linear theory shows that the ocean response is primarily baroclinic and is associated with the dispersion of near-inertial waves in the wake (Geisler, 1970). Within the framework of linear dynamics, one of

the crucial nondimensional numbers in the oceanic response problem is the Froude number, the ratio of the translation speed (U_h) to the first baroclinic mode internal wave phase speed (c_1) (Geisler, 1970). If this Froude number is greater (less) than unity, the oceanic response is predominately baroclinic (barotropic).

In his linear, two-layer treatment of the forced response, Geisler (1970) simulated the horizontal structure of the vertical velocity field in the wake of the hurricane by convolving a Green's function (Bessel function) with the wind stress curl. Upwelling and downwelling regions in the vertical velocity have a wavelength (Λ) that is proportional to the product of the storm translation speed (U_h) and the inertial period (IP). Geisler did not explicitly address the structure of the horizontal current regime. Geisler points out that it is unlikely that linear theory can describe the ocean response in the directly-forced or near-field region. Therefore, extensions of existing theory are necessary to facilitate direct comparisons with the AXCP observations beneath the hurricane, and to compare the linear theory to simulations from sophisticated primitive equation models.

The wind stress curl induces a semi-permanent baroclinic ridge along the sides of the upwelling and downwelling regions. Because this baroclinic ridge may remain in the wake for long times following hurricane passage, previous observational and theoretical studies have only considered the wind stress curl to be important. However, the typical inflow angles in a hurricane are 15-30 °, which induce divergence of the wind stress (Holland, 1987). During the passage of hurricane Belle, Mayer *et al.* (1981) demonstrated that the spatial scales of the wind stress curl and divergence were similar and that the magnitude of the stress divergence was about 30 % of that of the wind stress curl magnitude. This suggests that the divergence effects in the forcing should be examined to see if they contribute to the ocean response beneath the hurricane.

One of the consequences of linear theory is that the oceanic response can be characterized by the first few baroclinic modes in the far-field (Gill, 1984). As indicated above, this theoretical prediction appears to be verified by the observations of Lai and Sanford (1986) in the far-field of hurricanes Carrie and Dawn. They suggest that 75% of the baroclinic, near-inertial energy is contained in the first three bottom-slope modes as compared to 55% of the energy in the first three flat-bottom modes. Unfortunately, their observations do not measure the barotropic response to hurricane passage. The Shay and Elsberry (1987a) study of the near-inertial oscillations observed during the passage of hurricane Frederic was limited to a depth-averaged and first two baroclinic modes because of the number of current meters in the vertical.

21

Since the baroclinic modes have different rates of horizontal phase velocities, it is of interest to study their time evolution. Gill (1984) demonstrated that if the storm scale of the wind stress curl exceeds the deformation radius (which is called the large-scale limit) of the first baroclinic mode, there will be a time scale over which each mode will develop a $\pi/2$ phase difference with the remainder of the solution in the mixed layer. This large-scale limit uses a criterion that is not fundamentally different from the Froude number of Geisler (1970). A second-order effect is that slight increases in the mixed layer kinetic energy will occur on the time scale required for the first baroclinic mode to become in-phase with higher order modes. Kundu and Thomson (1985) noted this beating effect in numerical simulations of the near-inertial response to a moving atmospheric front. As will be shown below (see also Shay and Elsberry, 1987a), the time evolution of the near-inertial modal amplitudes from hurricane Frederic agrees rather well with these baroclinic time scales for modes 1 and 2. Moreover, amplitudes of the first two baroclinic modes in the mixed layer are within 10-15 % of those expected from linear theory.

The nonlinear, baroclinic response in the ocean to a moving hurricane was numerically simulated by Chang and Anthes (1978), Adamec et al. (1981), Price (1981, 1983), Hopkins (1982), and Greatbatch (1983). In these studies, a rigid lid was imposed at the sea surface, which eliminated the barotropic or depth-averaged response. For example, Hopkins (1982) simulated the dynamic response to a hurricane moving at the same translation speed as Frederic and found that the simulated mixed layer currents agreed well with the Shay (1983) observations. However, the computed magnitudes of the currents in the thermocline were too small. It is believed that one source of the discrepancies between the simulations and the observations is the neglect of the depth-averaged mode by imposing a rigid lid in the model. Although Brooks (1983) noted a significant depth-averaged current in the wake of hurricane Allen, the contribution of the depth-averaged component to the total observed variance was not estimated. It will also be demonstrated below (following Shay and Elsberry, 1987a) that the near-inertial response to hurricane Frederic contains a depth-independent component of 7-10 cm/s that contributes to about 15-20 % of the near-inertial variability.

Both the ocean's baroclinic and barotropic response to hurricane forcing was numerically simulated for the first time by Chang (1985). An inherent problem of free-surface modelling is that the barotropic mode propagates so quickly that very small

model time steps must be used. To circumvent this computational problem, Chang (1985) introduced a mode-splitting technique into the free-surface, primitive equation model. The simulated current response extended from the surface to 2000 m with a barotropic component of about 10-15 cm/s. New numerical model experiments with the Chang model will be used in this study.

B. OBJECTIVE AND KEY ISSUES

The objective of this study is to understand the vertical structure of the near-inertial ocean current response to the passage of hurricanes. The emphasis here is to blend observations from hurricanes Frederic and Norbert with analytical and numerical models. Thus, the near-inertial response is studied in terms of kinematics, energetics, normal modes and wavelengths using free modes and forced models in the far-field and near-field, respectively.

A synopsis of the moored ocean current observations acquired in hurricane Frederic in 1979 and current profiles from AXCP's deployed in hurricane Norbert is given in Chapter II. Brief descriptions of the hurricanes are also given in terms of the scales of the applied atmospheric forcing.

In Chapter III, the near-inertial response to a moving hurricane is examined within the framework of linear theory by extending the two-layer model of Geisler (1970) to a continuously stratified fluid and superposing the wind stress onto the first five baroclinic modes as in Kundu and Thomson (1985). In this treatment, analytical expressions are derived for the horizontal current velocities as well as the vertical velocity for the "near-field". The effects of the wind stress and the wind stress divergence are also included in the analysis.

The time-evolution of the near-inertial response to hurricane Frederic is examined using the moored current meter arrays in Chapter IV. The behavior of the vertical structure of the first two baroclinic modes is compared to predictions from linear theory (Gill, 1984). The effect of bottom topography on the near-inertial current response is also explored using the Lai and Sanford (1986) model.

The complete vertical structure of the near-inertial response in the near-field is addressed in Chapter V using the vertical profiles of ocean currents and temperatures acquired in hurricane Norbert. The near-inertial current profiles are expanded in terms of the forced dynamical modes using the theories derived in Chapter III. The effect of the stress divergence and wind stress are shown to be important in the direct forcing region as well as the wind stress curl.

A controversial issue raised by the Frederic observations (Shay and Elsberry, 1987a) is the role of the depth-averaged circulations induced by the passage of hurricanes. The role of the depth-averaged current and the baroclinic structure is assessed in Chapter VI using the numerical simulations from a 17-level, primitive equation model (Chang, 1985). Since the model current simulations appear to have sufficient veracity, the model simulations are compared to the Frederic observations. Finally, concluding statements are given in Chapter VII.

II. DATA DESCRIPTION

A. HURRICANE FREDERIC

1. Storm Track and Wind Field

The storm track shown in Fig. 2.1 is based on the post-season analysis of hurricane Frederic's movement across the Gulf of Mexico (Hebert, 1979). Because of the intensity of Frederic, reconnaissance aircraft constantly monitored the storm. Hurricane Frederic reached maximum wind speeds within 80 to 130 km west of the array sites about 21 Universal Time Coordinate (UTC) 12 September (the time of closest approach). Visible satellite imagery at 20 UTC 12 September clearly delineated a well-developed eye of 50 to 60 km in diameter. The translational speed of the hurricane (U_h) as it approached the Gulf Coast was 6 - 7 m/s, which was larger than the internal wave phase speed of the first baroclinic mode ($c_1 = 3$ m/s).
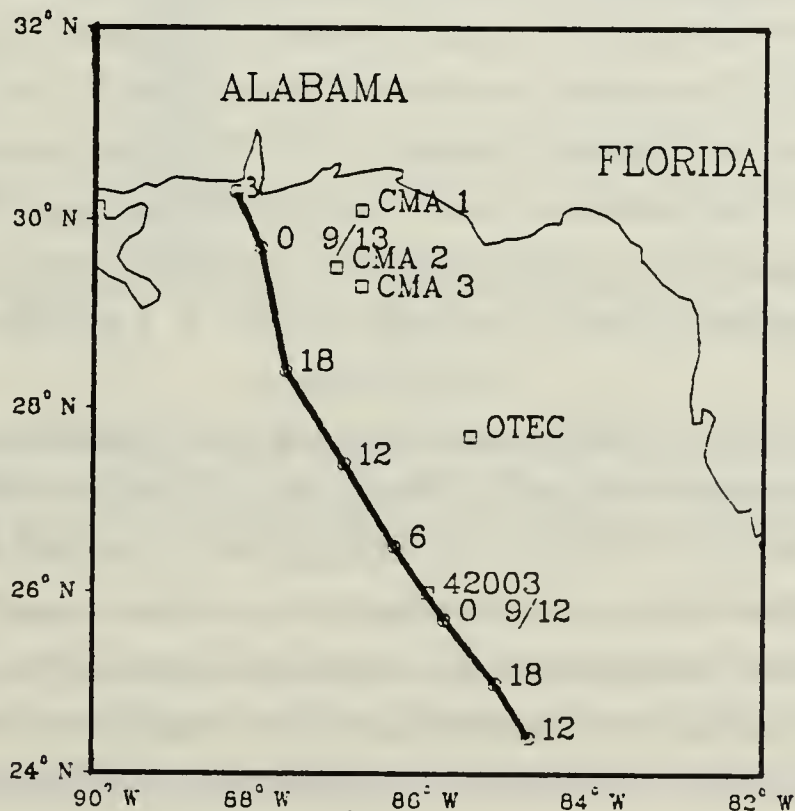
Figure 2.1 The path (circles) of hurricane Frederic in the northern Gulf of Mexico (Hebert, 1979) beginning 12 UTC 11 Sept. and ending 03 UTC 13 Sept. 1979. The boxes depict the NOAA data buoy 42003, the OTEC and three NAVOCEANO (CMA 1,2 and 3) current meter arrays.

25

Powell (1982) documented the boundary layer wind field associated with hurricane Frederic using data collected by two NOAA aircraft. The wind speeds ranged between 48 and 58 m/s at a radius of maximum wind (R_{max}) between 27 and 33 km. The curl of the wind stress field deduced from these values has a horizontal scale of about 60 km. Other wind reports confirm these intensities as Frederic made landfall (Hebert, 1979).

Marine winds (Fig. 2.2) were also measured by NOAA Buoy 42003 (Johnson and Renwick, 1981). The eye clearly passed over the buoy, as indicated by the minimum in the wind field as the direction changed from 40 to 200 °T, with a corresponding decrease in pressure to 959 millibars (mb). The maximum (near-surface) wind speeds at this location never exceeded 35 m/s. Using a Rankine vortex and a maximum wind stress of 3.5 N/m^2 in Frederic (Black, 1983), the maximum curl is 220 10^{-7} cm/s^2 with a $2R_{max}$ scale of 60 km. For an inflow angle of 20 °, the maximum stress convergence is about 75 x 10 $^{-7}$ cm/s^2.

2. Current Meter Data and Measurement Errors

The local variations in the bottom topography of the DeSoto Canyon (Fig. 2.3) are approximately parallel and normal to the coast at Current Meter Array (CMA)2 and CMA3. For example, north-south flow at CMA2 is in the cross-shelf direction, but it is in the along-shelf direction at CMA3. Since the storm moved on a northward track and the isobaths are nearly east-west and north-south along the northern and eastern rim of the DeSoto Canyon, the ocean current data are represented in a standard Cartesian coordinate system (i.e., y positive north and x positive east).

Seventeen Aanderaa RCM-5 current meters were deployed on five moored, taut-wire, subsurface arrays[1] (Fig. 2.3) in depths ranging from 100 - 500 m in the northern Gulf of Mexico. The arrays were designed with a flotation device one meter above the near-surface current meter (nominally 20 m). These current meters sampled ocean current, direction and temperature at 10 minute intervals. Two current meter arrays (CMA2 and CMA3) were deployed on adjacent sides of the DeSoto Canyon. The other NAVOCEANO mooring was on the continental shelf in about 100 m of water.

---

[1]Since the positions (but not the observations) of CMA6 and CMA9 remain classified confidential, the results from these arrays are only compared to the results from the unclassified arrays CMA1, CMA2 and CMA3.

26
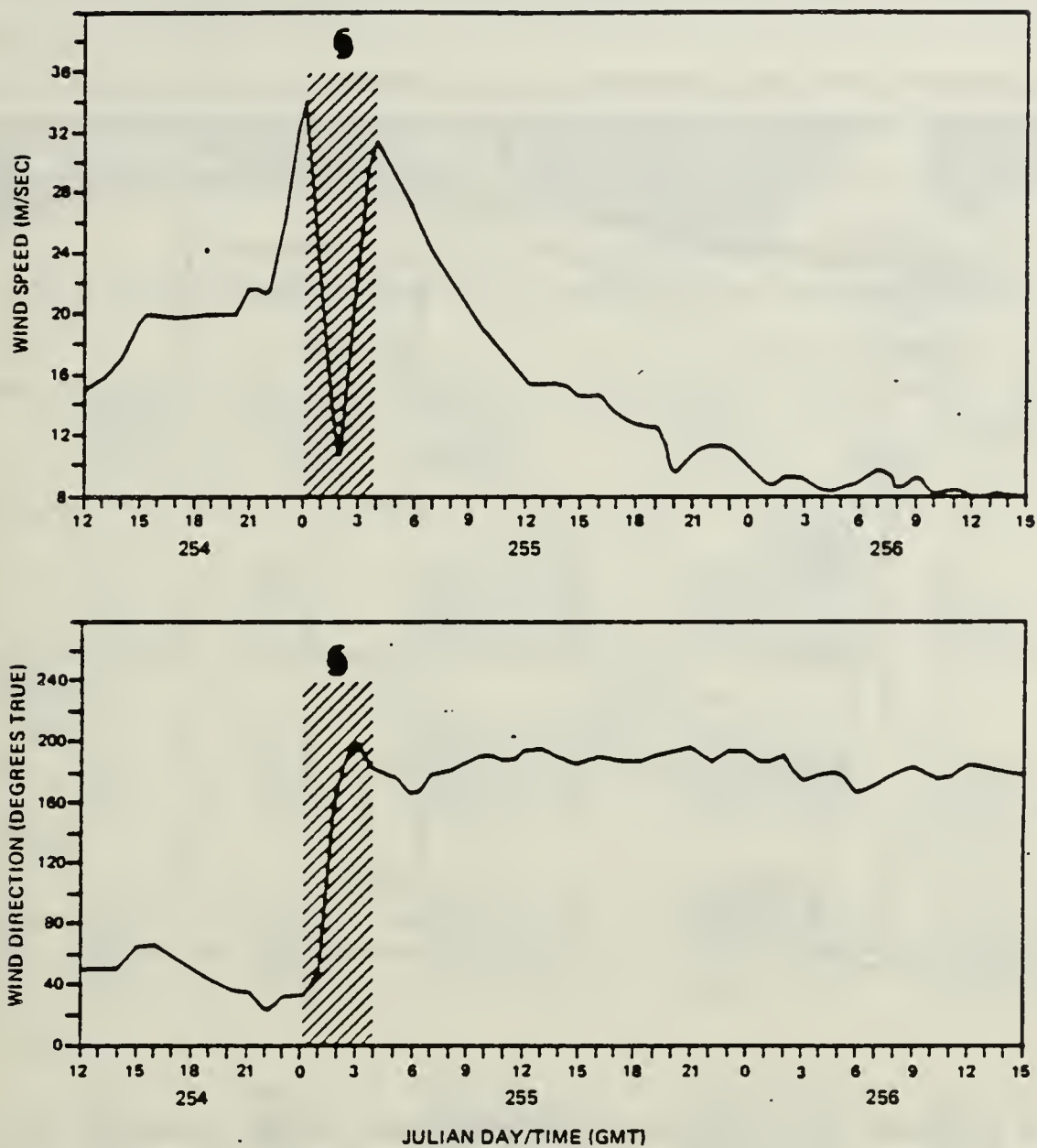
Figure 2.2 Wind speed (upper) and direction (lower) measured by NOAA buoy 42003 from 12 UTC 11 Sept. to 15 UTC 13 Sept. 1979. The hatched area depicts the period when the data buoy was in the eye of the hurricane (Johnson and Renwick, 1981).

The OTEC buoy was located 210 km south-southeast of the DeSoto Canyon in 1050 m of water and was instrumented with four Aanderaa RCM-5 current meters that measured ocean current speed, direction, temperature and pressure at 20 minute intervals (Starr and Maul, 1982). Table 1 is a synopsis of the observations for the entire period of deployment, which extends from the end of July to mid-October. The storm period is from a few days prior to hurricane passage to the end of the deployment period (mid-October).

27
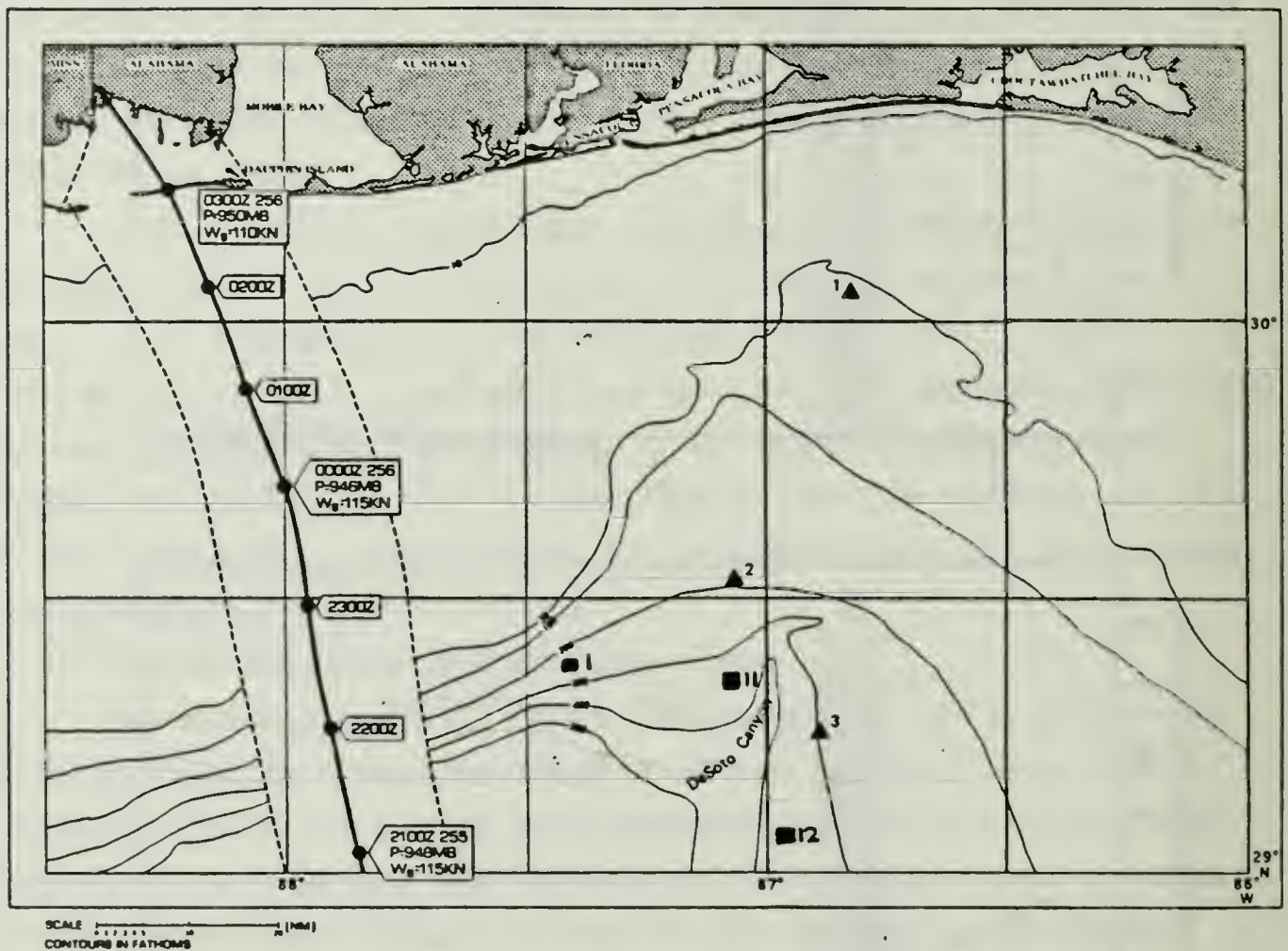
Figure 2.3 Positions of NAVOCEANO current meter arrays (triangles) and AXBT observations 1,11 and 12 (rectangles) of Black (1983) relative to the track of hurricane Frederic. The minimum pressure and maximum wind speeds at hourly intervals are taken from Hebert (1979). The radius of the maximum winds is indicated by the dashed lines parallel to the storm track and the depth contours (fathoms) are shown as solid lines.

Because the Savonius rotors were eventually lost from all the current meters in the mixed layer due to the large current speeds, the lengths of the time series are not equal. Furthermore, these large current speeds have not been corrected for rotor pumping. Current speeds recorded by Savonius type meters can be altered by horizontal and vertical mooring motion induced by the surface gravity wave field. Other sources of errors in the Aanderaa current meters are the instantaneous directional sampling, lack of vector averaging, and the slow vane response that

28

contaminates the spectrum of wave motions, especially at the higher frequencies (Beardsley *et al.*, 1977).

TABLE 1

A synopsis of moored current meter observations
in hurricane Frederic based on the Universal Time Coordinate (UTC).

Meter Depth (m)	Record Length (days)	Start Time (UTC)	End Time (UTC)	Variables
CMA1				
21	47.3	1600 26 Jul.	0000 12 Sep.	u,v
49	62.5	1600 26 Jul.	0600 27 Sep.	u,v
64	57.1	1600 26 Jul.	1920 21 Sep.	u,v,T
92*	61.2	1600 26 Jul.	2040 25 Sep.	u,v,T
CMA2				
19	64.9	1800 26 Jul.	1650 29 Sep.	u,v
179	65.3	1800 26 Jul.	0100 30 Sep.	u,v,T
324	66.0	1800 26 Jul.	1900 29 Sep.	u,v,T
CMA3				
21	57.3	1330 31 Jul.	2200 26 Sep.	u,v
251	68.5	1330 31 Jul.	0100 8 Oct.	u,v,T
437	68.2	1330 31 Jul.	1730 7 Oct.	u,v,T
457	64.4	1330 31 Jul.	0000 4 Oct.	u,v,T
CMA6				
20	64.9	2000 26 Jul.	1715 29 Sep.	u,v
180	61.3	2000 26 Jul.	0410 26 Sep.	u,v,T
330	65.6	2000 26 Jul.	1150 1 Oct.	u,v,T
CMA9				
20	60.3	1640 31 Jul.	0000 29 Sep.	u,v
250	71.4	1640 31 Jul.	0320 11 Oct.	u,v,T
500	64.2	1640 31 Jul.	2250 3 Oct.	u,v,T
OTEC				
100	30.00	0007 1 Sep.	0007 1 Oct.	u,v,T,p
232	30.00	0007 1 Sep.	0007 1 Oct.	u,v,T,p
546	30.00	0007 1 Sep.	0007 1 Oct.	u,v,T,p
950	30.00	0007 1 Sep.	0007 1 Oct.	u,v,T,p

* time clock synchronization problems

The pressure records on the OTEC current meters indicate that the mooring was tilted by the hurricane-forced currents. The maximum tilt of the mooring based on the vertical displacements measured by the pressure sensors was about 15 $^\circ$. The current meters at 100, 232, 546 and 950 m were displaced downward by 65, 55, 30 and 0 m, respectively. The corresponding changes in temperature were about 2.6, 1.5, 0.75 and 0.25 $^\circ$ C.

On the NAVOCEANO arrays, the temperature changes due to vertical displacements are not known as pressure sensors were not included. An upper bound on the mooring motion can be estimated from the AXBT and moored temperature measurements. The NAVOCEANO arrays were designed to withstand currents in excess of 150 cm/s with a maximum tilt of 10° (C. Robinson, 1986, personal communication). The maximum vertical displacement in the 10° tilt case would be 14 m and cause the maximum depth of the upper current meter to be 35 m. The AXBT observations (see Fig. 2.3) indicated that the threshold temperature of the thermistors (21.5 $^\circ$ C) was located between 75 to 80 m depth. Because the mixed layer (initial depth of 21 m) temperatures were always above this threshold, the mixed layer current meters must have always remained above 80 m. A 60 m displacement of this instrument would correspond to a tilt of the moored array by 21.5 $^\circ$ from the vertical. The corresponding maximum displacement is about 160 m in the horizontal. Thus, the horizontal displacements of the mooring array accounts for very little of the observed temperature variations.

Since the mixed layer current measurements were made at 21 m below the surface, the forced surface gravity wave field will induce a current that will contaminate the current measurements (Halpern et al., 1974). The magnitude of the surface wave current is estimated from

$$u_s = (\pi H_s/L_s)^2 c_o e^{k_s z} , \tag{2.1}$$

where H_s is the significant wave height, L_s is the dominant wavelength of the surface gravity wave field, k_s is the significant wavenumber $(2\pi/L_s)$ and c_o is the deep water, surface gravity wave phase speed $(g/k_s)^{1/2}$. The wavelength is estimated from the wave period (T_s) using the relationship $(g/2\pi)T_s^2$. The significant wave height and period of the surface gravity waves were estimated at NOAA data buoy 42003 (Johnson and Renwick, 1981). The significant wave height at the buoy was approximately 8 m with a period of 10 s . The current induced by the surface wave is estimated to be about 40 cm/s, which then decreases exponentially with an e-folding depth of 25 m. Since the

mooring may have been tilting a maximum of 15 °, the magnitude of the surface wave current ranged from 18 and 6 cm/s for tilts of the mooring from 0 - 15 °, respectively.

The time-dependent behavior of the currents induced by surface waves was studied theoretically by Hasselman (1970) and Pollard (1970). As the surface waves increase over the first quarter of an inertial period, the current begins to rotate inertially due to the influence of the Coriolis force. During the passage of storms (time scales of $1/f$), surface waves can induce fairly large inertial oscillations (Hasselman, 1970). The estimated surface wave current component was removed from the mixed layer record by forming a time series of an inertially rotating current with amplitudes of 10 cm/s and phase of $\pi/2$ starting 5 h before the time of closest approach. The adjustment for the surface wave current was e-folded over 4 IP's following the maximum value at CMA3. The phase of the forced near-inertial waves was preserved after the removal of this current.

3. Temperature Profiles

The AXBT data were collected by Black (1983) during and subsequent to the passage of Frederic in the area of the DeSoto Canyon (Fig. 2.3). Since the AXBT's only extended to 200 m, it was necessary to extrapolate the vertical temperature profiles to the bottom using the moored temperature data. For example, the temperature observations at CMA2 were used to extrapolate the thermal profile at AXBT station 1 (Fig. 2.4a). The vertical temperature gradients below 200 m were also checked against CTD data collected in support of OTEC during the summer of 1977 (Thomas et al., 1979) to insure consistency.

The mixed layer temperatures were not available because the ocean temperatures exceeded the maximum temperature resolvable by the thermistors. The AXBT observations of Black (1983) indicate that the mixed layer cooled by 3°C and deepened to 40-50 m in the DeSoto Canyon region. The mixed layer temperatures after storm passage were 25-26 °C. The vertical profiles of the Brunt-Väisälä frequency (N) were estimated using the AXBT data and climatological temperature-salinity (T-S) relationships (Wahl and Teague, 1983). A time-averaged value (Fig. 2.4b) was computed at each depth using the N^2 profiles.

B.   HURRICANE NORBERT

1. Storm Track and Wind Field

During the summer of 1984, the Hurricane Research Division (HRD) of NOAA conducted Planetary Boundary Layer Experiments in hurricane Norbert. Prior
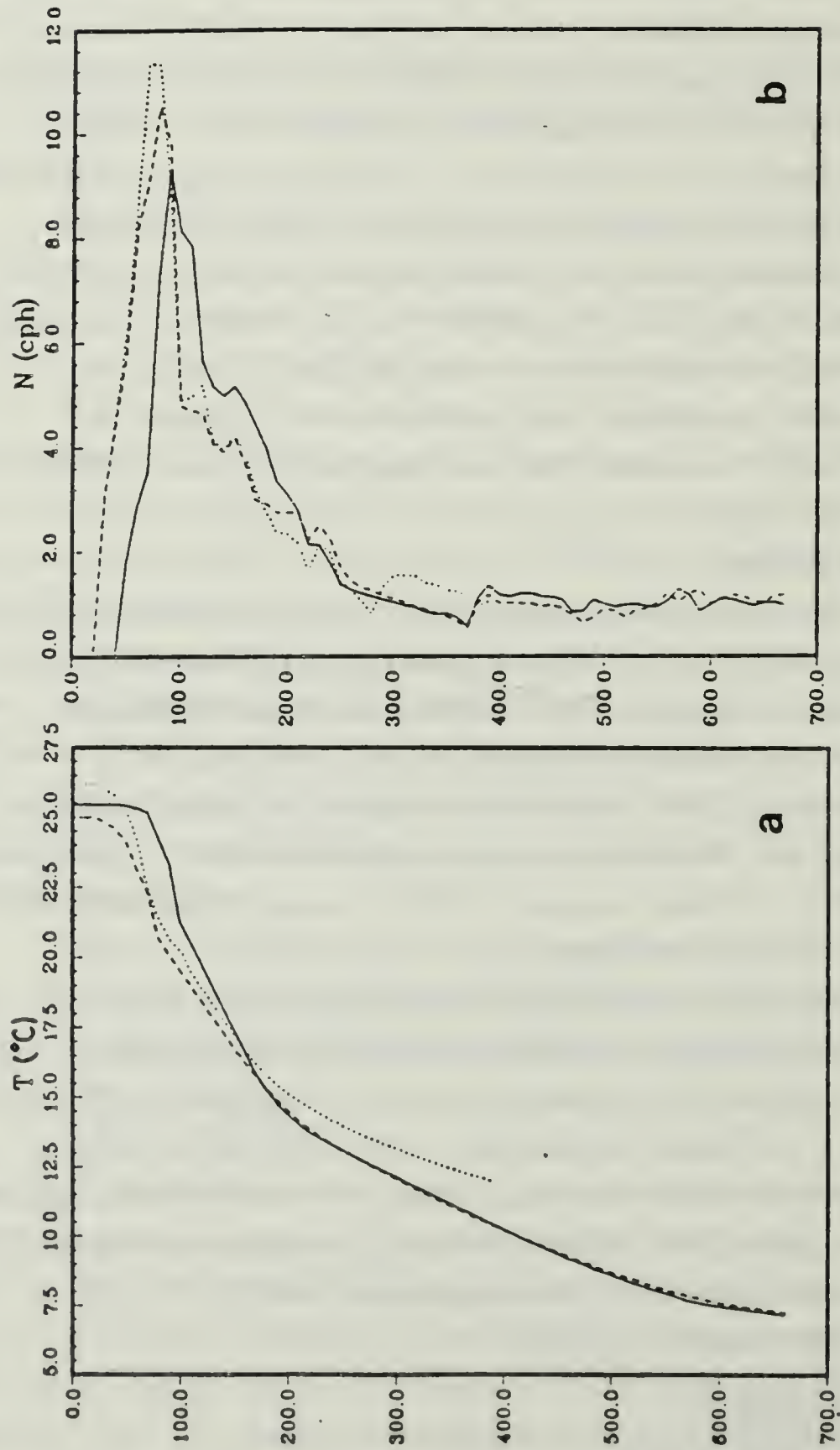
Figure 2.4 Profiles of a) temperature (°C) and b) Brunt-Väisälä frequency (cph) from three AXBT locations shown in Fig. 2.3: 1) 29.43 °N, 87.42 °W (dotted) ; 11) 29.33 °N, 87.11 °W (solid); and 12) 29.08 °N, 86.94 °W (dashed).

to the AXCP research flights (Sanford *et al.*, 1987), tropical storm Norbert was slowly developing into a hurricane (Fig. 2.5). Norbert slowly drifted in a cyclonic path for about 6 days. On 21 September, tropical storm Norbert was classified as a hurricane with a minimum central pressure of 950 mb and maximum winds of 115 knots. Notice the recurving path of hurricane Norbert between the 21 and 23 September just before the AXCP research flights on 23 and 24 September. The translation speed (U_h) for hurricane Norbert was only 3.8 - 4.2 m/s in the vicinity of the AXCP research flight and the vortex was moving at 320°T. The AXCP portion of the experiment was conducted by Horizon Marine with the support of a consortium of oil companies under the project Ocean Response to Hurricane Joint Industry Program (ORHJIP). The locations of the 16 AXCP's that were successfully deployed in hurricane Norbert are shown in Fig. 2.6.
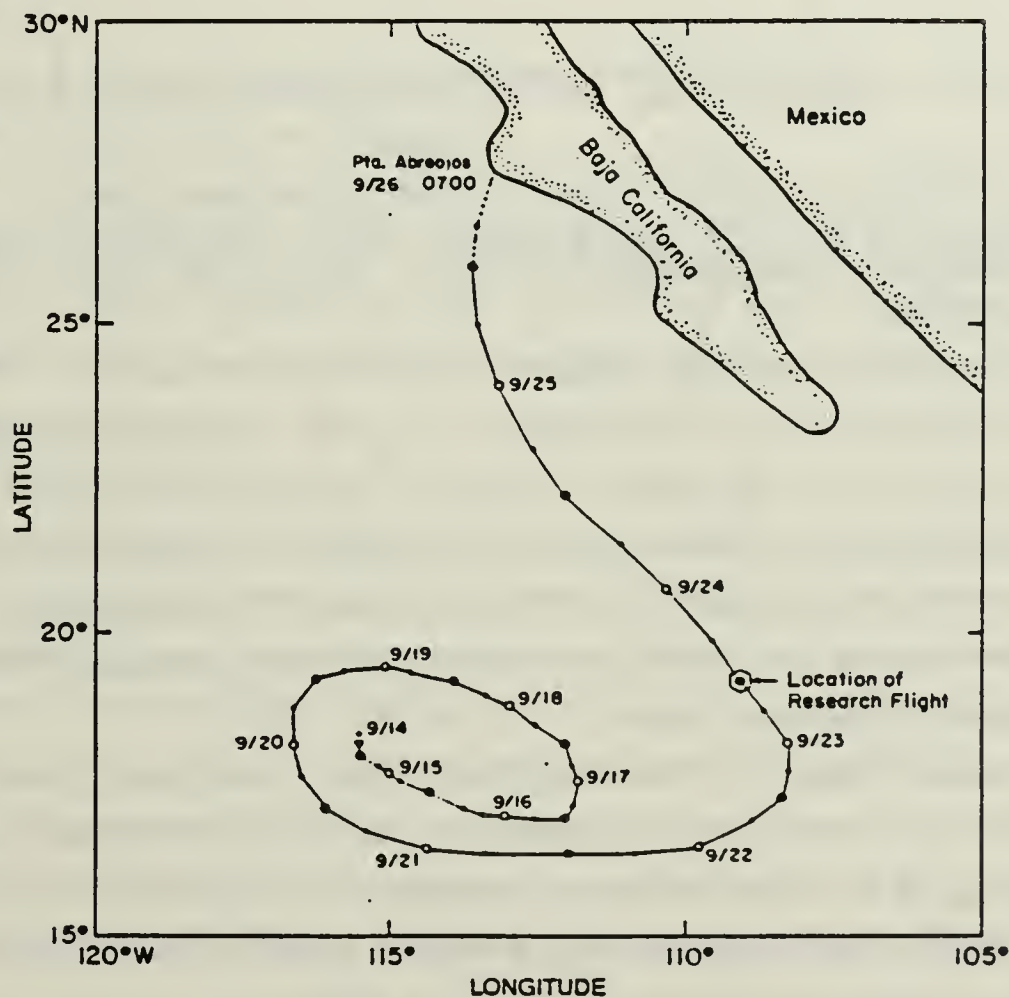
Figure 2.5 Track of hurricane Norbert and the location of the AXCP research flights (from Sanford *et al.* 1987). The Norbert AXCP flight started at 2230 UTC 23 September and ended at 0130 UTC 24 September 1984.
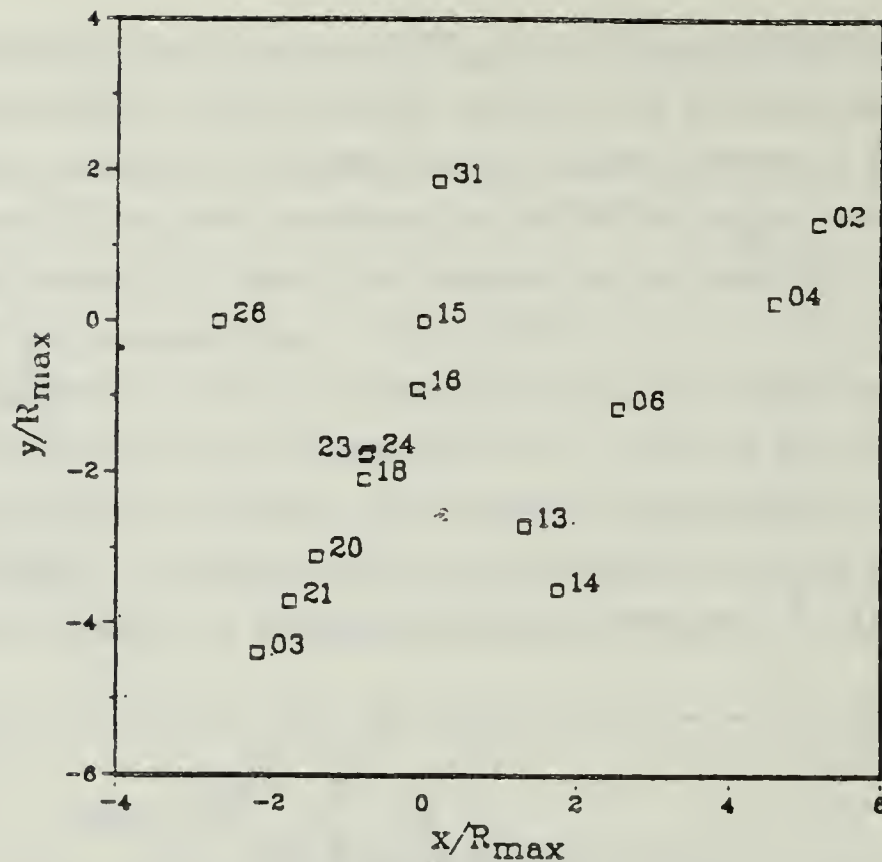
Figure 2.6 Positions of AXCP's (probe number is indicated) relative to storm center of Norbert (19°N, 109 °W, moving towards 320°T). The spatial distribution of the AXCP's is scaled nondimensionally in terms of the primary radii of maximum winds (R_{max}) of (34 km).

There are primary and secondary wind maxima that lead to a double-eye type structure as shown in Fig. 2.7 (Willoughby *et al.*, 1984). The winds in Norbert exceeded 50 m/s at both the primary (34 km) and secondary (17 km) radii of maximum wind, and the central pressure was in the 950 mb range. Outside the secondary maximum, the wind decreases to 20 m/s over 120 km. The maximum wind stress estimated for Norbert is 4.4 N/m² at the primary radius of maximum winds.

2. **Model of the Wind Stress**

Because of the lack of wind profiles in a few of the quadrants and the double-eye structure that would add considerable complexity in the wind field, a simpler distribution of the wind is treated here. A common representation of a hurricane wind stress distribution is the Rankine vortex given by Chang and Anthes (1978). The tangential and radial wind stress components are given by

$$\tau_r, \tau_\theta = -|\tau_{rm}|, |\tau_{\theta m}| \ f(\theta) \begin{cases} \dfrac{r}{R_{max}} & r < R_{max}, \\[2ex] \dfrac{(R_{out}-r)}{(R_{out}-R_{max})} & R_{max} < r < R_{out}, \\[2ex] 0 & r > R_{out}, \end{cases} \qquad (2.2)$$

34
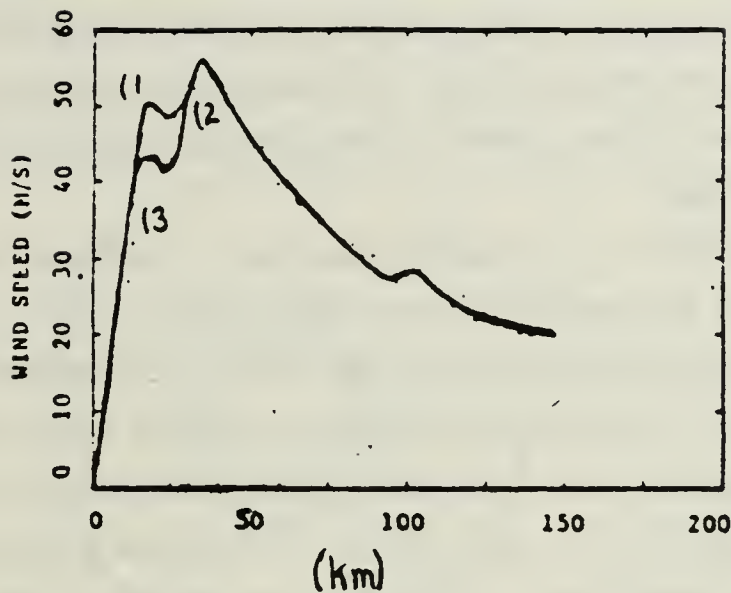
Figure 2.7 Flight-level wind profiles from hurricane Norbert (solid) in the right-rear (1), right (2) and (3) right-front quadrants.

where R_{max} (radius of maximum wind) = 30 km and R_{out} (radius to the outer edge of the hurricane) = 300 km. Typical values for $|\tau_r|$ and $|\tau_\theta|$ used in the Chang and Anthes experiments were 1.0 and 3.0 Nt/m^2, respectively. The function $f(\theta)$ represents the asymmetric factor given by

$$f(\theta) = 1.0 + b \cos(\theta) \quad ,$$

where b=0 for the symmetric and b=0.3 for the asymmetric case. This wind stress distribution is input as a body force in the mixed layer. The effect of the asymmetric storm was to displace the maximum ocean currents and temperature perturbations even farther to the right of the track. This rightward bias produced by the asymmetric storm was small compared to the bias induced by nonlinearities in the Chang and Anthes model. In this research, the storm is assumed to be symmetric (b=0). The region of strong positive vorticity (wind stress curl) is confined within $\pm$ R_{max} and corresponds to a length scale of $2R_{max}$ (68 km for Norbert and 60 km for Frederic).

The wind stress curl exceeds 280 x 10^{-7} cm/s^2 in the core of the hurricane (Fig. 2.8). The near-field is defined as the region where the wind stress curl is greater than zero which is approximately at a r_n = $3R_{max}$. Since both hurricanes had inflow angles of about 20 °, the maximum divergence of the wind stress is about 50 x 10^{-7} cm/s^2. Even larger inflow angles may be needed for the growth and maintenance of the tropical cyclone as it moves over the ocean (Holland, 1987). If the inflow angle

35

was 30 °, the maximum divergence would be 100 x 10 $^{-7}$ cm/s^2. Thus, the divergence term within a few radii of maximum winds may be important, as noted by Mayer *et al.* (1981) during the passage of hurricane Belle. The length scales associated with the divergence are comparable to those associated with the wind stress curl (2 R$_{max}$).

3. Ocean Current Data

A total of 16 AXCP's were sucessfully deployed in hurricane Norbert from the NOAA aircraft (Table 2). The profilers sample relative currents once every revolution (about 0.3 m in the vertical) with rms errors in the velocity measurements of about 1 cm/s (Sanford *et al.*, 1982). Since the profiler measures vertical current shear, the currents are integrated upward from a reference value as described in Sanford *et al.* (1987). The fast probes descend at a rate of 4.5 m/s and sample currents and temperatures in the upper 1000-1500 m of the ocean, whereas the slower probes (2.2 m/s) provide excellent resolution of the ocean response in the upper ocean (typically 200-250 m).

Upper ocean current measurements are contaminated by storm-generated surface waves that induce a current. Sanford *et al.* (1987) developed a least-squares model to account for the currents associated with surface wave, which for the u-component is

$$u_m = \left[A_u \cos(\sigma t) + B_u \sin(\sigma t) \right] e^{kz} , \qquad (2.3)$$

where A_u and B_u are the least squares coefficients (Table 3) for the u-velocity component, σ is the surface wave frequency ($2\pi/T$), T is wave period (nominally 5-15 s), k is the wavenumber (σ^2/g) and g is the acceleration of gravity. The least-squares model for the v-component of velocity is similar to the above expression. Equation (2.3) is analogous to (2.1) except that the amplitudes of the surface waves (H$_s$,L$_s$) are replaced by the amplitudes of the surface wave currents (A$_u$,B$_u$). Although the dominant waves appear to fit the model quite well (Fig. 2.9), some surface wave signals may remain in the profiles after removal of the surface wave currents, which may possibly contaminate the vertical structure analyses below. However, a second fit to the profiles after the dominant surface wave is removed reveals very small amplitudes in most of the profiles.

The velocity profiles are low-pass filtered every 3 m by a simple running mean (10 values) for subsequent processing. The AXCP profiles contain vertical structure that has not been previously available from moored current meter arrays (Mayer *et al.*, 1981; Brooks, 1983; Shay and Elsberry, 1987a). For the first time, the vertical structure
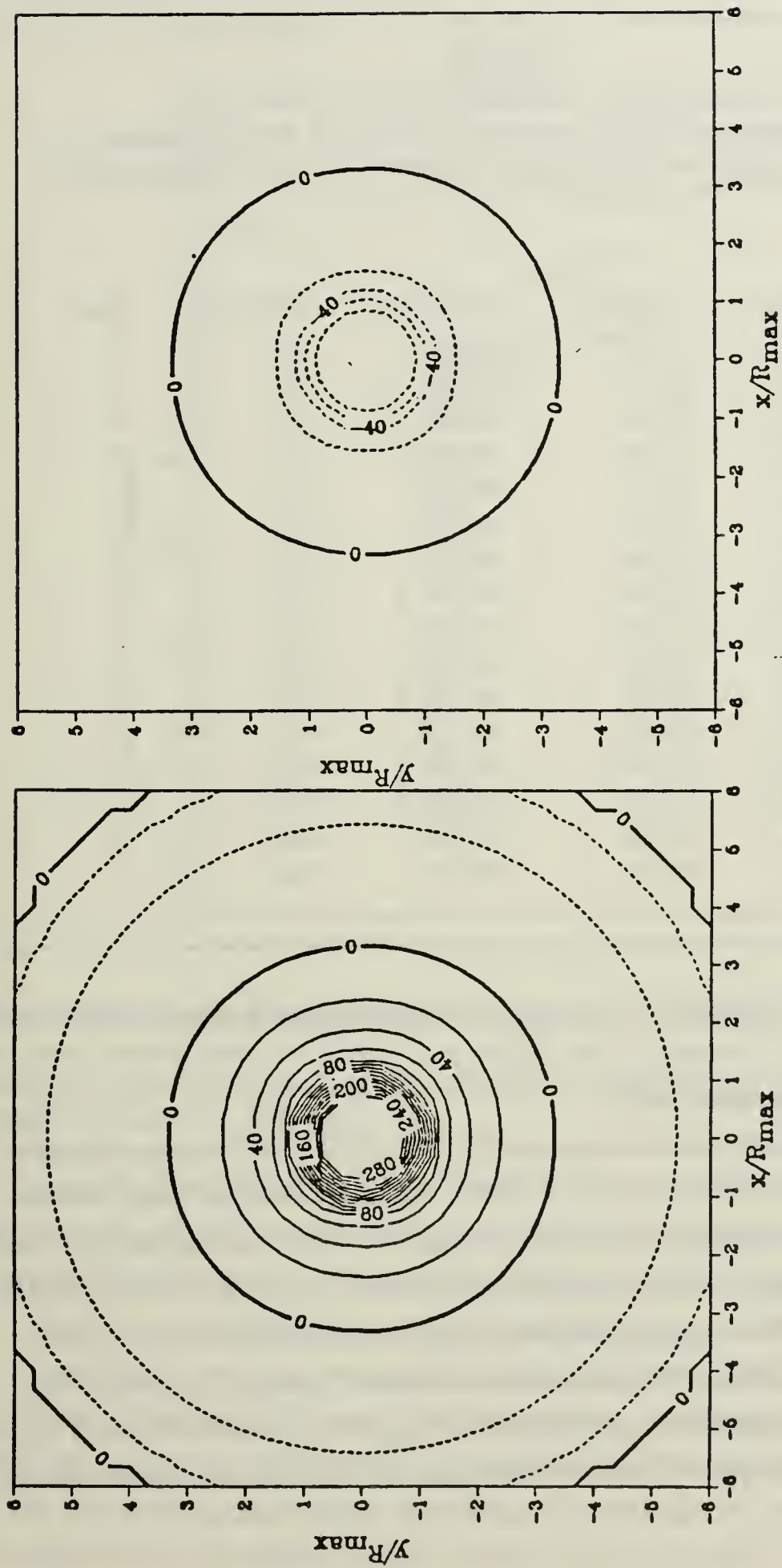
Figure 2.8 Idealized wind stress curl (left) and divergence (right) in units of $10^{-7} cm/s^2$ for hurricane Norbert based on a Rankine vortex and observed storm parameters. The abscissa and ordinate axes are scaled in terms of R_{max} relative to the storm center as in Fig. 2.6.

TABLE 2

A synopsis of AXCP observations acquired during hurricane
Norbert for the fast (F:4.5 m/s) and slow (S: 2.2 m/s) falling probes.

Probe	Time (JD)	Lat.(N)	Long.(W)	W_s(m/s)	Rate
N02	266.947	20 34	108 12	25.3	F
N04	266.950	20 15	108 08	32.0	F
N06	266.966	19 36	108 20	35.2	F
N13	266.983	19 04	108 19	34.4	F
N14	266.985	18 58	108 04	28.1	F
N16	267.000	19 12	108 57	33.0	S
N18	267.004	18 50	108 53	40.2	F
N20	267.007	18 31	108 50	29.7	F
N21	267.009	18 20	108 48	24.0	F
N03	267.012	18 07	108 46	21.8	F
N15	267.021	19 25	109 05	5.7	S
N22	267.021	18 53	108 56	41.9	S
N23	267.022	18 54	108 56	42.7	S
N24	267.022	18 55	108 56	42.9	S
N26	267.041	18 56	109 41	30.2	F
N31	267.058	19 49	109 24	38.0	F

of the ocean current response to hurricanes can be examined in detail with no vertical aliasing.

4. Ocean Temperature Data

The ocean temperatures measured by the AXCP's are low-pass filtered in a similar manner to the velocity data (Fig. 2.10). Mixed layer depths range between 18 to more than 40 m within the domain of hurricane Norbert. The temperature profile from AXCP 20 indicates a large temperature decrease of 11 $^\circ$C in the upper 100 m of the water column. This strong gradient impedes the vertical penetration of the hurricane-induced response by limiting the entrainment velocity. Vertical scales associated with the temperature gradients in the upper thermocline are about 160 m, below which the temperature decreases uniformly with depth in the domain influenced by hurricane Norbert.
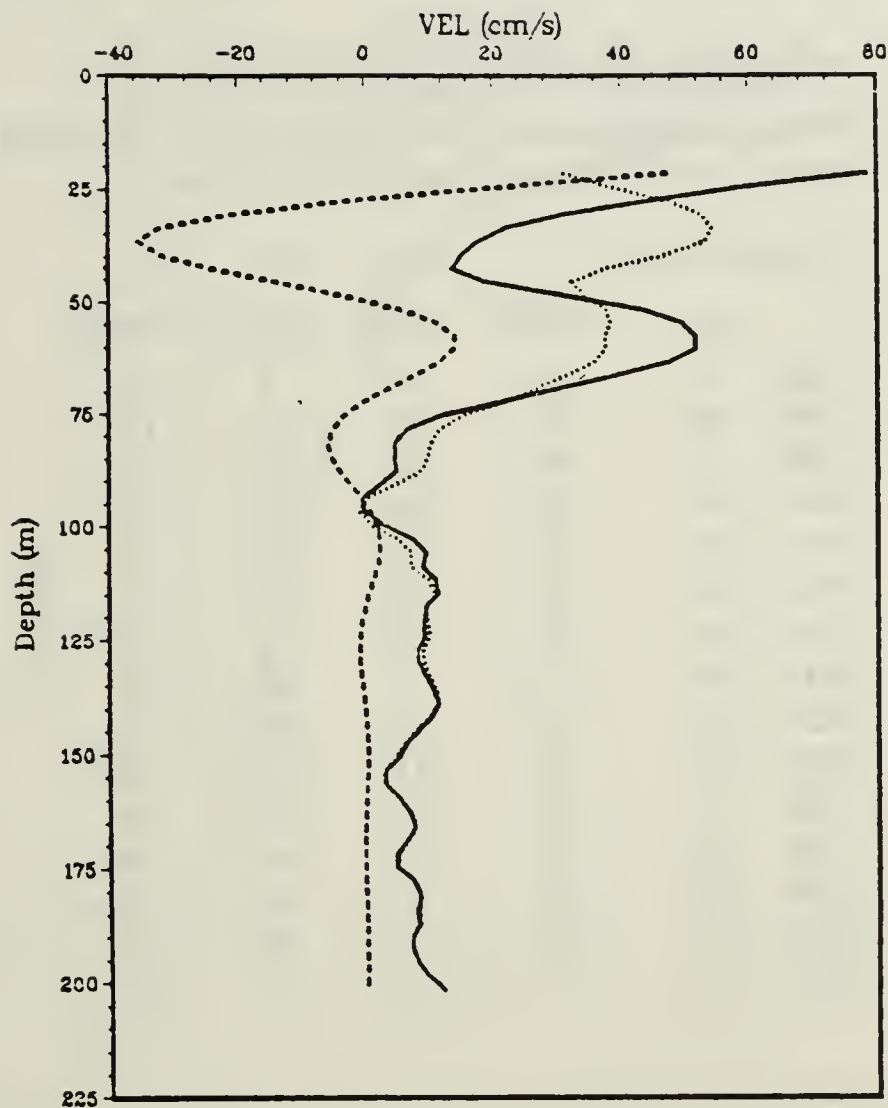
Figure 2.9 Original (solid), surface wave (dashed) and residual (dotted) v-component current (cm/s) profile from 20 to 200 m for AXCP 04 in Norbert. The residual current is obtained by removing the surface wave component from the observed current profile, which begins at about 21 m depth.

The vertical profiles of the Brunt-Väisälä frequency in Fig. 2.11 are estimated from the temperature data using climatological temperature-salinity (T-S) relationships, which may induce an error in the Brunt-Väisälä frequency of 0.-0.2 cph over a depth range of 100-450 m (Wahl and Teague, 1983). Only a few temperature and salinity profiles are available to estimate density structure in the eastern North Pacific where the AXCP's were deployed. The spatially-averaged Brunt-Väisälä frequency increased to about 8 cph at the base of the mixed layer and decreased to 2 cph at 200 m and below. The stratification suggests that the vertical penetration of the ocean's thermal response induced by the hurricane may be limited to the upper ocean.

39

TABLE 3

Periods and velocity amplitudes for the u
(A_u,B_u) and v (A_v,B_v) components of the surface wave in hurricane Norbert,
based on the model of (Sanford et al., 1987).

Probe	Period (s)	A_u (cm/s)	B_u (cm/s)	A_v (cm/s)	B_v (cm/s)
N02	9	24	11	4	-61
N04	10	24.	-35	-95	122
N06	9	-95	26	113	196
N13	9	-51	-39	-26	-43
N14	10	-70	-50	12	-58
N15	10	-25	-13	-5	5
N16	11	-19	-5	8	-29
N18	10	-129	1	20	-51
N20	10	-50	43	50	81
N21	10	-37	-31	-123	-13
N03	9	-25	-76	-21	38
N23	10	-57	13	65	28
N24	10	-67	-1	9	-46
N26	9	-147	117	-68	-60
N31	9	0	107	5	84

C. AIR/SEA PARAMETERS

The initial oceanic response (spin-up) to hurricanes is governed by the parameters (Table 4) of the applied atmospheric forcing (Geisler, 1970; Price, 1984; Greatbatch, 1984). The translation speeds (U_h) for hurricanes Norbert and Frederic are only 4 - 6.5 m/s. Hurricane Norbert is characterized as a slowly moving storm. The maximum wind stress estimated for Norbert is 4.4 N/m^2 at the primary radius of maximum winds. By contrast, Frederic is a fast moving storm at 6.5 m/s, but it is less intense than Norbert with a τ_m of 3.5 N/m^2.

1. Ocean Parameters and Nondimensional Framework

The initial mixed layer depths (h) in the region of hurricanes Norbert and Frederic were 30 to 45 m (see Table 4), and thicknesses of the thermocline (b) were 160 and 200 m, respectively. Both storms were located in the subtropics and had *Inertial*
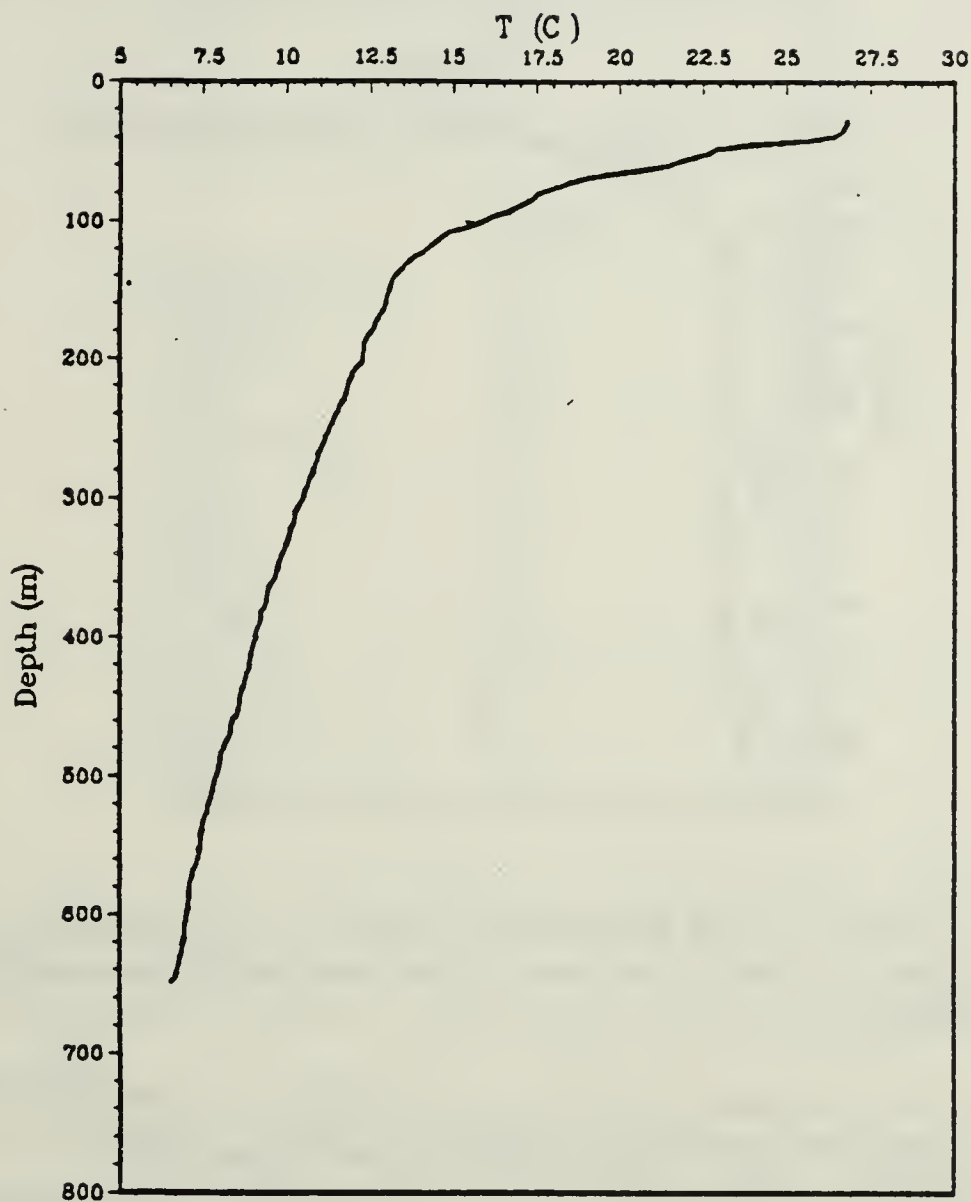
Figure 2.10 Low-pass filtered temperature (°C) profile from hurricane Norbert AXCP 20.

Period's (IP) ranging from a day (Frederic) to a day and a half (Norbert). The first mode internal wave phase speeds are 2.1 and 3 m/s based on the spatially-averaged Brunt-Väisälä frequency and the Sturm-Liouville problem (Chap. III).

The important nondimensional numbers in the ocean spin-up to hurricane passage are associated with comparisons between atmospheric and oceanic scales. Geisler (1970) demonstrated that if the internal Froude number $(U_h/c_1) > (<) 1$, the oceanic response is primarily baroclinic (barotropic). Within this framework, a mixed baroclinic and barotropic response may be expected since the Froude number is about 1.9 in Norbert and 2.2 in Frederic. Another relevant scale intercomparison is the ratio

41
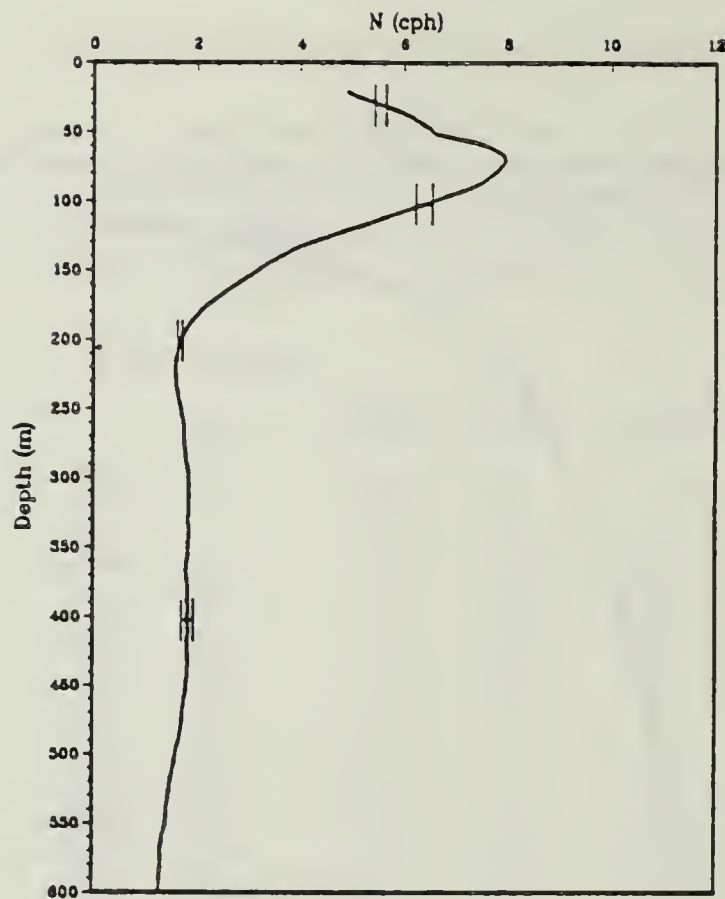
Figure 2.11 Spatially-averaged Brunt-Väisälä frequency (cph) profile from Norbert with the 95% confidence intervals at selected depths based on the bootstrap method and a normal distribution.

of the scale of the wind stress curl ($2R_{max}$) to the deformation radius of the first baroclinic mode $(a_1)^{-1}$ (c_1/f). If this nondimensional forcing scale is $>>$ ($<$) 1, the response is primarily baroclinic (barotropic). As with the internal Froude number, a mixed baroclinic-barotropic response is expected in these cases. Although the internal Froude number and nondimensional forcing scale are not fundamentally different, the nondimensional forcing scale is also the large-scale limit for which linear theory should apply (Gill, 1984). Veronis (1956) showed that if the ratio of the nondimensional forcing scale to the Froude number is larger than π, the internal wave amplitude associated with the baroclinic response will be large. Because this ratio (nondimensional time scale) is $O(1)$ in both of these storms, the amplitude of the internal waves is smaller in Norbert because Frederic is considered to be a fast moving storm.

The Geisler (1970) wavelength (Λ) is shown to be a function of storm translational speed, the Coriolis parameter, and the phase speed of the first baroclinic mode (c_1):

42

TABLE 4

Air/sea parameters for hurricanes Norbert and Frederic

	Norbert	Frederic
R_{max} (km)	34	30
τ (Nt/m^2)	4.4	3.5
U_h (m/s)	4.0	6.5
h (m)	40	45
g$'$ x 10^{-3}(m/s)	3.7	2.2
b (m)	160	200
IP (d)	1.5	1.0
c_1 (m/s)	2.1	3.
Λ (km)	444	520
U_h/c_1 (F)	1.9	2.2
α_1^{-1}(km)	44	41
$2R_{max}/\alpha_1^{-1}$ (S)	1.5	1.5
(S)/(F)	0.9	1.7

$$\Lambda = (2\pi/f)(U_h^2 - c_1^2)^{1/2} \quad .$$

According to the above expression, as c_1 approaches U_h the wavelength of the near-inertial waves decreases.

Price (1984) discussed the importance of the nondimensional numbers derived from the air-sea parameters. An important nondimensional number in the mixed layer is the Burger number M, which is a measure of the importance of the horizontal pressure gradients

$$M = \frac{(1 + 1/S_t^2)g'h}{(2R_{max}f)^2}, \tag{2.4}$$

where S_t is the nondimensional storm speed ($U_h/2R_{max}f$), h is the mixed layer depth and g$'$ is the reduced gravity. The Burger number measures the importance of the horizontal pressure gradient that couples the mixed layer to the thermocline and causes a vertical transfer of energy from the wind-forced mixed layer into the thermocline. Price (1984) suggests that the shift in the frequency above the local inertial frequency (blue-shift) is equal to one half of the mixed layer Burger number or Δv. The Burger numbers in Frederic and Norbert are approximately 0.08 and 0.36. The associated frequency shifts of the near-inertial response should be 0.04 and 0.18 above the local

43

inertial frequency. These shifts are within the near-inertial frequency band of 0.9f-1.2f (Kunze, 1985; Mooers, 1975). Thus, the near-inertial frequencies will be set to 1.18f for hurricane Norbert in light of the excellent agreement between the estimated Burger numbers and the frequency of the near-inertial oscillations in hurricane Frederic (Shay and Elsberry, 1987a).

Price (1984) also defined two other important nondimensional parameters in the response problem:

$$S_t = \frac{U_h}{R_{max}f} \quad \text{and}$$

$$T = \frac{Mb}{h_1},$$

where b is the thermocline thickness, and g' is the reduced gravity (Table 4). These non-dimensional numbers are given in Table 5, using the air-sea parameters specified in Table 4. The velocity in the thermocline depends on the nondimensional storm speed, S_t. For a symmetric storm, S_t is a ratio of the inertial time scale f^{-1} to the advective time scale of the storm, $2R_{max}/U_h$. Alternatively, S_t may be intrepreted as a ratio of the along-track wavelength U_h/f to the scale of the wind stress curl $(2R_{max})$. The parameter S_t is also the nondimensional number k_r derived by Greatbatch (1984) who refers to k_r as the translational storm scale (ratio of the local inertial period to the time scale over which the forcing acts). The translational time scale can also be thought of as the time available for mixing.

A storm with $S_t < 1$ is considered to be slow whereas a fast storm has $S_t > 2$. According to the Price criterion, Norbert would be considered a fast storm $(S_t = 2.1)$, whereas Frederic is a transition storm since $S_t = 1.7$. The value of S_t also sets the amplitude ratio between the geostrophic and wave components associated with the near-inertial response. According to Black's (1983) classification of storms, Norbert would be considered a fast moving storm $(U_h > 3 \text{ m/s})$. If the advective time scale is long compared to the inertial time scale $(S_t < 1$, i.e. a slow storm), the atmospheric forcing can decrease the amount of kinetic energy in the mixed layer in the rear half of the storm (Price, 1984).

The thermocline Burger number T represents the vertical phase difference of the velocity across the thermocline. This vertical phase difference provides the mechanism for the vertical propagation of energy from the wind-forced mixed layer to

TABLE 5

Nondimensional numbers from Price (1984) model
versus hurricanes Frederic and Norbert.

#	Price	Frederic	Norbert
S_t	1.42	1.74	2.07
M	0.12	0.08	0.36
T	0.48	0.27	2.10
R*	0.28	0.18	0.47
A	0.01	0.1	0.01

A is the vertical aspect ratio
R is the Rossby number
* These values were computed using the expression $\tau/h_1 U_h f$
  because Price (1983) includes a constant of 3 in the numerator.

the thermocline. As T approaches unity, the waves in the hurricane wake penetrate
through the first few cycles with very little phase change in the velocity. The values of
2.1 and 0.9 for the Norbert indicate that fairly large phase changes through the
thermocline should be expected. The thermocline Burger number of 0.27 for Frederic is
consistent with a deeper oceanic response that was demonstrated by Shay and Elsberry
(1987a). The phase changes through the thermocline derived from the Frederic data
are small with a simple vertical structure.

Finally, the Rossby numbers, estimated from the expression $\tau/h_1 U_h f$ are
approximately 0.2 for Frederic and 0.5 for Norbert. Chang and Anthes (1978) noted
that the nonlinearities decrease as the translational speed of the storm increases, which
is consistent with the scaling arguments of Greatbatch (1984).

2. **Velocity and Temperature Scales**

Price (1984) scales the maximum wind-driven velocity as $\tau R_{max}/h_1 U_h$. Using
the values in Table 4, the predicted wind-driven velocity for the hurricane Frederic case
would be 38-40 cm/s, which is roughly one-half of the observed near-inertial velocity in
the mixed layer (see Fig. 4.5). Similarly, the estimated mixed layer velocity during the
passage of Norbert is about half the maximum observed velocity of 1.1 m/s (see Fig.
5.2). The vertical velocity, which scales as τ/U_h, is generally larger for the slower
moving storms because the amount of vorticity injected into the mixed layer increases.

For example, the predicted vertical velocity scale for Frederic is 0.06 cm/s as compared to 0.08 cm/s for Norbert. Furthermore, increased vertical advection in the thermocline displaces the isopycnals upward for the slowly moving storms. The isopycnal displacement τ/fU_h predicted for hurricane Norbert is about 18 m, as compared to 8 m predicted for Frederic. Price refers to this phenomenon as "inertial pumping," which is a time-dependent manifestation of Ekman pumping by virtue of τ/L arguments (dimensions of the wind stress curl). It should be noted that the time available for mixing also increases for slower moving storms, although mixed layer depth changes due to mixing are counteracted by upwelling induced by the curl of the wind stress.

The Greatbatch (1984) scaling arguments are also used to estimate the wind-driven velocity, vertical velocity and temperature perturbations. As in the Price treatment, the Greatbatch scaling arguments apply to the area bounded by $r < R_{max}$, and the maximum wind-driven velocities are scaled as $\tau L/h_1 U_h$, where L is the scale of the wind stress curl ($2R_{max}$). Thus, the maximum horizontal velocities are 0.8 and 1 m/s in hurricanes Frederic and Norbert, respectively. The Price and Greatbatch formulation of the wind-driven velocity (u′) differ by a factor of two in the numerator because Price uses the radius of maximum winds R_{max}, which is half the scale of the wind stress curl (L) used by Greatbatch. Thus, the predicted Frederic velocity is nearly equal to the observed near-inertial velocity, although these data were obtained at about $4 R_{max}$. The vertical velocities (w′) are scaled similarly in both models and are consistent with the observations in the Frederic and Norbert storms of 0.06 and 0.08 cm/s.

The predicted temperature changes in the thermocline, according to the Greatbatch scaling, are about 0.2 °C, which is equal to the lower limit of the observed demodulated, near-inertial temperature changes (see Fig. 4.2) during the passage of hurricane Frederic. If the wind stress is nearly doubled, which is consistent with the Black (1983) estimates for Frederic, the temperature changes are doubled and are closer to agreement with the observations. The predicted temperature changes at 200 m in hurricane Norbert are 0.5 °C.

III. LINEAR THEORY

The near-inertial velocity profiles acquired during the passage Norbert indicate the presence of large vertical wavelength oscillations. Since these profiles were deployed within the direct forcing regime or near-field ($r_n < 3R_{max}$), it is clear that vertical structure is not just a sum of the free baroclinic modes as in the far-field (Gill, 1984). Thus, the current profiles should be examined in terms of the applied atmospheric forcing, especially for comparisons in the near-field.

A.   GOVERNING EQUATIONS

The two-layer model of Geisler (1970) is extended to a continuously stratified ocean with a Brunt-Väisälä frequency ($N(z)$) following the development by Kundu and Thomson (1985), who treated an atmospheric front rather than a tropical cyclone. Geisler (1970) only derived expressions for the vertical velocity and isopycnal displacement. Because the AXCP's measure the baroclinic components of the horizontal velocities, expressions for the structure of the horizontal velocities are derived here. It is assumed that the ocean is linear and inviscid with a mixed layer depth h where $N(z) = 0$. The governing equations for a Boussinesq fluid are

$$\frac{\partial u}{\partial t} - fv = -\frac{1}{\rho_o}\frac{\partial p}{\partial x} + X, \tag{3.1}$$

$$\frac{\partial v}{\partial t} + fu = -\frac{1}{\rho_o}\frac{\partial p}{\partial y} + Y, \tag{3.2}$$

$$\frac{\partial u}{\partial x} + \frac{\partial v}{\partial y} + \frac{\partial w}{\partial z} = 0, \tag{3.3}$$

$$\frac{\partial \rho}{\partial t} - \frac{\rho_o N^2 w}{g} = 0, \tag{3.4}$$

$$\frac{\partial p}{\partial z} + \rho g = 0, \tag{3.5}$$

where X and Y are the forcing functions ($\tau^x/h\rho_o$, $\tau^y/h\rho_o$) distributed over the mixed layer as a body force. The remainder of the variables are defined as in other treatments. The usual kinematic boundary conditions are prescribed with zero vertical motion at the sea surface ($z = 0$) and bottom of the profile ($z = -D$).

47

B. FREE MODES

Consider the free mode case in which the forcing functions are zero. Equations (3.1-3.5) can then be simplified to

$$\frac{d^2\varphi_n}{dz^2} + \frac{N^2(z)\,\varphi_n}{c_n^2} = 0,\qquad\qquad(3.6)$$

where φ_n is the nth eigenfunction, $c_n = (\sigma^2 - f^2)/K_n^2$ is the eigenvalue and represents the phase speed of the nth baroclinic mode ($K_n^2 = k^2 + l^2$) and $\varphi_n = 0$ at $z = 0,-D$. The wavelengths derived from the horizontal wavenumber in the free mode case refer to those moving with the disturbance and would be most appropriate in the far-field. Since the AXCP's only sense relative or baroclinic motions, the barotropic mode can not be resolved from the data. The vertical structure equation is numerically solved using the observed spatially-averaged N^2 profile (Fig. 2.11) and a Runge-Kutta 4th order scheme (Gerald, 1983). The first five baroclinic modes for the horizontal velocity eigenfunctions are shown in Fig. 3.1 and the relevant parameters for the first five baroclinic modes are given in Table 6.

1. WKBJ[2] Normalization

As near-inertial waves propagate into the interior of the stratified fluid, they can experience variations in amplitude and vertical wavelength because of the stratification changes (Leaman and Sanford, 1975). The high-order baroclinic modes (small vertical wavelength) are more susceptible to these stratification changes. To accommodate these changes in the stratification, the current profiles are scaled by

$$u_w(z) = u(z)/\sqrt{(N(z)/N_o)}, \text{ and}\qquad\qquad(3.7)$$

$$dz_w = (N(z)/N_o)dz ,$$

where u_w is the WKBJ-scaled current at depth z_w and N_o is the vertically-averaged $N(z)$ which ranges between 2-3 cph, so that the final scaled depth equals the original depth. The expressions in (3.7) represent WKBJ short-wavelength approximation to the wave equation (Robinson and Silvia, 1981).

2. Baroclinic Time Scales

If the scale of the wind stress curl (68 km) in Norbert, is greater than the deformation radius associated with the first mode (43 km) (large-scale limit), there will be a characteristic time scale for each baroclinic mode to separate from the solution in the mixed layer (Gill, 1984). The time required for a phase difference of $\pi/2$ to develop

---

[2]The letters WKBJ stand for G. Wentzel, H. A. Kramers, L. Brillouin and H. Jefferys who independently discovered the procedure working on different problems (Morse and Fesbach, 1953).
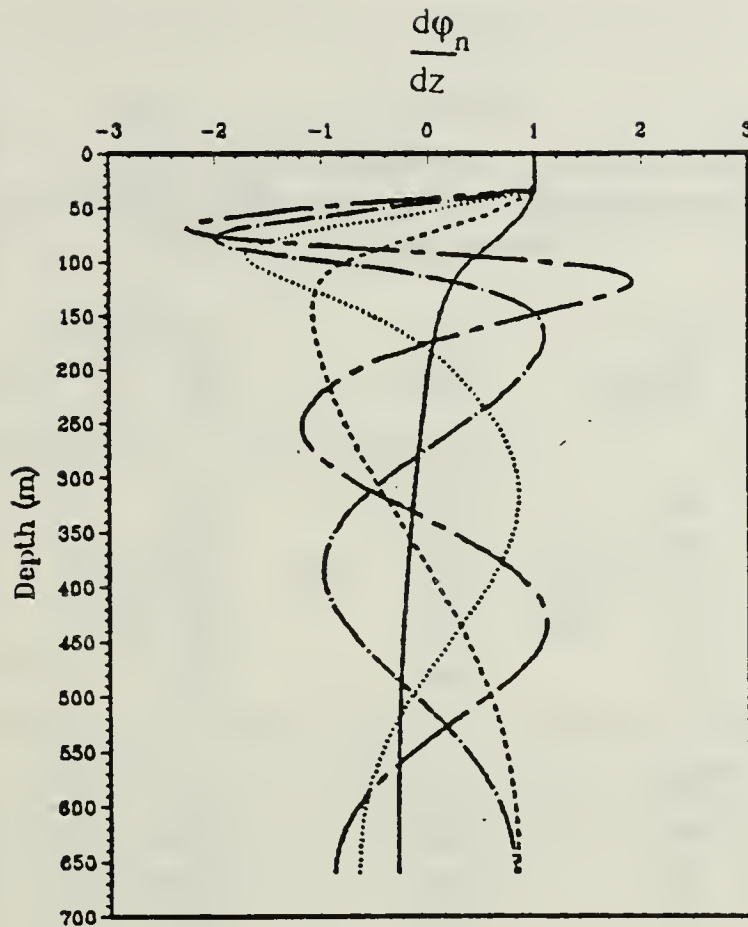
Figure 3.1 Amplitudes of the horizontal velocity eigenfunctions for the first five baroclinic modes: 1 (solid), 2 (dashed), 3 (dotted), 4 (chain-dotted) and 5 (chain-dashed), based on the Brunt-Väisälä frequency profile in Fig. 2.11 and $\sigma = 1.18f.$.

for each baroclinic mode n is given by

$$t_n = \frac{\pi f}{k_s^2 c_n^2} ,$$
(3.8)

where k_s is the inverse storm scale $(2R_{max})^{-1}$ and the other terms have been defined above. These time scales are given in Table 6 for the first five baroclinic modes. The essence of Gill's theory is that the modes will separate from the remainder of the mixed layer (40 m, $N = 0$) solution over these time scales as energy propagates vertically into the thermocline. This modal separation was noted in numerical simulations of the passage of an atmospheric front by Kundu and Thomson (1985) and for the first time in observations acquired during the passage of hurricane Frederic (Shay and Elsberry, 1987a). Since the low-order modes can penetrate into the thermocline very quickly, these time scales will also be compared to amplitude changes in the thermocline (upper 250 m).

TABLE 6

Phase speed (c_n), deformation radius (α_n^{-1}), wavelength (λ_n), the equivalent forcing depth ($\int_{-D}^{0} \varphi_{nz}^{2}(z)dz$) and baroclinic time scales (t_n).

mode n	c_n (m/s)	α_n^{-1} (km)$^{-1}$	λ_n (km)	$\int \varphi_{nz}^{2}(z)dz$ (m)	t_n (IP)
Norbert					
1	2.1	43	231	98	1.2
2	1.4	29	130	334	2.6
3	0.9	19	78	336	4.8
4	0.7	15	56	421	10.5
5	0.5	11	49	592	20.6
Frederic					
1	3.0	42	255	86	1.1
2	1.1	15	92	174	7.5
3	0.7	10	58	373	18.8
4	0.5	7	41	651	36.8
5	0.4	6	33	1056	57.5

$\varphi_{nz} = d\varphi_n/dz$

C. FORCED MODES

The variables in equations (3.1-3.5) are expanded in terms of normal modes

$$w,\rho(x,y,z,t) = \sum_n w_n,\rho_n \varphi_n(z) ,$$

$$u,v,p(x,y,z,t) = \sum_n u_n,v_n,p_n \frac{d\varphi_n}{dz} .$$

The variables (u,v,p,w,ρ) with n subscripts represent horizontal structure functions in (x,y,t), whereas the vertical structure functions are the φ_n's. Although the φ_n's are orthogonal, there is no guarantee that the $d\varphi_n$'s/dz are orthogonal. The inner products of the $d\varphi_n/dz$ and the $d\varphi_m/dz$ are $O(0.01)$ whereas the inner products of $(d\varphi_n/dz)^2$ are $O(100)$ as shown in Table 6. Thus, these terms are neglected in the subsequent analysis. Equations (3.1-3.5) expanded into the normal modes become

$$\frac{\partial u_n}{\partial t} - fv_n = -\frac{1}{\rho_o} \frac{\partial p_n}{\partial x} + X_n, \qquad (3.10)$$

$$\frac{\partial v_n}{\partial t} + fu_n = -\frac{1}{\rho_o} \frac{\partial p_n}{\partial y} + Y_n, \qquad (3.11)$$

$$\frac{\partial u_n}{\partial x} + \frac{\partial v_n}{\partial y} + w_n = 0, \tag{3.12}$$

$$\frac{\partial p_n}{\partial t} - \frac{\rho_o N^2 w_n}{g} = 0, \tag{3.13}$$

$$p_n = \frac{c_n^2}{N^2} g \rho_n \tag{3.14}$$

where the forcing functions are also expanded as

$$X_n = \frac{\tau^x}{\rho_o \int_{-D}^{0} \varphi_{nz}^2 \, dz} \quad \text{and} \quad Y_n = \frac{\tau^y}{\rho_o \int_{-D}^{0} \varphi_{nz}^2 \, dz}.$$

where $\varphi_{nz} = d\varphi_n/dz$.

In this treatment of the wind stress superposition onto the modes, the vertical integrals of the eigenfunction squared ($\int_{-D}^{0} \varphi_{nz}^2 dz$) will be referred to as the equivalent forcing depths (Wunsch and Gill, 1976). These values are also given in Table 6. Notice the last two equations may be recast into

$$w_n = \frac{\partial p_n}{\partial t} \left(\frac{1}{c_n^2 \rho_o} \right) \quad,$$

which renders the conservation of mass equation as

$$\rho_o c_n^2 \left\{ \frac{\partial u_n}{\partial x} + \frac{\partial v_n}{\partial y} \right\} + \frac{\partial p_n}{\partial t} = 0. \tag{3.15}$$

Thus, the governing equation for the vertical velocity for the nth baroclinic mode becomes

$$c_n^2 \left\{ \frac{\partial^2}{\partial x^2} + \frac{\partial^2}{\partial y^2} - \frac{1}{c_n^2} \frac{\partial^2}{\partial t^2} - \alpha_n^2 \right\} w_n = f \nabla x \tau_n + \frac{\partial}{\partial t} \nabla \bullet \tau_n \quad, \tag{3.16}$$

where $\nabla x \tau_n = \partial Y_n/\partial x - \partial X_n/\partial y$ and $\nabla \bullet \tau_n = \partial X_n/\partial x + \partial Y_n/\partial y$. The details of the derivations for the vertical and horizontal velocities are given in the Appendix A. Equation (3.16) is analogous to equation (10) in Geisler (1970) except that the phase speed (c_n) and the inverse deformation radius (α_n) are for the nth baroclinic mode. If the storm is moving steadily with speed U_h in the $+y$ direction, the local time derivative is transformed into a space derivative

$$\frac{\partial}{\partial t} = -U_h \frac{\partial}{\partial y}.$$

Substituting this expression into (3.16) yields

$$\mathcal{L}_2 w_n = -\frac{f}{c_n^2} \nabla x \tau_n + \frac{U_h}{c_n^2} \frac{\partial}{\partial y} (\nabla \bullet \tau_n) ,$$

where the operator is given by

$$\mathcal{L}_2 = \left(\frac{U_h^2}{c_n^2} - 1 \right) \frac{\partial^2}{\partial y^2} - \frac{\partial^2}{\partial x^2} + \alpha_n^2 .$$

This operator is hyperbolic (elliptical) depending on the Froude number $U_h/c_n > (<)$ 1. Only the hyperbolic case ($U_h > c_n$) is considered here. Since the AXCP's measure the vertical shear of the horizontal velocity, the spatial distribution of the corresponding eigenfunctions ($u_n(x,y)$, $v_n(x,y)$) is sought using (3.10), (3.11) and (3.15), which yields (Longuet-Higgins, 1965)

$$\mathcal{L}_2 u_n = -\frac{1}{U_h} \nabla x \tau_n + \frac{1}{c_n^2} \left(fY_n - U_h \frac{\partial X_n}{\partial y} \right),$$

$$\mathcal{L}_2 v_n = \frac{1}{U_h} \int_{-\infty}^{0} \frac{\partial}{\partial x} \nabla x \tau_n dy - \frac{1}{c_n^2} \left(fX_n + U_h \frac{\partial Y_n}{\partial y} \right),$$

where the integrand in the v_n equation is defined only in the direct forcing region. The details of this derivation are given in Appendix A. Geisler (1970) introduced a nondimensional coordinate system

$$y' = \left[\frac{U_h^2}{c_n^2} - 1 \right]^{-1/2} \alpha_n y ,$$

$$x' = \alpha_n x ,$$

which transforms the operator into

$$\mathcal{L}_2' = \alpha_n^2 \left\{ \frac{\partial^2}{\partial y'^2} - \frac{\partial^2}{\partial x'^2} + 1 \right\} .$$

The governing expressions for the vertical and horizontal velocities are

$$\mathcal{L}_2' w_n = -\frac{1}{f} \nabla x \tau_n + \frac{U_h}{f^2} \frac{\partial}{\partial y} (\nabla \bullet \tau_n),$$

$$\mathcal{L}_2' u_n = -\frac{1}{U_h \alpha_n^2} \nabla x \tau_n + \frac{1}{f^2} \left(fY_n - U_h \frac{\partial X_n}{\partial y} \right), \qquad (3.17)$$

$$\mathcal{L}_2' v_n = \frac{1}{U_h \alpha_n^2} \int_{-\infty}^{0} \frac{\partial}{\partial x} \nabla x \tau_n dy - \frac{1}{f^2} \left(fX_n + U_h \frac{\partial Y_n}{\partial y} \right).$$

The $\nabla x \tau_n$ and $\nabla \bullet \tau_n$ are the wind stress curl and divergence of the wind stress as a function of mode number. The dominant wind stress curl term sets up the semi-permanent baroclinic ridge in the wake of the storm. The second term in the vertical

velocity equation is the gradient of the wind stress divergence. Since the divergence term is negative (convergence), the gradient of the divergence has the same sign as the wind stress curl, which augments the effect of the wind stress curl on the ocean current response. In the horizontal velocity equations, the second terms on the right side represent those components that are directly driven by the wind stress (Y_n/f and $-X_n/f$), which are referred to here as Ekman-type velocities. The third terms in the u and v equations represent a sink of vorticity and the y-component of the divergence, respectively. Most analytical treatments have ignored the divergent and Ekman-type terms because the wind stress curl sets up the semi-permanent baroclinic ridge, and it has been assumed that the inflow angle was zero. However, Mayer *et al.* (1981) showed that the scales of the wind stress divergence were 30 - 50 % of the curl term in hurricane Belle.

D.   IMPULSIVE FORCING

Since the translation speed of Norbert exceeds the first mode internal wave phase speed, the oceanic response should be dominated by baroclinic near-inertial waves in the wake of the hurricane. A further consequence of this relationship is that the ocean is undisturbed well ahead of the storm, which may be demonstrated by a direct application of the radiation boundary condition (Lighthill, 1967).

The solutions of (3.17) begin with the assumption that the right side can be approximated with a dirac delta function to represent an impulsive type of forcing function

$$\nabla \times \tau_n = -\tau_{on} \, L \, \delta(x)\delta(y) \, ,$$

where τ_{on} represents the magnitude of the wind stress projected onto the nth baroclinic mode and L is the the scale of the storm (typically $2R_{max}$). Without loss of generality, only the curl term will be operated upon here, and the divergence and Ekman-type terms will be dropped from the transform and inversion process (but not from the solution). The implusive forcing assumption can be similarly applied to the other terms.

The first equation in (3.17) is recast into an expression with an impulsive forcing on the right-hand side with the nondimensional operator on the left side

$$\mathscr{L}_2 w_n = \frac{\tau_{on}\alpha_n^2}{fL} \left[\frac{U_h^2}{c_n^2} - 1 \right]^{-1/2} \delta(x')\delta(y') \, . \tag{3.18}$$

Double Fourier transforming (3.17) yields

$$\widehat{\tau}(k,l) = \frac{\tau_{on}\alpha_n^2}{fL} \left[\frac{U_h^2}{c_n^2} - 1 \right]^{-1/2} \left[\frac{1}{(k^2 - l^2 + 1)} \right] \, ,$$

53

and substituting into the inversion formula renders an integral equation representing a fundamental solution to the problem or a Green's function (Stakold, 1978)

$$F(x',y') = \frac{\tau_{on}\alpha_n^2}{fL}\left[\frac{U_h^2}{c_n^2}-1\right]^{1/2}\iint_{-\infty}^{\infty}\frac{1}{(k^2-l^2+1)}e^{-ikx'}e^{-ily'}dk\,dl\ .$$

The Green's function that emerges from the solution of the integral equation is a Bessel's function of order 0 (see Appendix B):

$$\iint_{-\infty}^{\infty}\frac{1}{(k^2-l^2+1)}e^{-ikx'}e^{-ily'}dk\,dl = \frac{J_0((y'^2-x'^2)^{1/2})}{2}H(y'-x')\ .$$

Because a hurricane can be represented by a circularly symmetric point source translating over the ocean, the Bessel function is geometrically appropriate and $H(y'-x')$ represents a unit step function. Since the argument of the Bessel function involves (y',x') or $(\alpha_n y, \alpha_n x)$, the fundamental solution also represents a two-dimensional eigenvalue problem.

E.   THE SOLUTION

Generally, the solution to an integral equation is represented by a convolution of the forcing term and the Green's function integrated over all source points $(\overline{x},\overline{y})$ within the direct forcing region

$$w_n = \frac{-1}{\tau_{on}L}\iint_{-\infty}^{\infty}\nabla x\tau_n(\overline{x},\overline{y})G(y',\overline{y};x',\overline{x})\,d\overline{x}\,d\overline{y}\ ,$$

where the coefficient $(\tau_{on}L)^{-1}$ is due to the impulsive forcing assumption.

As noted above, the complete set of forcing functions will now be introduced into the convolution integral for the 3-dimensional velocity structure

$$w_n = -\frac{1}{2f}\int_{-\infty}^{\infty}\int_0^{\infty}\nabla x\tau_n J_0(r')d\overline{x}\,d\overline{y} - \frac{U_h}{2f}\int_{-\infty}^{\infty}\int_0^{\infty}\frac{\partial}{\partial y}(\nabla\bullet\tau_n)J_0(r')d\overline{x}\,d\overline{y},$$

$$u_n = -\frac{1}{2U_h\alpha_n^2}\int_{-\infty}^{\infty}\int_0^{\infty}\nabla x\tau_n J_0(r')d\overline{x}\,d\overline{y} + \frac{1}{2f^2}\int_{-\infty}^{\infty}\int_0^{\infty}(fY_n-U_h\frac{\partial X_n}{\partial y})J_0(r')\,d\overline{x}\,d\overline{y},\qquad(3.19)$$

$$v_n = \frac{1}{2U_h\alpha_n^2}\int_{-\infty}^{\infty}\int_0^{\infty}\int_{-\infty}^{\infty}\frac{\partial}{\partial x}\nabla x\tau_n dy\,J_0(r')\,d\overline{x}\,d\overline{y} - \frac{1}{2f^2}\int_{-\infty}^{\infty}\int_0^{\infty}(fX_n+U_h\frac{\partial Y_n}{\partial y})J_0(r')d\overline{x}\,d\overline{y},$$

where the Bessel function represents the kernel in the convolution and the argument is given by:

$$r'^2 = \frac{1}{\alpha_n^2}\left[\left[\frac{U_h^2}{c_n^2}-1\right](y'-\overline{y})^2 - (x'-\overline{x})^2\right]\ .$$

54

The limits of the integration are from zero to $-\infty$ in y' as a result of the radiation boundary condition. In these convolutions, the direct forcing region will be restricted to R_{max} for the curl and divergence terms, and to 40 km for the Ekman-type terms. If the size of these regions is doubled, the simulated velocities are similarly increased.

F. COMPARISON TO THE TWO-LAYER MODEL

The effect of a continuously stratified ocean model versus a two-layer model as in Geisler (1970) is demonstrated with a wind stress curl similar to that of Geisler

$$\nabla \times \tau_n = 2.5 \ \frac{\tau_m}{L} \left\{ \frac{r}{L} - \frac{r^2}{L^2} \right\} e^{-r/L} \ , \tag{3.20}$$

where τ_m is the maximum wind stress (3 N/m^2), r is radial distance from the storm center and L is the length scale of the wind stress curl (100 km). In these numerical experiments, the storm translation speed is 7 m/s and a phase speed of the internal mode is 1.4 m/s.

In this version of the model (Fig. 3.2a), maximum upward velocities are slightly greater than the 3 nondimensional units predicted by Geisler (1970). In dimensional units, these values are about 7-8 x 10^{-2} cm/s, which is twice the velocity Price (1983) and Greatbatch (1984) predicted from scaling arguments. The pattern of vertical velocities is elongated in the cross-track direction over the first half of the inertial cycle (220 km) with a scale of 8R$_{max}$. The lateral spreading of the wave-wake is due to the localized core of positive vorticity, which is usually confined to r $<$ 2R$_{max}$.

To compare the effect of various wind stress curl patterns, a second numerical experiment is performed by replacing the stress pattern in (3.20) with a Rankine vortex (2.2) that is based on the same parameters above. The region of positive vertical velocities (Fig. 3.2b) is confined to a narrower region of r $<$ 2R$_{max}$ with comparable maxima of 7-8 x 10^{-2}. The pattern is more crescent-shaped and more resembles the character of the Bessel function than in the simulation with (3.20). The vertical velocities damp more quickly because the spatial scale of the wind stress forcing is smaller by 2R$_{max}$.

1. Vertical Velocity

Using the Rankine vortex and storm parameters from Norbert, the total vertical velocity for a sum of the first three baroclinic modes is shown in Fig. 3.3. The vertical velocity is upward (positive) in the direct forcing regime with maximum values of 0.1-0.2 cm/s which agrees well with scaled vertical velocity (0.1 cm/s) based on the
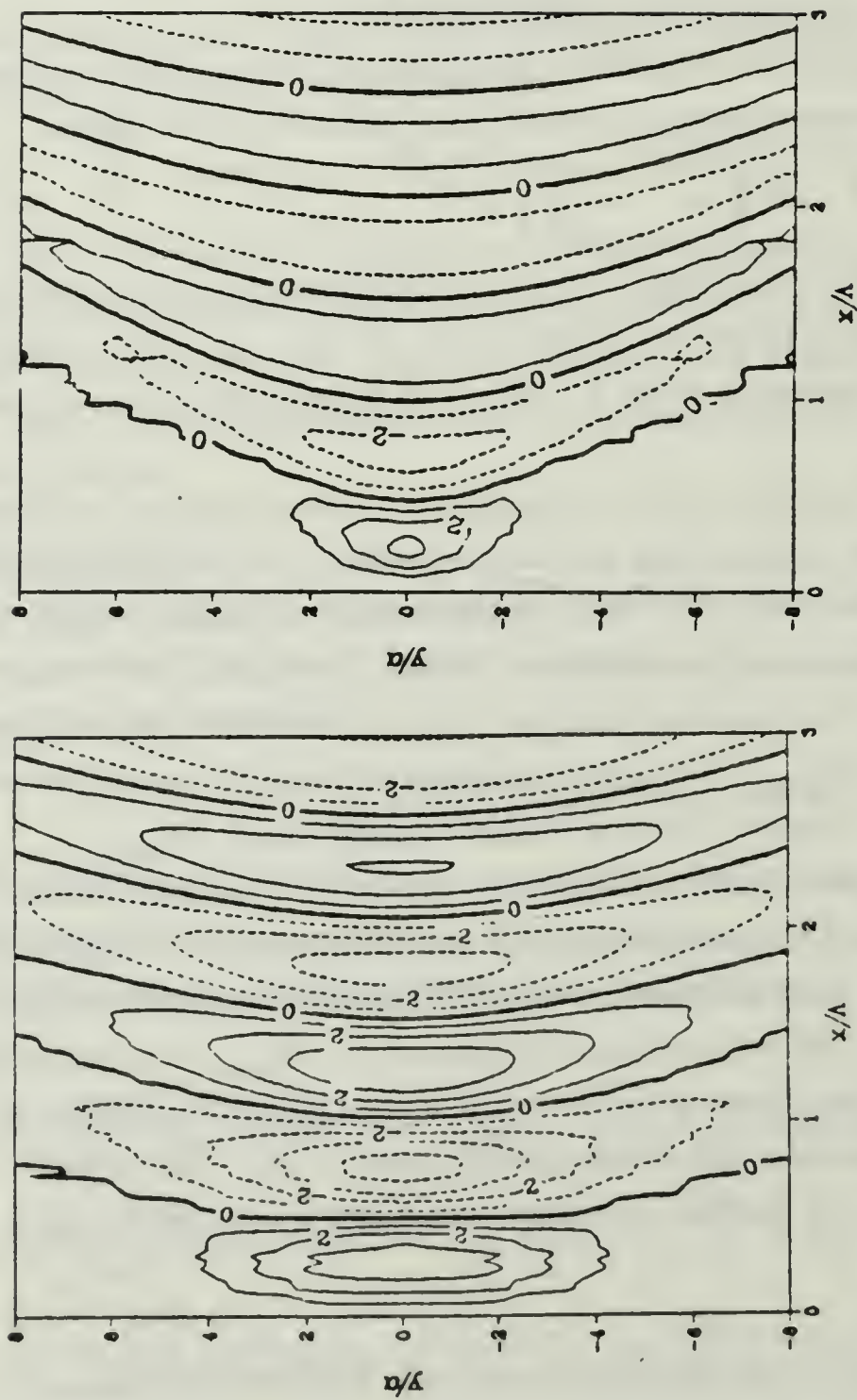
Figure 3.2 Nondimensional vertical velocity contours from the two-layer model using the wind stress curl (left) from Geisler (1970) and (right) a Rankine vortex. The storm is moving in the -x direction at 7 m/s. The contour interval is 2.5 x 10^{-2} cm/s and the storm and ocean parameters are R_{max} = 30 km, τ_m = 3 N/m^2 and c_1 = 1.4 m/s. The abscissa and ordinate are normalized by the wavelength of the first mode (850 km) and R_{max}.

56

maximum stress. The upward (downward) vertical velocities indicate areas of upwelling (downwelling) on the semi-permanent baroclinic ridge that is established due to the net input of cyclonic vorticity by the storm (Price, 1981). Upper ocean currents diverge from the storm track as cooler water is upwelled. Conversely, the horizontal currents in areas of downwelling, converge toward the storm track. The horizontal wavelength for the first mode estimated from linear theory is 440 km. This is the wavelength in the fixed frame as opposed to the wavelength moving with the storm, which scales with wavelength of the first free mode $(c_1 = \sigma/K_1)$.

As expected, the pattern is dominated by the wind stress curl (Fig. 3.3a). For an inflow angle 20°, the contribution of the divergence term in the direct forcing region is approximately 25 % of the curl term. For larger inflow angles, the wind stress divergence becomes larger. However, there does not seem to be any semi-permanent ocean features set up by the wind stress divergence as in the case of the curl. The effect of the divergence damps away from the directly forced region within 2-3 inertial wavelengths. The contribution here is associated with the gradient of the divergence, which has a scale half that of the curl term and accounts for the decrease in magnitude.

Since the kernel of the integral in (3.19) is the Bessel function, the decay of the velocity amplitudes follows from an asymptotic analysis of that function (Arfken, 1970)

$$J_o(y) = \sqrt{\frac{2}{\pi y}} \cos (y - \pi/4) \ , \tag{3.21}$$

which implies that the amplitude approximately decreases as $y^{-1/2}$.

The structure of the horizontal velocities (Fig. 3.4) for a summation of the first three modes corresponds to the pattern of the vertical velocity. Maximum v-components exceed 100 cm/s in the first upwelling area in the wake. Within the next half-wavelength, the v-component changes direction and is associated with the convergence of flow and the downwelling of the near-surface waters. The u-component velocity pattern is out of phase with the v-component and the maximum u-component is 60 cm/s. Thus, the velocities are varying as expected for forced, near-inertial motions superposed on the mean flow associated with the baroclinic ridge. The pattern broadens in the wake of the storm according to $\tan^{-1} (U_h^2/c_n^2-1)^{-1/2}$ and the amplitudes decrease according to the asymptotic expression (Geisler, 1970).

The major term in the momentum balance of the horizontal velocites is the wind stress curl (Fig. 3.4b). As expected, the first baroclinic mode terms dominate the
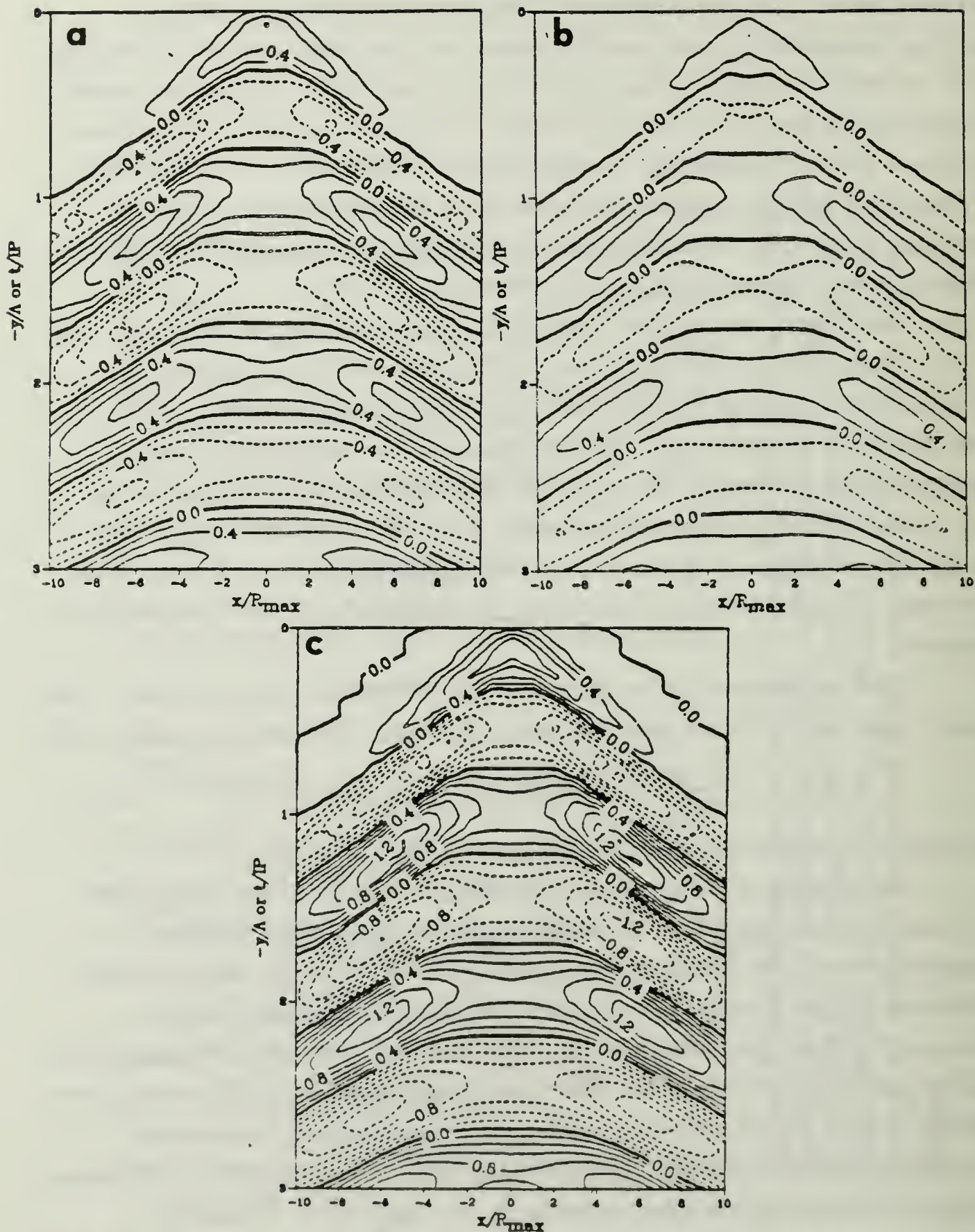
Figure 3.3 Nondimensional vertical velocity contours at 90 m for a summation of the first three baroclinic modes in the thermocline based on the Rankine vortex model for (a) only the wind stress curl, (b) only the wind stress divergence and (c) the total (a + b). The model storm is moving in the + y direction at 4 m/s. The contour interval is as Fig. 3.2 and the ordinate and abscissa axes are nondimensionally scaled with the wavelength of the first mode (440 km) and R_{max} (30 km).

other baroclinic modes by factor of about three to four because of the superposition of the wind stress onto the modes. The divergence and Ekman terms are considerably weaker with relative maxima of 20 and 10 cm/s, respectively (Fig. 3.4c and d). The divergence term augments the wind stress curl term in the direct forcing area, but damps very quickly after 2 Λ. By contrast, the Ekman terms act to diminish the velocities induced by the curl and divergence terms by roughly 10 cm/s. The importance of the Ekman term also diminishes rather quickly, which is not surprising since the wind stress is also diminishing quickly beyond a radius of 200 km. It is clear that the wind stress curl dominates the ocean response over short and long space (time) scales. However, the divergence and Ekman terms do contribute to oceanic current variations within the direct forcing region.

2. **Simulated Vertical Structure**

Using the expansions in (3.9), the simulated velocity fields from the linear model $(u_n(x',y'),v_n(x',y'))$ are constructed in the form of a depth-space or depth-time series by multiplying the horizontal structure functions by the vertical structure functions $\varphi(z)$. Since the model is linear and the large scale limit is satisfied (S = 1.5), these separation time scales of the modes predicted by Gill (1984) should become clear in the wake. As shown above (Table 6), these baroclinic time scales are : $t_1 = 1.2$ IP; $t_2 = 2.6$ IP; and $t_3 = 4.8$ IP in hurricane Norbert. The essence of Gill's theory is that the modes will separate from the remainder of the mixed layer solution over these time scales as energy propagates vertically into the thermocline. This modal separation was noted in numerical simulations of the passage of an atmospheric front by Kundu and Thomson (1985) and for the first time in observations acquired during the passage of hurricane Frederic (Shay and Elsberry, 1987a).

An along-track (or time series) section of the v-component for a summation of the first three baroclinic modes is shown in Fig. 3.5 at $x = \pm R_{max}$. The abscissa depicts either space or time normalized to a wavelength Λ of 440 km or an IP of 1.5 days. Within the first 1.5 IP, the maximum velocity component decreases from about 110 cm/s to about 70 cm/s as the first baroclinic mode propagates out of the mixed layer and into the thermocline. The slope of the zero lines is upward towards the left which represents an upward phase propagation. This corresponds to downward energy propagation for near-inertial waves (Leaman and Sanford, 1975). A second decrease in mixed layer velocity after about 3 IP corresponds to the time scale associated with the second baroclinic mode. Energy in the upper ocean remains essentially constant

59
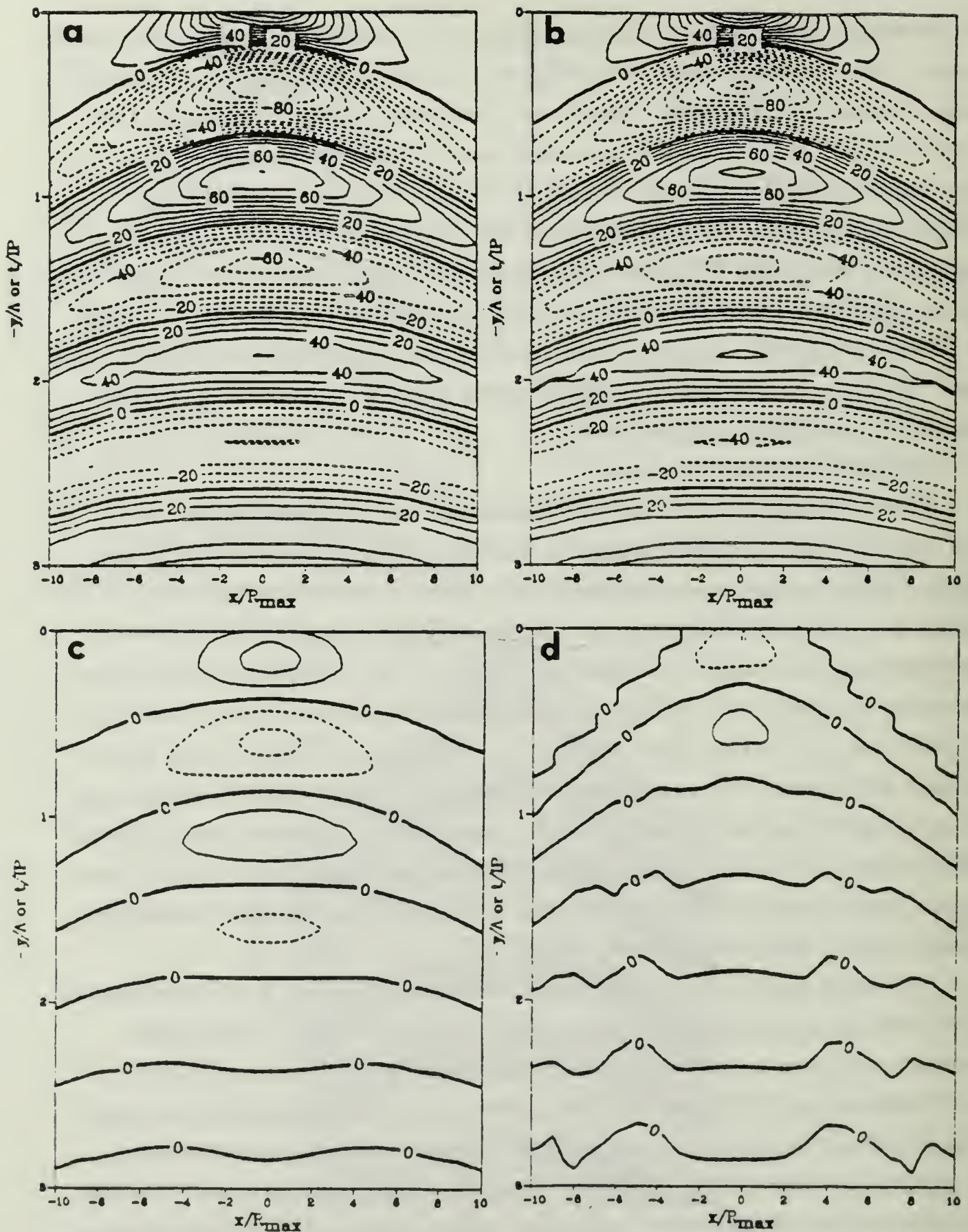
Figure 3.4 Simulations of the mixed layer v-component (cm/s) for a summation of the first three baroclinic modes for forcing due to (a) all the forcing terms, b) the wind stress curl, (c) the wind stress divergence and (d) the wind stress based on the observed storm parameters in Norbert. The contour interval is 10 cm/s with a maximum of 110 cm/s.

between 3-5 IP. The time required for the first baroclinic mode to again become in phase in the mixed layer is roughly $4t_1$ or 4.8 IP, which also corresponds to the time scale of the third baroclinic mode separating from the mixed layer ($t_3 = 4t_1$). At about 5 IP, the mixed layer velocity actually increases by 10 cm/s, which appears to be associated with the more dominant first baroclinic mode rather than a decrease in the mixed layer velocity as the third mode separates from the solution. This full-cycle of mode 1 ($4t_1$) also agrees with simulations by Kundu and Thomson (1985).

G. SUMMARY

In this chapter, the linear, two-layer model of Geisler (1970) has been extended to include a continuously stratified fluid. The wind stress is superposed unto the first five baroclinic modes as in Kundu and Thomson (1985). The veracity of the analytical model was demonstrated by collapsing the continuously stratified model into a two-layer model to directly compare with the results of Geisler. The slight differences in the response of the vertical velocity is due to the selection of the forcing functions. It appears that the Rankine vortex forcing gives more realistic results than the forcing (3.20) used by Geisler.

To facilitate comparisons to the AXCP observations, explicit relationships for the horizontal velocities have been derived for a northward moving storm. The behavior of the modal amplitudes for the v-component agrees well with the time scales predicted from Gill's theory. Thus, the analytical model velocities for the first few modes will be compared to the AXCP data acquired during Norbert within the near-field.

61
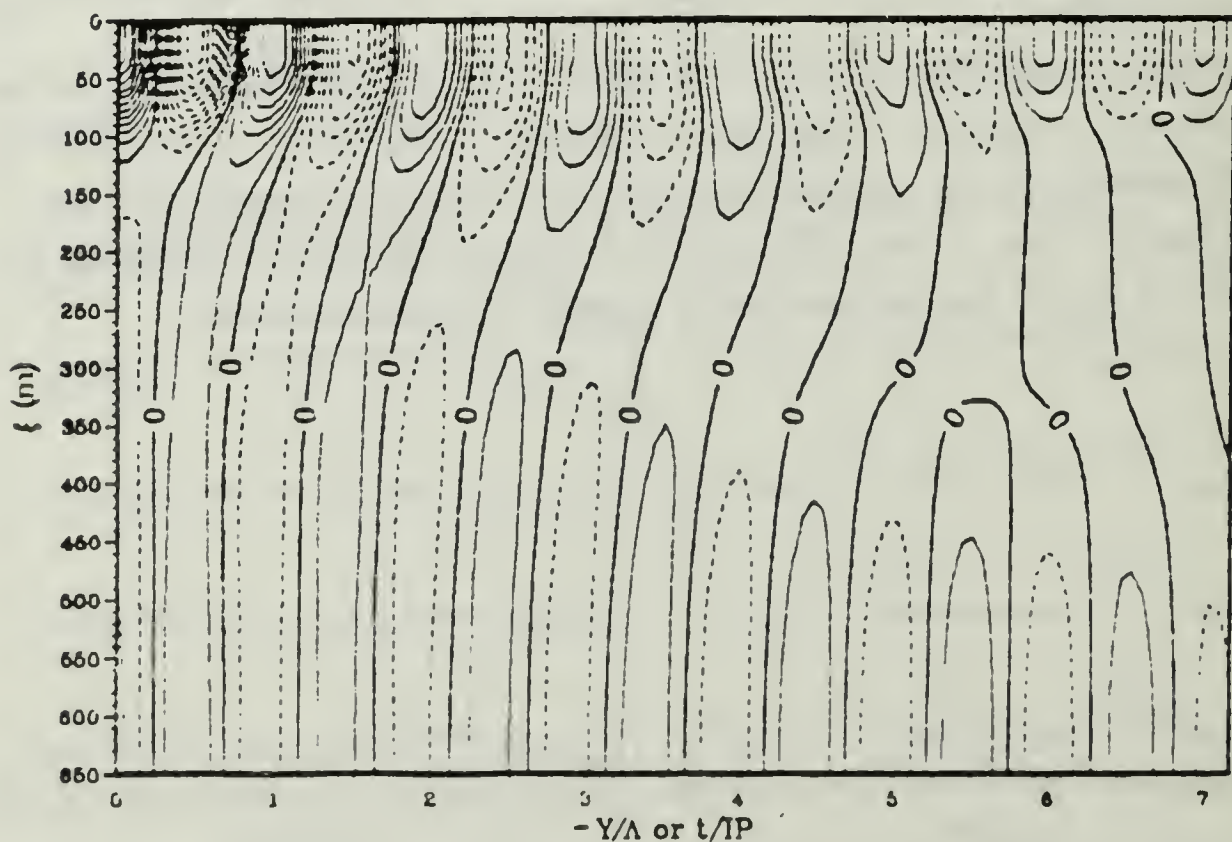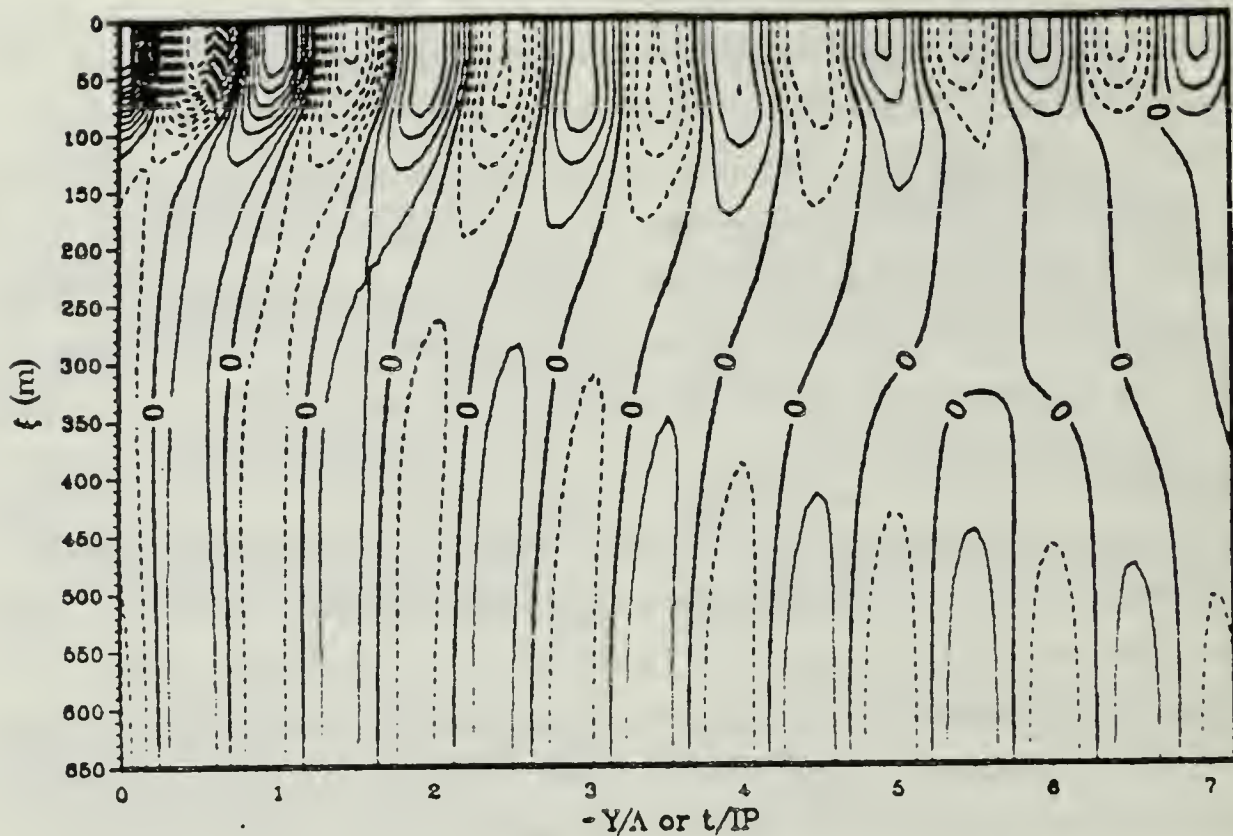
Figure 3.5 Summation of the first three baroclinic modes for the v-component from the forced model in the along-track direction at $x = R_{max}$ (upper) and $x = -R_{max}$ (lower) with a contour interval of 10 cm/s. The solid (dashed) contours represent positive (negative) velocity. The abscissa is normalized by the wavelength of the first mode (440 m).

IV. TIME EVOLUTION

The advantage of the moored current meter data is the ability to depict the
detailed time evolution of the currents and temperatures at selected levels prior, during
and subsequent to storm passage. In this chapter, the near-inertial response is isolated
from the moored ocean current and temperature measurements in hurricane Frederic
by complex demodulation. The amplitudes of the near-inertial currents are fit to the
the vertical modes and the time-evolution of the modes is compared to the predictions
from linear theory of Gill (1984). Because these data were acquired along the
periphery of the DeSoto Canyon, the effects of the sloping bottom on the first two
baroclinic modes are studied using the model of Lai and Sanford (1986).

The ocean current and temperature data were low-pass filtered at 3 h using a
Lanczos taper window (Table 7) and were subsampled every hour to smooth the data
series. The smoothed data series were used for most of the data analyses except in the
spectral calculations where increased time resolution was required.

TABLE 7
Characteristics of the low-pass Lanczos filter.

Period (h)	Energy Rejection
3	6 db at 2.9 h
	20 db at 2.6 h
48	6 db at 40 h
	20 db at 24 h

The *I*nertial *P*eriods (IP's) are equal to 24.2 and 24.5 h at CMA 2 and 3 (Fig.
2.1), respectively whereas the local IP at the OTEC site is 25.8 h. The length scale of
the near-inertial response will be referenced to the scale of the wind stress curl, which is
approximately 60 km for Frederic (Powell, 1982), and the Rossby radii of deformation
(see Table 6) for the barotropic and first three baroclinic modes. These deformation
radii are based on the near-inertial wave phase speeds computed from the Sturm-
Liouville problem, which was discussed in Chapter III.

63

If the scale of the wind stress curl (60 km) is greater than the deformation radius associated with the first mode (42 km), there will be a characteristic time scale for each baroclinic mode to separate from the solution in the mixed layer (Gill, 1984). For the Frederic case, the baroclinic time scales are t_1 = 25 h, t_2 = 7.5 IP and t_3 = 18.8 IP for first three baroclinic modes. The above relationship was derived for changes in the baroclinic modes within the mixed layer. Since the low-order modes can penetrate into the thermocline very quickly, these time scales will also be compared to clockwise amplitude changes in the thermocline (upper 250 m).

A.   OCEAN CURRENT SPECTRA

A Tukey data window (Otnes and Enochson, 1978) is applied to the original current observations prior to the removal of the mean in the calculation of the energy spectra. The data are Fourier transformed and spectrally-averaged over bandwidths to help decrease leakage of energy to adjacent frequency bands (Otnes and Enochson, 1978). Energy above the Nyquist frequency ($1/2\Delta t$), where Δt is the 10 minute sampling interval (20 minutes at OTEC), is eliminated to minimize aliasing of the spectra.

The auto-spectra of the cross- and along-track velocity components in the mixed layer at CMA3 are fairly representative of the spectra throughout the water column (Fig. 4.1). The dominant peak in the spectra is shifted above the local inertial frequency and is significant at the 95 % confidence level. The variance associated with the near-inertial motion is nearly two orders of magnitude larger than the peak at the semi-diurnal frequency. Because of the large bandwidth in the near-inertial band (typically 0.01 cph), the frequency shifts cannot be determined from the spectra. The spectra are red at the higher frequencies, which indicates fairly reliable current measurements.

The energy spectra are decomposed into clockwise (CW) and counter-clockwise (CCW) rotating components to illustrate the rotational characteristics of the inertial wave motion (Gonella, 1972 ; Mooers, 1973). The rotary spectrum estimates for the near-inertial period motions are given in Table 8. Generally, the CW spectral density estimates are 1 to 2 orders of magnitude larger than the CCW rotating motion. However, the CCW spectral density exceeds that in the CW direction in the upper thermocline (100 m) at the OTEC site. Since, the CW and CCW spectral densities at CMA1 are not significantly different, the paper will concentrate on the near-inertial
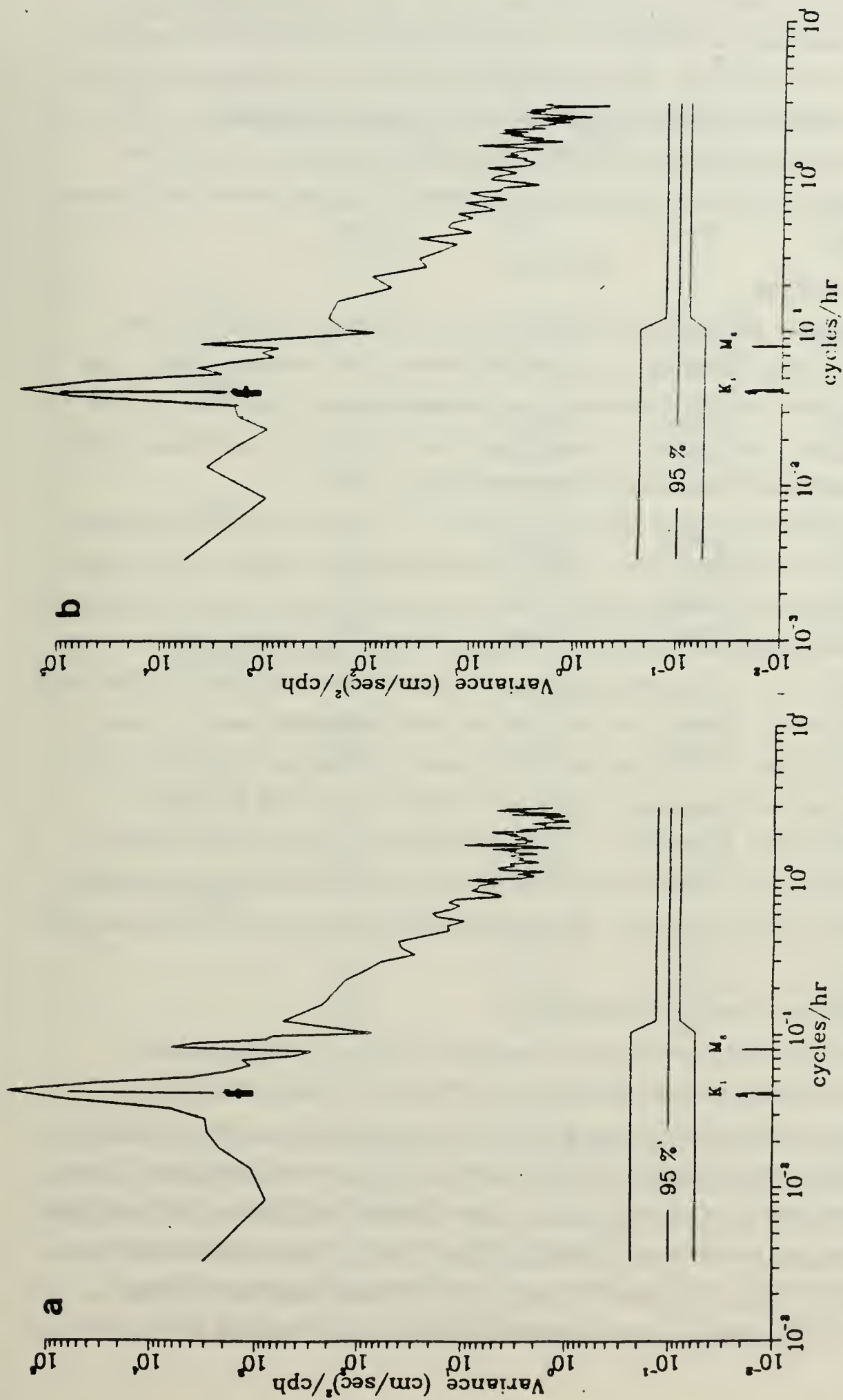
Figure 4.1 Normalized auto-spectra from CMA3 for a) cross-track and b) along-track velocity components in the mixed layer. K_1, f, M_2 represent the diurnal tide, inertial and semi-diurnal tide frequencies. The 95 % confidence intervals are shown at the bottom.

response at CMA2, CMA3 and the OTEC moorings. The rotary coefficients are indicative of the amount of coherence or correlation between the horizontal velocity components (Fofonoff, 1969). For near-inertial oscillations, the coefficients approach unity, which is the case in these records except in the upper thermocline at OTEC. By contrast, the subinertial (periods of 3 IP) and superinertial (periods of 12 h) CW spectral estimates (not shown) are more than an order of magnitude less than the near-inertial motion.

1. Tidal Analysis

A harmonic analysis was performed over a 29-day time series of the pre-hurricane current data following the method of Doodson and Warburg (1941). The variances associated with the semi-diurnal and diurnal frequency bands are given in Table 9 for the pre-storm period. Generally, the tides in this region are diurnal with very weak semi-diurnal components (Zetler and Hanson, 1972).

The diurnal tides are dominated by the K1, O1 and P1 tides in this region of the Gulf of Mexico (Molinari *et al.*, 1979). Considerably more variance is associated with the diurnal tides in the upper layers than in the lower layers. Molinari and Mayer (1982) also found larger tidal currents at 100 m (4-5 cm/s) than at 550 m (2-3 cm/s) at the Tampa OTEC site. The corresponding amplitudes in the mixed layer at CMA2 and CMA3 were 4-5 cm/s. Below the mixed layer, the tidal amplitudes were 2 - 3 cm/s, except at 437 m (CMA3) where the amplitudes nearly equaled that observed in the mixed layer. These estimates agree with other estimates in the Gulf of Mexico (Brooks, 1983 ; Daddio *et al.*, 1977). The periods of near-inertial and diurnal tidal signals are very close and cannot be resolved since the spectral bandwidth around the daily oscillations is about 0.01 cph. Thus, the diurnal tides were not removed from the time series.

2. Current and Temperature Response

Near-inertial wave excitation by hurricane Frederic was clearly evident throughout the water column at the three arrays (Fig. 4.2). The increase in the currents at all levels was first felt about 8-9 h in front of the storm. The mixed layer currents oscillated with magnitudes of 80-90 cm/s, which agrees with the mixed layer currents in the numerical simulations of hurricane Frederic by Hopkins (1982) and with predictions based on the scaling arguments of Greatbatch (1984). These currents then decreased over e-folding scales of about 4 IP. However, the behavior of the near-inertial waves in the thermocline was markedly different from the mixed layer. For

66

TABLE 8

Near-inertial rotary spectrum estimates shifted above the
local inertial frequency.

	Depth (m)	CW $(cm/s)^2/cph$	CCW	Rotary Coeff.
CMA1				
	49	6.7×10^3	1.3×10^3	$+0.68$
	64	2.5×10^3	1.4×10^3	$+0.62$
CMA2				
	19	1.8×10^5	3.5×10^3	$+0.96$
	179	4.6×10^4	3.7×10^2	$+0.95$
	324	2.8×10^4	1.3×10^2	$+0.96$
CMA3				
	21	4.0×10^5	2.0×10^3	$+0.98$
	251	1.4×10^5	6.1×10^2	$+0.98$
	437	1.2×10^5	6.3×10^2	$+0.98$
	457	6.2×10^4	5.0×10^2	$+1.00$
CMA6				
	19	1.4×10^5	5.1×10^3	$+0.95$
	180	7.5×10^3	2.0×10^2	$+0.92$
	330	5.0×10^3	1.0×10^2	$+0.95$
CMA9				
	20	3.8×10^5	1.8×10^3	$+0.95$
	250	1.1×10^5	5.0×10^2	$+0.93$
	500	5.0×10^4	2.0×10^2	$+0.95$
OTEC				
	100	2.7×10^3	3.3×10^3	-0.20
	232	2.1×10^4	1.0×10^2	$+0.95$
	546	1.6×10^4	9.0×10^1	$+0.95$
	950	3.5×10^3	7.0×10^1	$+0.90$

example, the currents in the thermocline at CMA3 (251 m) and CMA2 (179 m) oscillated with amplitudes of 25 cm/s and described a modulation envelope within 7 IP subsequent to the passage of Frederic. The thermocline currents at CMA3 persisted for nearly the entire record following storm passage (21 IP). The near-bottom currents showed similar modulation behavior at both arrays. The OTEC data (Fig. 4.2c) indicate that the near-inertial response is even deeper than suggested by the

TABLE 9

Variance of the semi-diurnal (M2,K2,N2,T2) and diurnal
(K1,O1,P1) tides estimated from 29 days of pre-storm data.

	Depth (m)	Semi-diurnal $(cm/s)^2$	Diurnal $(cm/s)^2$
CMA1			
	21	3	44
	49	2	5
	64	2	6
CMA2			
	19	2	23
	179	2	10
	324	1	1
CMA3			
	21	2	20
	251	1	4
	437	1	16
	457	1	3
OTEC			
	100	2	#
	232	1	#
	546	1	#
	950	2	#

* OTEC analyses are based on only 10 days of pre-storm data.
\# Could not be resolved from 10 days of pre-storm data.

NAVOCEANO data. Although the current speeds at 232 m were considerably weaker ($\pm$ 15 cm/s) than those observed at the CMA3 (which was closer to the hurricane path), the currents at the OTEC site increased in magnitude between 4-6 and 8-10 IP.

The thermocline and near-bottom temperatures at CMA2 and CMA3 were modified considerably by the passage of the storm. These temperatures were in-phase with the along-track velocity component, as expected from plane wave theory (Mayer et al., 1981). At CMA2 (Fig. 4.2b), the pre-storm temperatures at 179 m ranged between 14.3 to 14.8 °C. As the storm arrived, the temperature increased by about 3 ° at this level. This was followed by a near-inertial response over the next 10 IP. Initially, the near-bottom (324 m) temperature decreased by 1.5 ° C and subsequently increased about 3.5 ° C over one IP. Small amplitude, near-inertial oscillations were superposed on a lower frequency (about 4 IP) oscillation following storm passage. At CMA3, the thermocline (250 m) and near-bottom (457 m) temperatures followed similar trends except for a shorter period oscillation (2 IP) in the near-bottom temperatures.
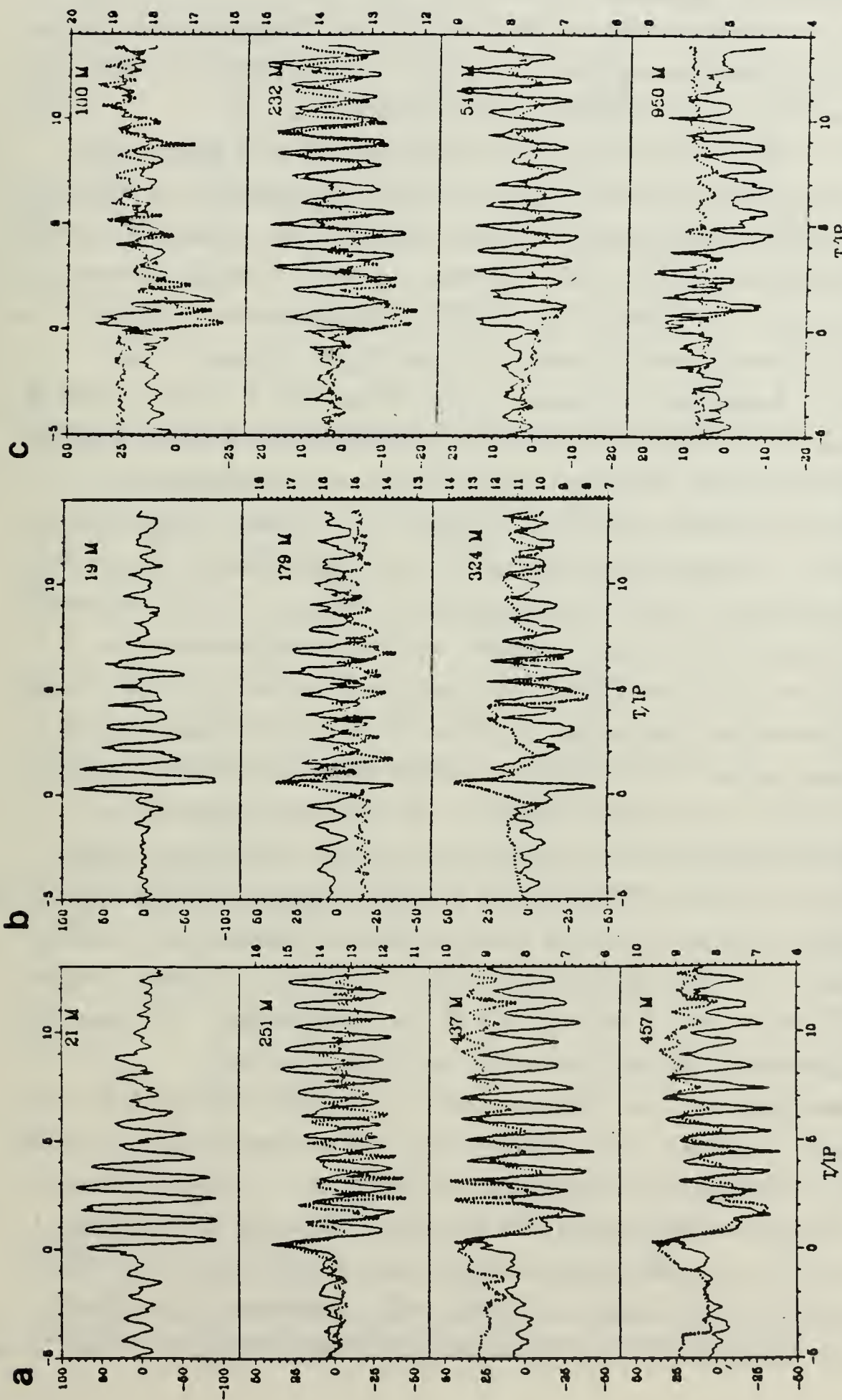
Figure 4.2 Along-track velocity (cm/s, solid) and temperature (°C, dashed) time series at a) CMA3 , b) CMA2 and c) OTEC site from 7 Sept. to 25 Sept. 1979. Time t = 0 corresponds to the time of closest approach of hurricane Frederic at 21 UTC 12 Sept. (CMA2 and CMA3) and 12 UTC 12 Sept. (OTEC).

The near-inertial response in the ocean currents and temperatures at CMA6 and CMA9 are quite similar to those at CMA2 and CMA3. The thermocline currents at CMA9 (250 m) increased in amplitude to about 22 cm/s after about 7 IP which also defined a modulation envelope observed at CMA2 and CMA3.

Mean currents were estimated by a running average over an inertial period. The largest mean currents were oriented along the bottom topography at all three sites. At CMA3 (Fig. 4.3a), the mean along-track (nearly parallel to the topography) current direction was towards the south at 4 cm/s. However, there was a significant change in the mean current about 9-12 h prior to the time of closest approach of hurricane Frederic. First, the mean currents increased at all four depths by about 10 cm/s towards the north. Subsequently, the mean current reversed over 2 IP and exceeded 10 cm/s towards the south. Moreover, the near-bottom mean current exceeded that in the mixed layer and thermocline. The mean cross-track current in the mixed layer at CMA2 was 20-25 cm/s before the arrival of the storm and was much stronger than at CMA3 (Fig. 4.3b). Although the mean current decreased slightly during the period of inertial wave excitation, it returned to pre-storm values within an IP. The mean mixed layer current reversed after 8 IP, but it is unclear whether this was related to the forcing associated with hurricane Frederic. Another significant feature at CMA2 is the increase of the thermocline mean current to 25 cm/s about 5 IP following the storm. Although the mean current at this level did not reverse as in the mixed layer, a rapid decrease to pre-storm values occurred after 8 IP. The observed mean currents at CMA6 and CMA9 follow the bottom topography and support these interpretations.

The mean flow at the OTEC site (Fig. 4.3c) also changed a few hours prior to the time of closest approach of hurricane Frederic (12 UTC 12 September). The mean currents exceeded 5 cm/s flowing towards the north at all depths. The mean current at 100 m oscillated with periods on the order of 5 IP after storm passage. This appears to be a local phenomena as it was not observed at any of the other depths.

The mean currents in the thermocline were also markedly different at all array sites (see Fig. 4.3). Whereas a slow, southward mean flow was observed at CMA3, the mean flow was towards the north at all levels at the OTEC site. This pattern suggests a convergence zone existed between the DeSoto Canyon region and the OTEC site. Climatologically, there is a predominant northward mean flow following the isobaths during the summer months (Molinari and Mayer, 1982). Furthermore, Black (1983) indicates that the Loop Current was located about 100 km south of the OTEC site
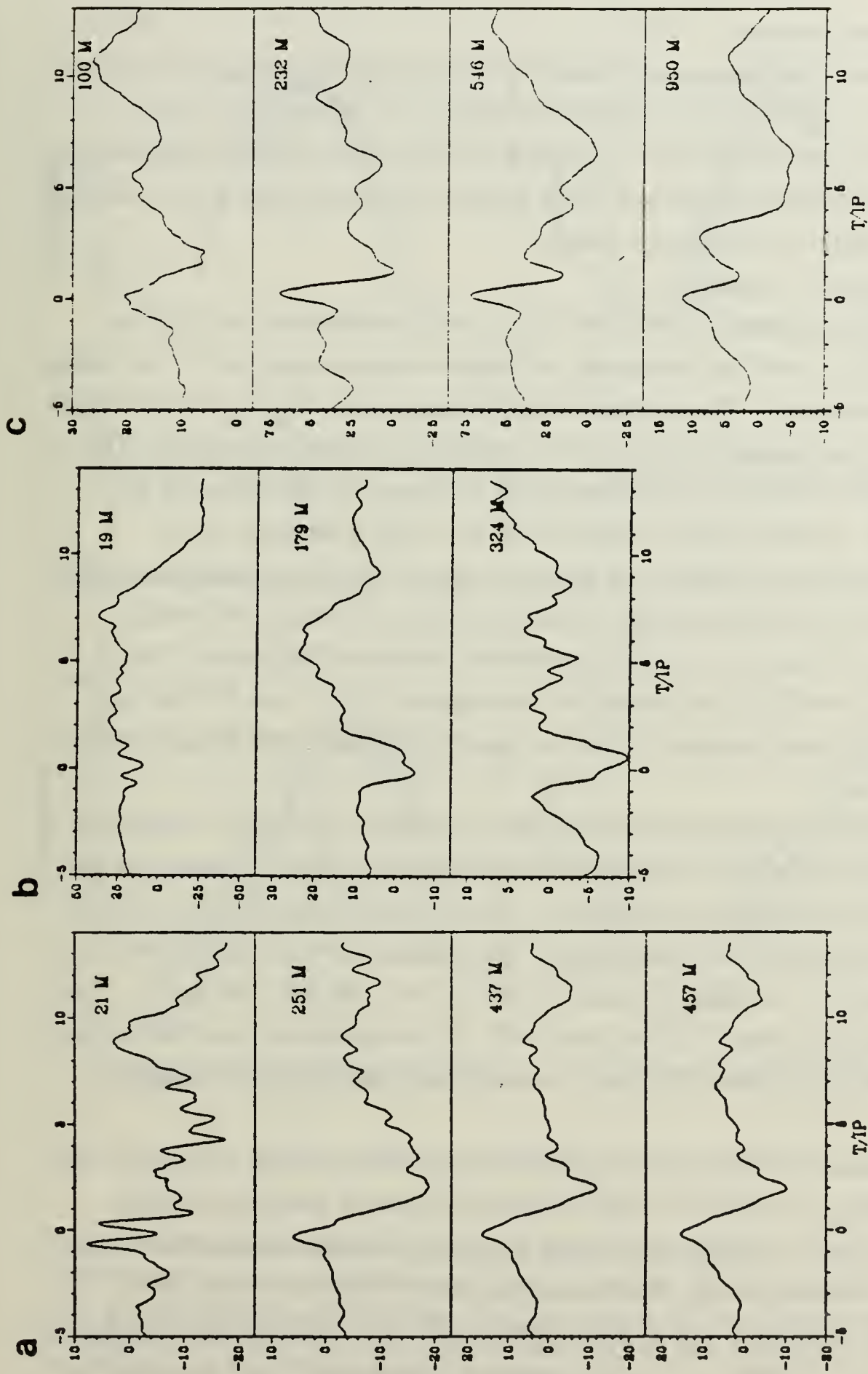
Figure 4.3 Running inertial period mean of the velocity component (cm/s) following the bottom topography at a) CMA3 (along-track), b) CMA2 (cross-track), and c) OTEC (along-track) with same time scale as in Fig. 4.2.

71

during the passage of Frederic. Thus, the mean circulation in this region may be quite complicated.

3. Frequency Analysis

Near-inertial oscillations are defined to be in the frequency range of $0.90f$ to $1.20f$ where f is the local Coriolis parameter (Mooers, 1975 ; Kunze, 1985). The Frederic data were least-squares fit to the model of Mayer *et al.* (1981) to diagnose the period of the near-inertial oscillations. For a series of trial frequencies, a set of weights (u_1, u_2) was determined from the expression

$$u(t) = u_1 \cos(\sigma t) + u_2 \sin(\sigma t) + u_R , \qquad (4.1)$$

where σ is the trial frequency $(0.90f\text{-}1.20f)$ and u_R is the residual current after the removal of the signal with that frequency. A similar expression was used for the along-track velocity component. The product of the residual currents (u_R, v_R) were averaged in time to form a covariance between the two velocity components at zero lag. The carrier frequency is defined as the frequency that minimizes the covariance of the residual currents. Because of the strength of the near-inertial response to the hurricane, it is assumed a single carrier frequency exists. The fit was performed on the data starting 12 h following the point of closest approach of Frederic to avoid contamination of the signal by the initial transient circulation (Mayer *et al.*, 1981). The current data were fit to the frequencies over segments of 1, 3 and 7 IP for each time series. More stable estimates of the near-inertial frequency were obtained with the 7 IP averages.

The variance reduction curves for CMA3 are shown in Fig. 4.4. The carrier frequency may not necessarily be aligned with these maxima, since it is defined to be the frequency that minimizes the covariance of the residual signals. Near the bottom, the diagnosed frequencies are $1.06f$ (based on the minimum covariance), but the relative maxima in the explained variance occurs at $\sigma = 1.08f$ (Fig. 4.4c and d). Thus, there is uncertainty of about $0.02f$ or about 0.4 h. In the mixed layer and thermocline, the explained variances exceed 70 % with very little uncertainty in the diagnosed frequency.

The diagnosed frequencies are generally blue-shifted between 1-6% above the local inertial frequency (Table 10) which is predicted from the mixed layer Burger number (see Table 5). This blue-shift in the frequency indicates that the forced near-inertial waves rotate faster than the local inertial period. For these values, M is roughly 0.08 in the Frederic case or a predicted blue-shift in the frequency of 0.04 in the mixed layer, which nearly equals the diagnosed frequency at CMA2 and CMA3.
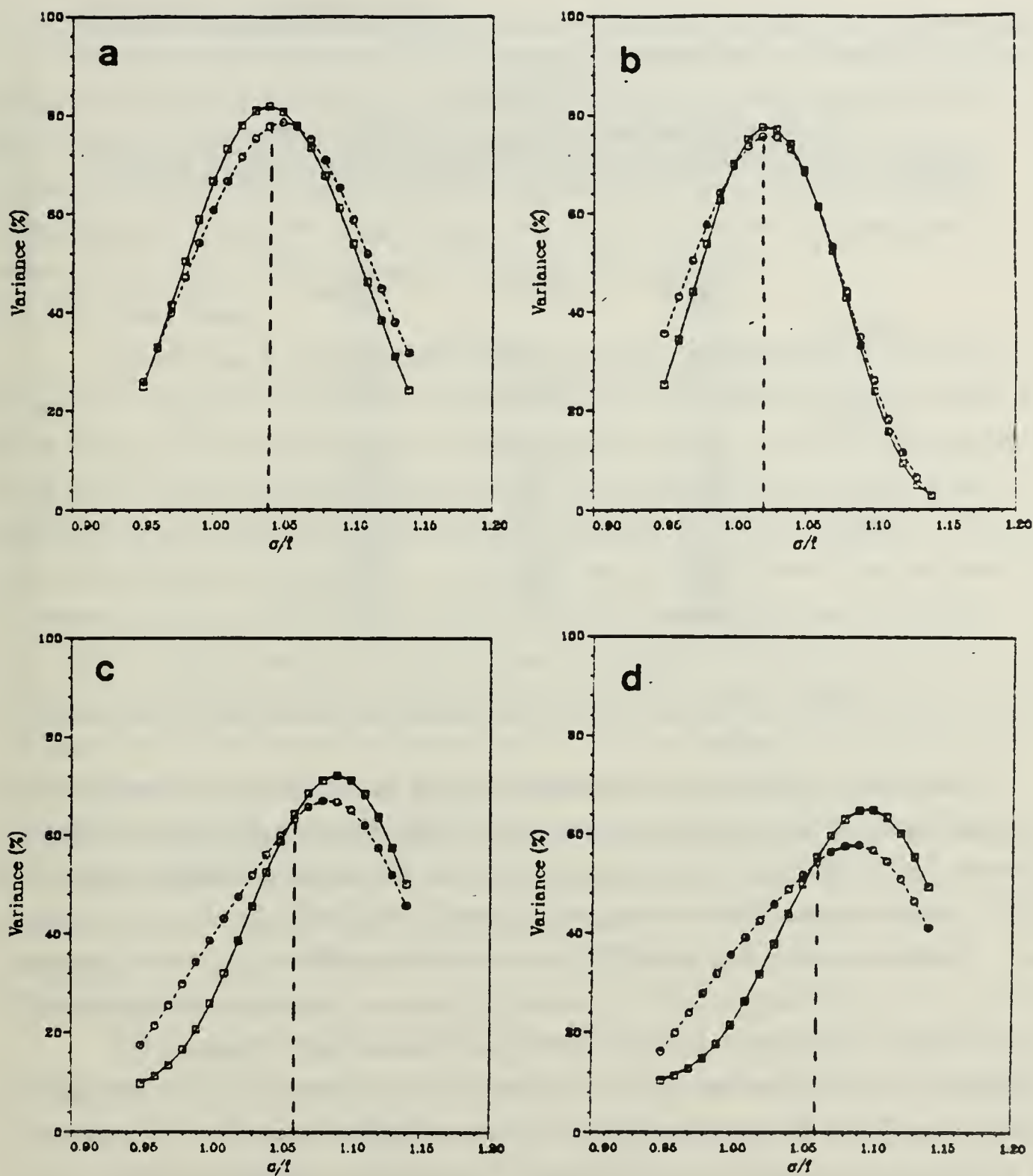
Figure 4.4 Explained variance (%) for the cross-track (solid) and along -track (dashed) velocity components at trial frequencies normalized by the local inertial frequency (σ/f) from CMA3 for a) 21 m, b) 251 m, c) 437 m, and d) 457 m. These estimates are based on least-squares fit over 7 IP. The vertical dashed line represents the frequency at which the covariance of the residual is minimized.

TABLE 10

Near-inertial frequencies (periods) at which a maximum response occurs in the observed currents based on a least-squares fit over 7 IP.

	Depth (m)	σ/f	Period (h)
CMA2			
	19	1.04	23.3
	179	1.02	23.7
	324	1.05	23.1
CMA3			
	21	1.04	23.5
	251	1.02	23.9
	437	1.06	23.1
	457	1.06	23.1
OTEC			
	100	1.04	24.8
	232	1.01	25.5
	546	1.03	25.0
	950	1.04	24.8

Since the lower order modes propagate rapidly into the interior of the fluid, a consistent blue-shift is expected with depth (Price, 1983 ; Kundu and Thomson, 1985). However, the blue-shifts in the frequencies in this case do not always increase with depth as the frequencies in the thermocline (typically 1.02f) are less than in the mixed layer. Another exception is at the OTEC site where the frequency at 232 m is less than at 100 m. The uncertainty of 0.02f in determining the exact frequencies as mentioned above can shift the frequency to that observed in the mixed layer. One possible mechanism for shifting the frequency of near-inertial waves is the mean flow (Mooers, 1975 ; Kunze, 1985). If the scale of the mean flow is comparable to the wavelength of the propagating near-inertial waves, the relative vorticity of the mean flow can effectively shift the frequency of the near-inertial waves. Thus, the frequency can be shifted above (below) f in regions of cyclonic (anticyclonic) vorticity. For example, Gaul (1967) found an anticyclonic rotating gyre in the DeSoto Canyon region that might account for the shift in frequency of the waves towards f. Unfortunately, the relative vorticity field can not be resolved with the available data in this case.

B. HORIZONTAL STRUCTURE

The near-inertial component in the time series was isolated by demodulating the ocean current and temperature data (Perkins, 1970; Otnes and Enochson, 1978). The data were multiplied by the function $\exp(j2\pi\sigma i\Delta t)$, where j is $\sqrt{-1}$, σ is the carrier frequency (see Table 10) and $i\Delta t$ represents the time at the ith data point. The data were low-pass filtered at 48 h and combined to form the amplitude and phase time series of the CW and CCW-rotating components (Mooers, 1973).

1. Mixed Layer

The increase in the CW-amplitude following hurricane passage was similar at both CMA2 and CMA3 (Fig. 4.5). The maximum CW-amplitude persisted for about 2 IP at CMA3, but at CMA2 the near-inertial amplitude started to decrease immediately. After 4-4.5 IP, the near-inertial amplitudes at CMA2 began to increase again in the mixed layer and nearly equaled the near-inertial amplitude at CMA3 after 5 IP. This time scale roughly corresponds to the time $(4t_1)$ required for the first baroclinic mode to become in-phase with the higher order modes in the mixed layer (see Fig. 10c in Gill, 1984). This provides further observational evidence of the interchange of energy between the mixed layer and the stratified fluid below (Gill, 1984 ; Kundu and Thomson, 1985). Differences in the near-inertial response between CMA2 and CMA3 may have been due to local mean currents. The mean current direction followed the bottom topography and was stronger at CMA2 than at CMA3 (see Fig. 4.3). The maximum amplitudes are about 70 and 90 cm/s after the removal of the surface wave current components at CMA6 and CMA9, respectively. At both arrays, a slight secondary increase in the CW-amplitudes is evident between 4-5 IP as observed at CMA2 and CMA3.

The energy flux from the mixed layer can be estimated using the relationship $\rho u^2 h/2T$ where ρ is the density, u is the amplitude of the near-inertial current and T is e-fold time scale of energy (5 IP). The energy flux estimate from the mixed layer based on the Frederic observations is 23 mW/m^2. Brooks (1983) reported an estimate of 10 mW/m^2 in the mid-thermocline during the passage of hurricane Allen.

Initially, the near-inertial wavelength of the ocean response is set by the scale of the wind stress curl in a hurricane (Price, 1983). The complex coefficients of the CW-rotating current vectors can be used to estimate the correlation coefficient and phase angle between two instruments over the first 7 IP (Kundu and Thomson, 1985). The phase angle is measured counter-clockwise from the CW-rotating vector at CMA2
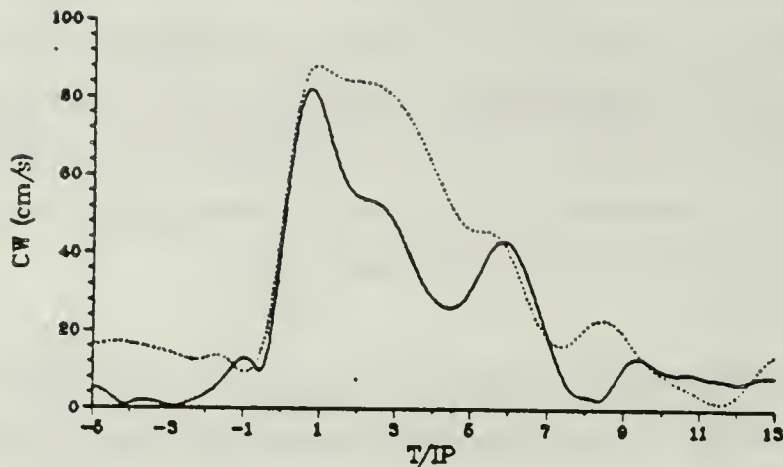
Figure 4.5 Clockwise (CW)-amplitudes (cm/s) of the near-inertial component in the mixed layer at CMA2 (solid) and CMA3 (dashed). Time scale is the same as in Fig. 4.2.

relative to that at CMA3 and is weighted by the magnitude of the instantaneous CW-rotating vectors. Assuming a plane wave relationship in a mixed layer of constant depth, the phase difference can be used to estimate spatial wavelengths (λ_r) from

$$\partial\theta/\partial r = 2\pi/\lambda_r \text{ , or}$$
$$\lambda_r = 2\pi\Delta r/\Delta\theta, \tag{4.2}$$

where Δr is the horizontal (vertical) distance between two instruments and $\Delta\theta$ is the phase difference in radians. The spatial separation between CMA2 and CMA3 is 39 km.

The phase angle between the mixed layer currents is about 55-60^0 during and subsequent to the passage of the storm (Fig. 4.6) and remains phase-locked during the period of large CW-amplitudes. The 1-h difference in time between the points of closest approach of Frederic to CMA2 and CMA3 has been incorporated into the phase. The estimated wavelength from (4.2) is 240-260 km, which is roughly 8 R_{max} or four times the scale of the wind stress curl (60 km). The 250 km wavelength agrees with the estimated wavelength of the first baroclinic mode that is derived from the Sturm-Liouville problem using a variable N^2 profile (see Table 6). Black (1983) also observed wavelengths of 240 km in the AXBT data acquired during the passage of hurricane Frederic. However, linear theory by Geisler (1970) suggests that the horizontal wavelengths should be much larger. For a storm speed of 6.5 m/s and IP = 24.4 h, the predicted wavelength should be about 550 km. The horizontal wavelengths

of the ocean response to hurricane Allen (370 km) were also less than predicted by Geisler's linear theory (Brooks, 1983). Because the mechanism that forces these shorter horizontal wavelengths of the near-inertial response is related to the wind stress curl (Price, 1983; Greatbatch, 1984), the wavelength associated with the near-inertial response varies with each hurricane.
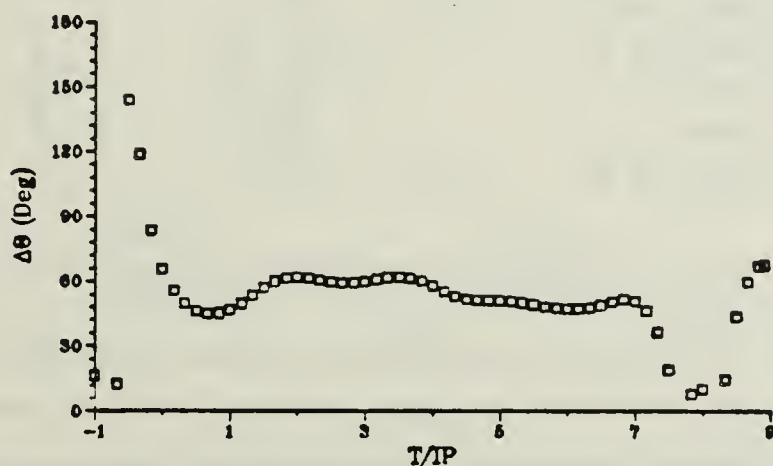
Figure 4.6 CW-phase in the mixed layer currents between CMA2 and CMA3. The start time is 21 UTC 11 Sept. and ends 21 UTC 19 Sept. and represents the period of significant CW-amplitudes in Fig. 4.5.

The CW-rotating phases (Table 11) are compared at the various array sites. These additional arrays provide five more estimates of the horizontal wavelengths of the near-inertial response, thus increasing the confidence in the estimate of the near-inertial wavelength based on CMA2 and CMA3. In these other five cases, there is a phase-locking of large CW-rotating amplitudes over the first 5 IP in the mixed layer (as in Figs. 4.5 and 4.6). The corresponding estimates of wavelengths are comparable to the 250 km wavelengths estmated between CMA2 and CMA3 and range between 200-300 km. Thus, the wavelength of the near-inertial response in the far-field agrees with the excitation of an energetic first baroclinic mode.

2. Thermocline

Significant increases in the CW-amplitudes above the background level occurred in the thermocline (Fig. 4.7) at all the moorings and continued for 18-21 IP subsequent to storm passage. However, there are some marked differences in

TABLE 11

Differences in the CW-rotating phases in the mixed
layer between the various arrays in hurricane Frederic averaged over 5 IP.

Arrays	$\Delta\Theta$ ($^{\circ}$)
CMA6 vs. 9	70
CMA2 vs. 6	15
CMA2 vs. 9	63
CMA2 vs. 3	57
CMA6 vs. 3	63
CMA3 vs. 9	12

thermocline current response. At CMA3, the amplitude increased to 28 cm/s as the storm passed through the region. After the time scale associated with the first baroclinic mode (t_1 = 25 h), the amplitude decreased by about 10 cm/s to a relative minima of 18 cm/s. Thus, it appears that the first mode indeed separates from the remainder of the modes after 25 h and there is a relative minima in the amplitudes by 50 h ($2t_1$). This is consistent with the linear theory of Gill (1984), who suggests that at $2t_n$, the nth baroclinic mode will be 180^0 out of phase with the remainder of the modes and the amplitudes should be near a relative minima. After 50 h ($2t_1$), the amplitude began to increase slightly by about 4-5 cm/s. During the period from t_2 to $2t_2$ (7.5-15 IP), the CW-amplitude increases significantly to nearly 30 cm/s. Although the relative minima occurs at about 16.5 IP rather than the expected 15 IP, this is considered to be fairly good agreement between the relative extrema of the CW-amplitudes and the predicted time scales. There is also another peak in the amplitude after 19 IP that may correspond to the separation of the third baroclinic mode. The CW-amplitudes at CMA2 (Fig. 4.7b) decreased to pre-storm values and then increased again at roughly 5 1P, whereas the secondary maxima occurred after 7 IP at CMA3. One possibility is that there may be slight differences in the phase speed of the second baroclinic mode at CMA2 since the water is about 130 m shallower and there are some differences in the N^2 profile at station 1 (Fig. 2.4). The CW-amplitude again approached a relative minima after 10 IP or roughly twice the time scale associated

with the secondary maxima. Initially, the CW-amplitudes in the thermocline at CMA6 and CMA9 increased to about 20 cm/s followed by a decrease of about 10 cm/s. After about 5-7 IP, there were similar increases in the amplitudes, which exceeded 20 cm/s at CMA6 and CMA9.
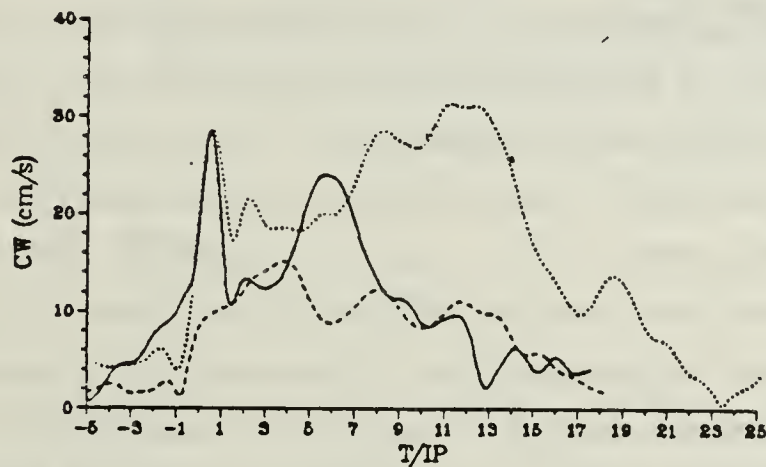
Figure 4.7 CW-amplitudes (cm/s) of the near-inertial component in the thermocline at CMA2 (179 m, solid), CMA3 (251 m, dotted) and OTEC site (232 m, dashed) starting on 21 UTC 7 Sept. and ending 21 UTC 8 Oct..

In the thermocline (232 m) at the OTEC site, the amplitudes increased nearly four-fold over the background level to about 10 cm/s. However, a very large peak similar to that at CMA2 and CMA3 was not observed immediately following storm passage. The time difference in storm passage between the DeSoto Canyon and the OTEC site was about 1/2 IP. Taking this time differential into account, the estimated wavelength in the thermocline also approaches the 240 km observed by Black (1983) in the DeSoto Canyon region and estimated above from the horizontal phase differences in the mixed layer.

C. VERTICAL STRUCTURE

At CMA2 (Fig. 4.8a), the initial maxima were 28 and 10 cm/s in the thermocline and near-bottom layers as at CMA3. After 6 IP, the thermocline and near-bottom CW-amplitudes were equal (20 cm/s) and were roughly half the secondary maxima of the mixed layer amplitude. The amplitudes then gradually decreased to pre-storm levels after 12 IP. The thermocline and near-bottom amplitudes at CMA3 increased to

about 33 and 22 cm/s, respectively (Fig. 4.9b). The CW-amplitude in the near-bottom layers approached zero within an IP in association with an abrupt phase change. Within the next 4 IP, the CW-amplitude near the bottom exceeded the amplitude in the thermocline and then approached a maximum of 25 cm/s about 7 IP following storm passage. Notice that another maxima of 25 cm/s occurred in the thermocline after 8 IP.

The 10 cm/s amplitudes at a depth of 950 m at the OTEC Site (Fig. 4.9c) demonstrates an ocean response to hurricane forcing throughout the water column. Brooks (1983) also observed a near-inertial response close to the bottom at 700 m during the passage of hurricane Allen. At the OTEC site, the maximum CW-amplitudes in the thermocline occurred at 232 m rather than at 100 m. Because the CCW-amplitudes at 100 m were more energetic than the CW-amplitudes, this may be the influence of the shear zones on the edges of the CW-rotating Loop Current in the Gulf of Mexico. That is, the current meter at 100 m may have been engulfed by the CCW-rotating shear on the periphery of the Loop Current (Molinari and Mayer, 1982).

At all three moorings, the phases between the vertical levels started to converge a few hours prior to the closest approach of hurricane Frederic (Fig. 4.9). Generally, there was about a 90 $^{\circ}$ phase change between the mixed layer and the thermocline at CMA2, CMA3, CMA6 and CMA9 as predicted by Price (1983). The near-inertial response below the mixed layer was nearly in-phase at all three moorings, which suggests a low-mode response in the vertical. Higher order modes may be present that cannot be detected with the limited sampling in the vertical, but the possibility of all the current meters simultaneously sampling at the nodes at each level is quite remote (J. F. Price, 1982, personal communication). The AXCP data acquired in hurricane Norbert to be described below provide the vertical resolution necessary to calculate the amount of energy in the higher order baroclinic modes.

Since the initial phase differences were about 90° between the mixed layer and thermocline, the vertical wavelengths estimated from (4.2) exceeded 1000 m. Since the water depths at the three current meter array sites were 340, 465 and 1050 m, the low-order modes (large vertical wavelengths) contributed significantly to the near-inertial variability. The 1000 m vertical wavelength is roughly five times the scale of the thermocline (about 200 m) and is consistent with the vertical wavelengths derived in Eloise simulations (Price, 1983) and the hurricane Allen observations (Brooks, 1983).
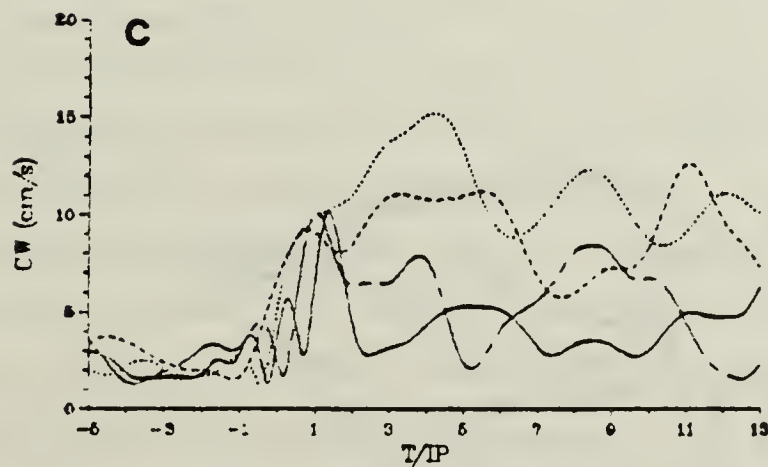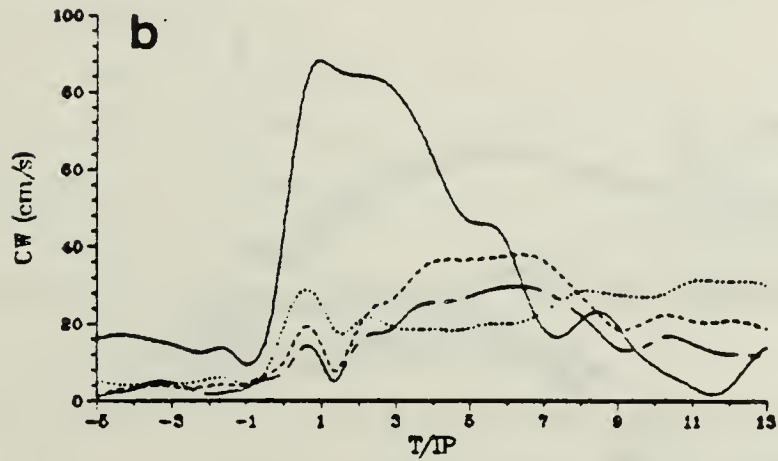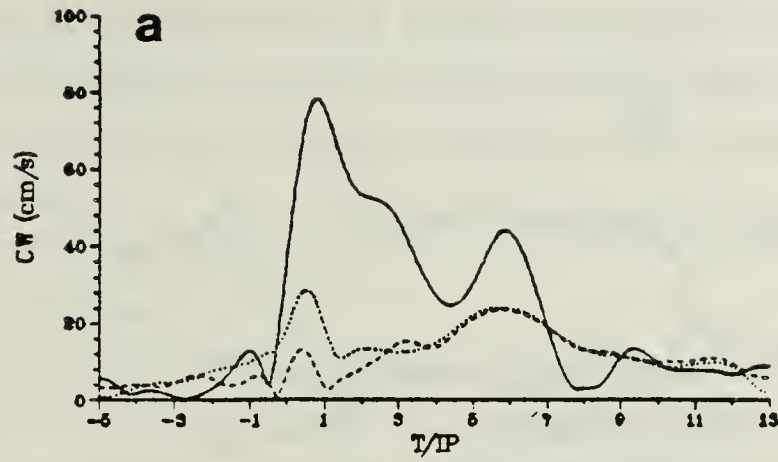
Figure 4.8 CW-amplitudes from a) CMA2 at 19 m (solid), 179 m (dotted), and 324 m
(dashed) ; b) CMA3 at 21 m (solid), 251 m (dotted), 437 m (dashed), and 457 m (chain-
dash); and c) OTEC at 100 m (solid), 232 m (dotted), 546 m (dashed), and 950 m
(chain-dash).Time scale is the same as in Fig. 4.2.

81
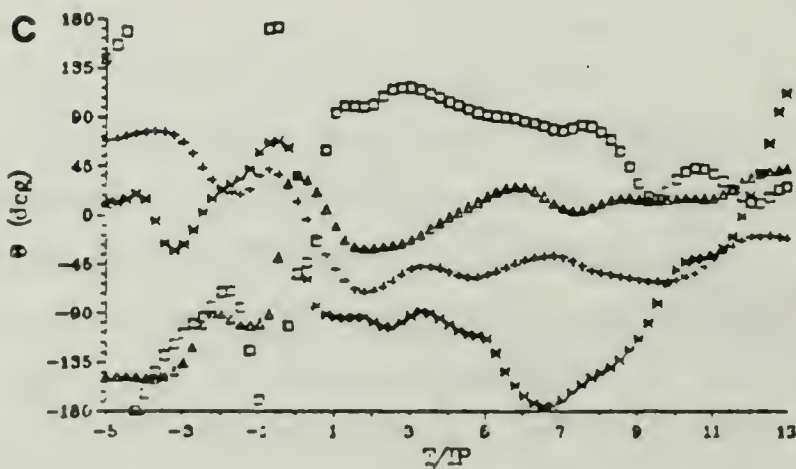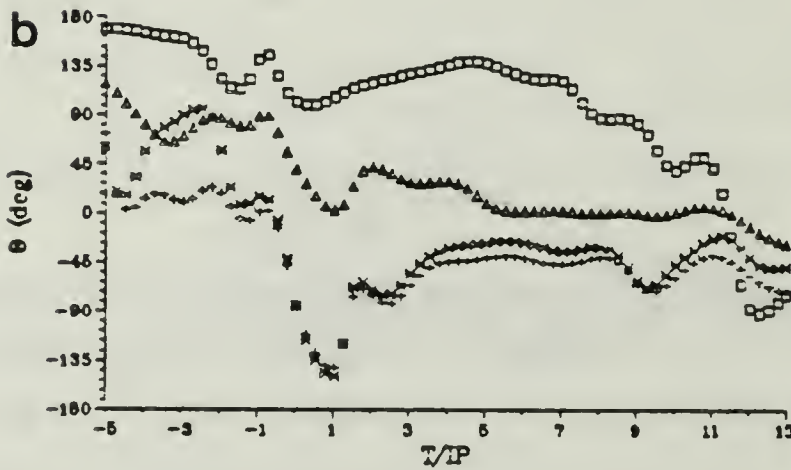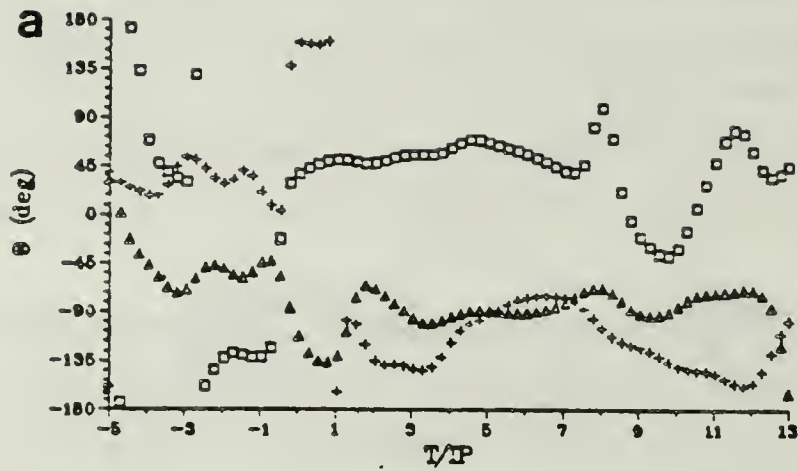
Figure 4.9 CW-phases from a) CMA2 at 19 m (square), 179 m (triangle) and 324 m (plus) ; b) CMA3 at 21 m (square), 251 m (triangle), 437 m (plus) and 457 m (xdash); and c) OTEC at 100 m (square), 232 m (triangle), 546 m (plus) and 950 m (xdash) every 6 h. Time scale is the same as in Fig. 4.2.

D. VERTICAL AND HORIZONTAL ENERGY PROPAGATION

The vertical and horizontal group velocities at which energy propagates are calculated from the dispersion relationship for the baroclinic modes of near-inertial waves (Brooks, 1983)

$$c_v = -(\sigma/m)(N^2/\sigma^2)\tan^2(\varphi), \tag{4.3}$$

$$c_h = (\sigma/K)(N^2/\sigma^2)\tan^2(\varphi), \tag{4.4}$$

where σ is the observed frequency, m and k are wavenumbers in the vertical and horizontal directions, and $\tan(\varphi) = k/m$. The wavenumbers m and k are equal to $2\pi/\lambda_v$ and $2\pi/\lambda_h$, respectively, where λ_v and λ_h represent the vertical and horizontal wavelengths estimated above. The mean and one standard deviation values assigned to the variables in (4.3) and (4.4) are :

$\sigma = (7.45 \pm 0.12) \times 10^{-5}$ rad/s,

$N = (6.60 \pm 0.71) \times 10^{-3}$ rad/s,

$m = (6.28 \pm 0.17) \times 10^{-3}$ rad/m,

$k = (2.51 \pm 0.11) \times 10^{-5}$ rad/m.

Note that in estimating the energy propagation, the Brunt-Väisälä frequency profile was averaged in the upper 250 m of the water column.

The vertical group velocity (Table 12) associated with the 1000 m vertical wavelength is 0.15 cm/s $\pm$ 0.05 cm/s. This estimate of group velocity, which is associated with the first baroclinic mode, is within one standard deviation of the 0.12 cm/s from Price (1983) and slightly larger than the estimate of 0.07 cm/s from the hurricane Allen observations (Brooks, 1983). The direction of the energy propagation is downward from the mixed layer into the thermocline for surface-intensified flow. For downward propagating wave groups associated with baroclinic modes, Leaman and Sanford (1975) showed that phase propagation is upward. After the phases began to separate, the vertical wavelengths were about equal to the water depth, which is indicative of a mode 2 response. The vertical group velocity is then 0.03 $\pm$ 0.02 cm/s, which is an order of magnitude less than during the hurricane forcing period.

The horizontal group velocity of the first baroclinic mode is 0.4 m/s. The estimates from the Eloise simulations (Price, 1983) and Allen observations (Brooks, 1983) were 1 and 0.3 m/s, respectively. The discrepancy between the Eloise and the first baroclinic mode is due to the difference in horizontal wavenumber. The rate of energy propagation agrees with the group velocity estimated from the Allen observations (Brooks, 1983).

TABLE 12

Vertical (c_{vn}) and horizontal group velocity (c_{hn})
for the first two baroclinic modes estimated from the dispersion relation.

n	c_{vn} (cm/s)	c_{hn} (m/s)
1	0.15	0.4
2	0.03	0.1

As noted above, the rates of energy propagation depend on the horizontal and vertical wavenumbers (4.3, 4.4). These wavenumbers inferred from CMA6 and CMA9 are nearly equal to those derived from the other arrays. Thus, the estimates of group velocity from the other two arrays are not significantly different from the above values.

E. MODAL ANALYSIS

1. Flat Bottom Modes

Consider the case in which the bottom is flat, with the depth D = constant. The Sturm-Liouville problem is solved using a constant Brunt-Väisälä frequency (N = 2.15 x 10^{-3} rad/s), which was derived by vertically averaging the profile over the entire water column to compare to a constant N model with a sloping bottom (Lai and Sanford, 1986). The free mode model (Chap. III) is solved using a flat bottom ocean where the flow normal to the bottom is zero ($\varphi_n = 0$ at z = -D) and a free surface boundary condition that pressure is continuous across the interface,

$$\frac{d\varphi_n}{dz} = \frac{g}{(\sigma^2 - f^2)} k^2 \varphi_n \quad .$$

Equation (3.6) along with these boundary conditions constitutes a Sturm-Liouville problem for which any number of modes satisfy the relation. Since the oceanic response to hurricanes is dominated by the low-order modes (large vertical wavelength), this assumption is reasonable. Leaman and Sanford (1976) point out that as the vertical wavelengths (higher order modes) decrease, stratification effects become increasingly important. The resulting amplitudes of the horizontal velocity eigenfunctions for modes 0, 1 and 2 at CMA3 are shown in Fig. 4.10. The eigenfunctions of the horizontal velocity at all of the array sites are similar.
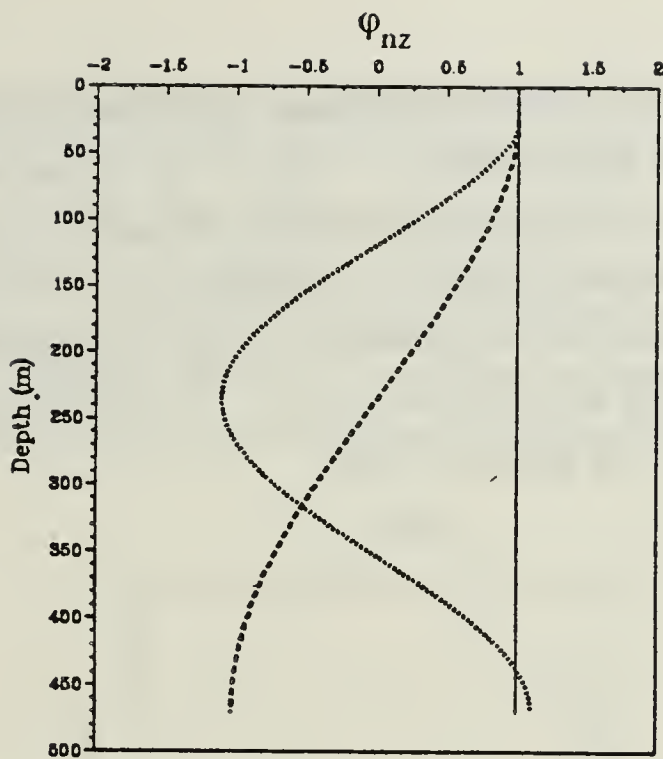
Figure 4.10 Amplitude of the horizontal velocity eigenfunctions for the flat-bottom mode 0 (solid), mode 1 (dashed) and mode 2 (dotted). The physical parameters are N = 2.15 x $10^{-3}s^{-1}$, σ = 1.04f and D = 500 m.

2. Bottom Slope Modes

For the current meter measurements acquired in the DeSoto Canyon, a bottom slope (typically α_{ss} = 6×10^{-3}) is introduced into the model. Wunsch (1968, 1969) studied the propagation of internal waves up a slope using a constant N model. Lai and Sanford (1986) extended the model to include rotational effects. The model assumes a wedge-shaped, linear bottom-slope of the form z = $-\alpha_s x$. The kinematical boundary conditions at the ocean surface and bottom in terms of the perturbation streamfunction (ψ) are: $\psi(x,0)$ = 0 and $\psi(x,-\alpha_s x)$ = 0

In this case, (3.6) is no longer separable and the waves differ considerably from simple plane waves. Lai and Sanford (1986) showed that the propagating wave solutions are

$$\psi_n(x,z) = \exp(\pm jq(\ln(\gamma x-z))) - \exp(\pm jq(\ln(\gamma x + z))),$$

where $q = 2n\pi/\ln(\gamma+\alpha_s)/(\gamma-\alpha_s)$, $\gamma^2 = (\sigma^2 - f^2)/(N^2 - \sigma^2)$ is the slope of the internal wave characteristic, and +(-) refer to downward (upward) energy propagation. The perturbation streamfunction is related to the currents in the usual manner, *viz.* u = $-\partial\psi/\partial z$, w = $\partial\psi/\partial x$. The baroclinic modes are affected the most by the sloping bottom.

It should be noted that the two-dimensional, linear wedge, eigenvalue problem is sensitive to variations in N and x, where $x > D/\alpha_s$. If the bottom slope is supercritical ($\alpha_s > \gamma$), the waves are reflected seaward and cannot propagate up the slope onto the shelf. A subcritical condition is appropriate at CMA3 since $\alpha_s < \gamma$. The resulting amplitudes associated with downward energy propagation for modes 1 and 2 of the horizontal velocity are shown in Fig. 4.11. Notice the increased, near-bottom amplitude induced by the sloping bottom.
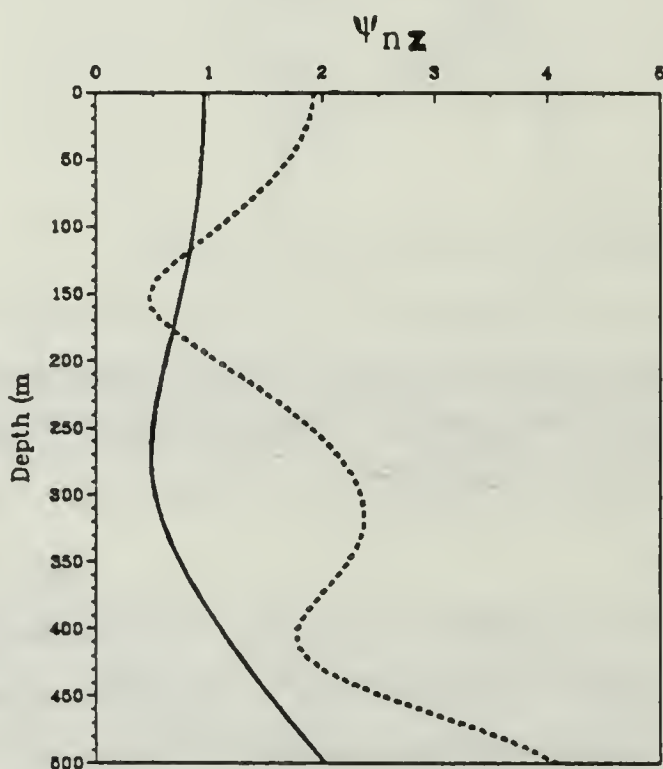
Figure 4.11 Amplitude of the horizontal velocity eigenfunctions for the slope mode 1 (solid) and mode 2 (dashed). The physical parameters are the same as in Fig. 4.10, except that $x = 85$ km and $\alpha_s = 6 \times 10^{-3}$.

3. Data Analysis

Since the modal contributions can contain both CW and CCW-rotating components (Leaman, 1976), only the real part of the velocity amplitude was least-squares fit to the first two baroclinic, flat and sloping bottom modes after the vertical average was removed from the time series. The data analysis concentrates on the large vertical scales for two reasons : 1) only three or four observations are available in the column; and 2) the far-field response is dominated by low-order modes (Price, 1983 ; Lai and Sanford, 1986).

The time evolution of the CW-amplitude coefficients at CMA3 indicate that the storm excited both vertically-averaged flow and baroclinic modes (Fig. 4.12). As

shown in previous studies, the baroclinic modes dominated the near-inertial response to hurricane Frederic and were considerably more energetic than the depth-averaged flow. The mode 2 current exceeded 16 cm/s and gradually decreased to 8 cm/s after about 7 IP. The first baroclinic mode also increased significantly above pre-storm levels. The amplitude then increased to a secondary maximum of about 24 cm/s after 3-4 IP. After this secondary maxima in the mode 1 amplitude, the amplitude decreased rapidly as the second baroclinic mode dominated the response after 7 IP.
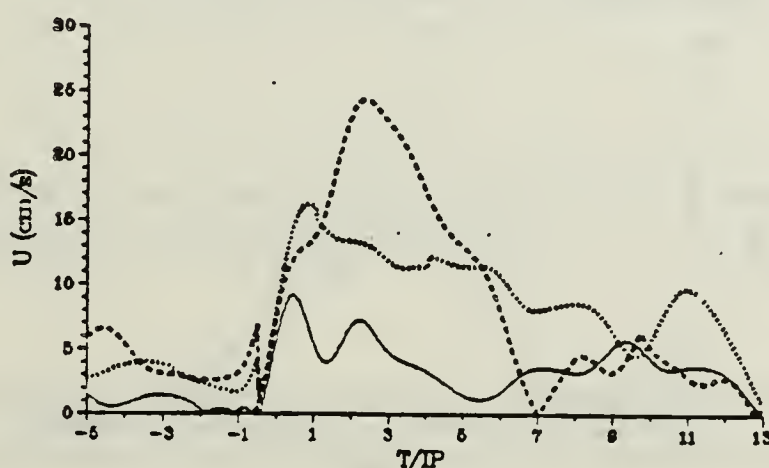
Figure 4.12 Velocity coefficients at CMA3 for depth-averaged mode (solid), mode 1 (dashed), and mode 2 (dotted). Time scale is the same as in Fig. 4.2. The biases for each mode have been applied to the appropriate curves to represent the amount of aliasing due to limited vertical sampling as described in the Appendix C.

The depth-averaged flow reached a peak amplitude of about 7-9 cm/s during the spin-up phase and then decreased to a relative minimum within an IP (Fig. 4.12). After a few IP, the depth-averaged flow decreased to about 4 cm/s. This initial amplitude is comparable to the 4-8 cm/s current amplitudes induced by the free-surface slope, which will be addressed further in Chapter VI. It should be noted that the wavelength of the barotropic mode is 4700 km, whereas the basin scale in the Gulf of Mexico is 1500 km. Thus, it seems unlikely that the basin will admit a barotropic mode excited by hurricane passage. Geisler (1970) showed that the relevant parameter associated with the barotropic mode is the deformation radius (1000 km) rather than the horizontal wavelength. Although it is unclear at this point whether Frederic

excited a barotropic response, it certainly excited a non-zero, depth-averaged component.

The modal time series are reconstructed at each depth by multiplying the modal coefficients by the appropriate eigenfunctions for that depth. The residual amplitudes are estimated by subtracting the modal series from the data (Fig. 4.13). The residual currents are smaller if the depth-averaged current is extracted from the data series prior to the least-squares fit. The residual amplitudes reach a maximum of 7-8 cm/s after 4 IP and then decrease gradually to zero by 8 IP.
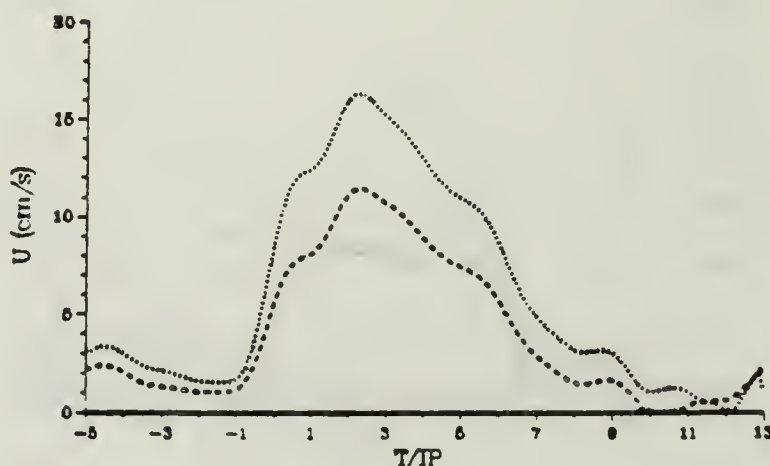
Figure 4.13 Residual variances for the flat bottom (dashed) and sloping -bottom (dotted) least squares fit with the vertical-average removed. Time scale is the same as in Fig. 4.2.

The amplitudes of the baroclinic modes (Fig. 4.14) for the sloping bottom model were greater than in the flat-bottom case. Initially, the amplitude of the first baroclinic slope mode was 8 cm/s larger than the flat bottom mode 1 amplitude, whereas the second bottom-slope mode amplitude increased by about 10 cm/s. The maximum differences between the flat and sloping bottom amplitudes occurred after about 2 IP and were 11 and 16 cm/s for modes 1 and 2, respectively. The residual amplitudes (see Fig. 4.13) associated with the slope mode fits generally decreased by about 2-3 cm/s, which indicates that more of the observed variance can be explained by the bottom-slope modes.
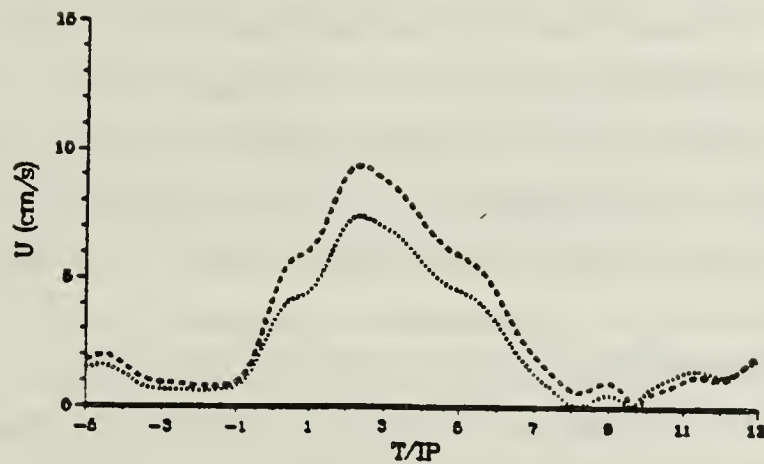
Figure 4.14 Differences in the sloping bottom and flat-bottom modes 1 (dashed), and mode 2 (dotted). Time scale is the same as in Fig. 4.6.

An estimate of the amount of aliased energy was made by attempting to represent the currents from a 15-level baroclinic model (Adamec *et al.*, 1981) with only three currents at the same depths as at the NAVOCEANO arrays (see details in Appendix C). The difference in the amplitudes between the 15-level and 3-level fits is an indication of the bias induced by limited vertical sampling. The biases in the first two baroclinic modes are 6 and 4 cm/s, whereas the discrepancy between the depth-averages is 2 cm/s. These biases in modal amplitudes were applied by creating a time series with a phase of $\pi/2$ about 5 h prior to the point of closest approach.

The contributions of the baroclinic modes to the mixed layer amplitudes can be estimated from the product of the mixed layer eigenfunctions (unity in the mixed layer) and the modal coefficients. After accounting for the bias in the modal coefficients, the mode 1 and 2 contributions were about 13 and 16 cm/s, respectively. Since the total amplitude in the mixed layer was about 90 cm/s, the percentage of the amplitude accounted for by the first two modes is 33 %. Gill (1984) estimated amplitudes of 13 and 14 cm/s for the first two baroclinic modes for a mixed layer depth of 50 m (see his Table 1). Since the initial mixed layer amplitude in that study was 100 cm/s, the amount of baroclinic energy in the mixed layer was 27 % of the total.

During the period of the enhanced mode 1 amplitude (3 IP), the total contribution of the baroclinic modes to the mixed layer was about 37 cm/s or roughly 41 %. Thus, the amplitudes associated with the first two baroclinic modes estimated from Frederic data are within 10 -15 % of theoretical results derived from linear theory.

The modal coefficients are then used to estimate the amount of variance associated with the summation of the depth-averaged flow and the first two baroclinic modes. The evolutions of the explained variances averaged over an IP are given in Table 13 for the flat- and sloping-bottom modes at CMA3. The flat-bottom mode 1 contributed 38% while the bottom-slope mode 1 accounted for 41 % of the variance over the first IP. The contributions from the first mode increased to a maximum over the following 3-4 IP for both the flat and sloping bottom cases. There was also an increase in the amount of explained variance by mode 2 (30-40 %) after 7 IP. Similar contributions from mode 2 are found in the sloping-bottom model with a further increase in the explained variances by 6 %. Hence, the increases in the thermocline amplitude 6-8 IP after storm passage appear to be associated with the second baroclinic mode.

TABLE 13

Explained current variances at CMA3 for the depth-averaged and first two baroclinic modes in the flat-(F) and sloping-(S) bottom models.

	F			S		F	S
IP	0	1	$\Sigma(1+2)$	1	$\Sigma(1+2)$	$\Sigma(0+1+2)$	$\Sigma(0+1+2)$
0	0.33	0.50	0.86	0.49	0.87	0.80	0.83
1	0.34	0.38	0.72	0.41	0.80	0.65	0.69
2	0.18	0.40	0.79	0.36	0.84	0.72	0.78
3	0.27	0.60	0.88	0.53	0.89	0.80	0.85
4	0.19	0.68	0.83	0.65	0.82	0.81	0.82
5	0.13	0.62	0.69	0.73	0.66	0.71	0.68
6	0.06	0.54	0.55	0.69	0.59	0.57	0.59
7	0.19	0.24	0.42	0.46	0.54	0.31	0.45
8	0.20	0.11	0.56	0.11	0.60	0.43	0.55
9	0.24	0.20	0.50	0.15	0.64	0.47	0.60
10	0.23	0.17	0.45	0.25	0.51	0.57	0.62

A sum of the depth-averaged flow and first two baroclinic modes at CMA3 explained 62 % and 68 % of the variance over the first 10 IP for the flat- and sloping-bottom models, respectively. The depth-averaged current contributed about 21 % to the observed near-inertial wave variance over the first 10 IP. The first baroclinic mode accounted for 40 % of the current variations, whereas the second baroclinic mode contributed about 25 % in the flat-bottom case. By contrast, the first baroclinic bottom-slope mode accounted for about 45 % of the near-inertial variance. Thus, the increases in the explained variances by the first two bottom-slope modes were about 5 % and 6 % , respectively.

At CMA2, the depth-averaged term accounted for 25% of the variability of the near-inertial response, and a sum of the modes explained 52 % of the variance. The second baroclinic mode was more energetic than mode 1 by about a factor of 3. A sum of the modes at the OTEC site contributed about 62 % to the near-inertial variance. However, some caution has to be applied to these results in light of the intermittency of the forced near-inertial response at 100 m.

At CMA6 and CMA9, the depth-averaged components ranged from 5-9 cm/s and accounted for about 20 % of the observed near-inertial variance. The amplitudes of the first two baroclinic modes were within 3-5 cm/s of those estimated from the modal analyses at CMA2 and CMA3. Furthermore, the modal response was dominated by the first baroclinic mode.

In comparison, the modal decomposition of vertical current profiles into the first three baroclinic modes during the passage of hurricanes Dawn and Carrie explained 55 and 73 % of the variance for the flat and bottom-slope models, respectively (Lai and Sanford, 1986). Their results clearly showed a fairly significant change in modal contributions by including a sloping bottom. The velocity profiles collected during STREX show that higher order modes are excited by the passage of a storm, but most of the energy seems to be concentrated in a mode 2 response (D'Asaro, 1984). The low-mode response determined from the Frederic observations is consistent with these earlier studies except that the depth-averaged mode also contributes to the variability.

F.   SUMMARY

Analyses of the moored current meter measurements indicate that the forced near-inertial waves have frequencies that are blue-shifted above the local inertial period, large CW-rotating amplitudes and wavelengths of the first baroclinic mode.

This estimate of wavelength (250 km) is similar to the findings of Black (1983) using the AXBT measurements made in the vicinity of the current meter arrays.

The time-evolution of the first two baroclinic modes is similar to the predictions from linear theory (Gill, 1984). The secondary increases in the CW-rotating amplitudes in the mixed layer and in the thermocline are correlated to the time scales associated with the first two baroclinic modes. The vertical structure of the near-inertial response can be described by a sum of the depth-averaged and first two baroclinic modes. The addition of the bottom slope accounts for 5-8 % more of the near-inertial variability.

The critical issue raised by these calculations is the role of the depth-averaged or barotropic component in the near-inertial frequency band. At all of the arrays (including OTEC), there was a significant increase in the current amplitudes during the passage of Frederic. Because of limited vertical sampling, some higher mode energy may have been leaked into the barotropic mode which has amplitudes of 7-10 cm/s. This issue is addressed in Chapter VI using numerical simulations from a free surface model.

V. VERTICAL STRUCTURE

The primary motivation for this chapter is to determine the number of baroclinic modes that are required to describe the near-inertial ocean current response in the near-field. Since the current meter moorings only provided data at selected depths, the least-squares fit may have aliased some of the higher mode energy into the low baroclinic modes. Thus, the near-inertial response in the ocean current profiles acquired during hurricane Norbert are decomposed into the first three or four baroclinic modes using the forced, linear theory in Chapter III.

A. SYNOPTIC SCALE PICTURE

1. Mixed Layer

Previous studies of the oceanic response to hurricane passage using AXBT observations have documented a crescent-shaped pattern of sea-surface temperature patterns (Black, 1983). The maximum temperature decreases of 2-3 °C in the mixed layer occur on the right side of the hurricane at about 1-2 R_{max} behind the storm center. Numerical studies also demonstrate this rightward bias of upper ocean processes (Chang and Anthes, 1978 ; Price, 1981).

In hurricane Norbert (Fig. 5.1a), the maximum cooling region is located to the rear of the storm at roughly $2R_{max}$. The minimum mixed layer temperature is 25.7 °C, which represents a decrease of 2.6 °C relative to the observed temperature ahead of the storm. Over the remainder of the domain, the mixed layer temperatures exceeded 27 °C.

The distribution of mixed layer depths in Norbert correspond to the pattern of mixed layer temperature decreases (Fig. 5.2). The mixed layer depth decreased only to 18 m at roughly 90 km (2-4 R_{max}) in the wake of the storm where peak upwelling occurs. Strong vertical advective processes are associated with the upwelling of cool water, which tends to form a shallower mixed layer and indirectly enhances entrainment mixing and surface cooling. On the right side of the track, the mixed layer deepened to depths of 40 m or more.

Maximum mixed layer currents in the wake of Norbert exceeded 1 m/s at roughly 2-4 R_{max} (Fig. 5.2b) in the same region as the minimum in mixed layer temperature and depth. Sanford *et al.* (1987) also observed similar maximum velocities
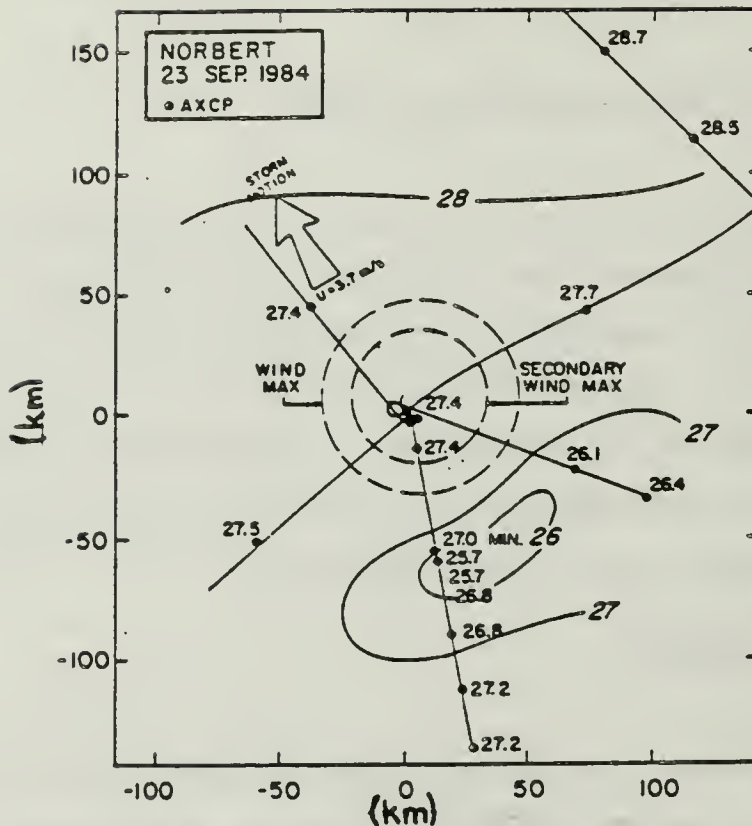
Figure 5.1 Sea-surface temperature patterns (°C) in hurricanes Norbert with the primary and secondary radii of maximum winds as depicted by the quasi-circular dashed lines and the direction of the storm movement is indicated by the double arrow.

in the three-layer model fits to the observations. The general pattern of mixed layer currents agrees with the divergent upwelling and convergent downwelling regimes predicted from numerical studies (Price, 1981) and shown in analytical studies (Geisler, 1970). Undoubtedly, larger current speeds existed at the surface, but these could not be measured by the AXCP.

2. Thermocline

The thermocline current (80 m) pattern in Norbert was anticyclonic and exceeded 40 cm/s (Figure 5.3). In the region of maximum mixed layer currents and strong upwelling, the difference in the directions of the currents between the mixed layer and thermocline is only 40 -60 °. Over the remainder of the domain, the direction of the thermocline currents is nearly opposite to the mixed layer current, which suggests a low baroclinic mode response (discussed below). The considerable vertical current shears in the upper ocean are presumably associated with near-inertial processes. Thus, a fairly large area of near-critical Richardson numbers (shown below) (< 1) is located in the regions of largest mixed layer temperature decreases. These calculations of Richardson numbers are the first confirmation of this physical process
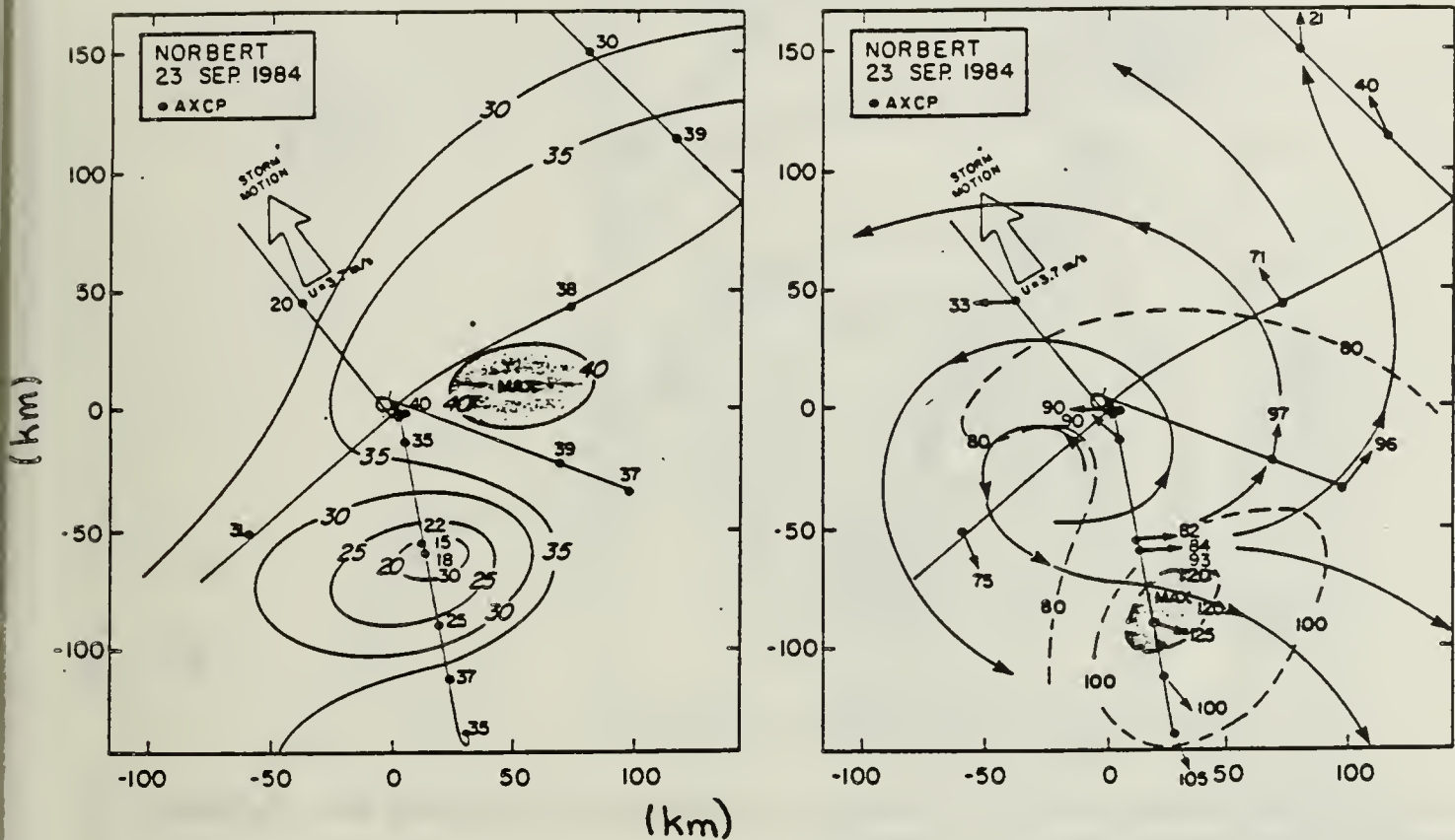
Figure 5.2 Mixed layer depths (m) (left) and mixed layer currents (cm/s) in Norbert with the shaded regions depicting the regions of maximum mixed layer depths (> 40 m) and currents (> 120 cm/s).

that has been generally assumed in numerical treatments of the oceanic response to hurricanes (Price, 1981). However, surface-generated mixing is also a possibile explanation because of high surface winds and very shallow mixed layers.

B. VERTICAL STRUCTURE

1. Vertical Wavenumber Spectra

A Tukey data window (Otnes and Enochson, 1978) is applied to the current profiles prior to the removal of the mean in the calculation of the energy spectra. The data are transformed and spectrally-averaged over bandwidths to help decrease leakage of energy to adjacent frequency bands (Otnes and Enochson, 1978). Energy above the Nyquist wavenumber ($1/2\Delta z$ where Δz is the 3-m sampling interval) is eliminated to minimize aliasing of the spectra.

The vertical wavenumber (m) spectra of the kinetic energy (KE) are compared to the background internal wave spectra of Garrett and Munk (1975). The form of the spectra used in this intercomparison is similar to that of Leaman (1976)

$$KE(m) = (N_o^2/M^3)(3E_o/2j_*\pi)A(\lambda_v),$$ \hfill (5.1)
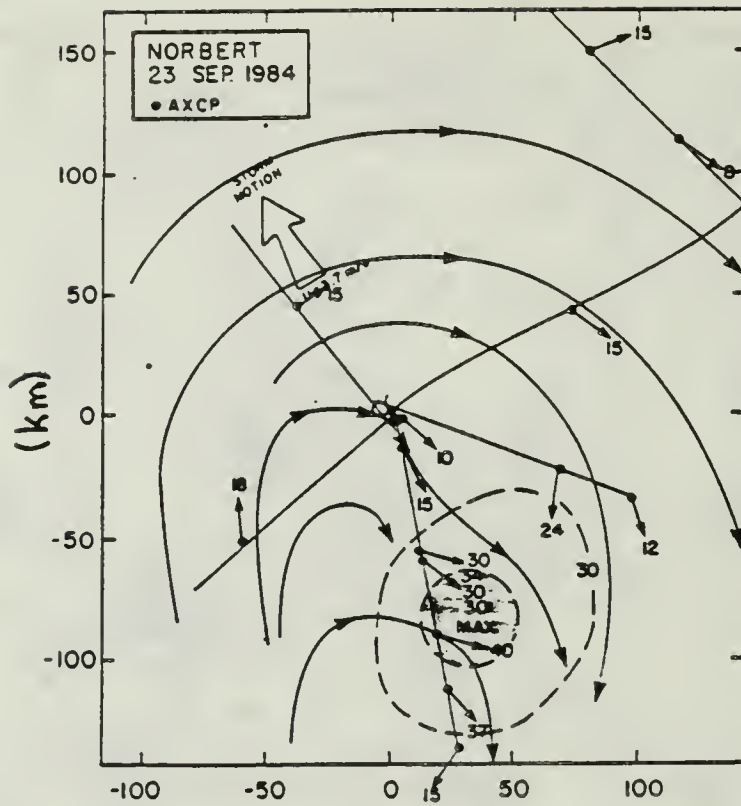
Figure 5.3 Currents (cm/s) at 80 m in hurricane Norbert with the shaded area depicting the region of maximum currents (> 40 cm/s).

where $A(\lambda_v) = (t\text{-}1)(1+\lambda_v)^{-t}$, $\lambda_v = m/(j_*\pi M_o)$, $M_o = 0.122$ cycles/km, $j_* = 6$, $E_o = 2\pi \times 10^{-5}$ and and $t = 2.5$ (Garrett and Munk, 1975). The nondimensional energy density (E_o) seems to be a universal value within a factor of 2-3 in the ocean for the background internal wave spectra (Munk, 1981).

In the right-front quadrant of hurricane Norbert (AXCP 02 in Fig. 2.6), the observed vertical wavenumber spectra are not significantly different from the GM75 spectra in the wave band from 50 m to 350 m (Fig. 5.4). At the large and small wavenumbers, there are only small differences between the observed and GM75 spectra. However, the observed KE spectra in the left-rear quadrant (AXCP 20), exceeds the GM75 values by nearly an order of magnitude over the entire spectrum. The most energetic vertical wavenumbers are associated with vertical wavelengths greater than 50 m. At the large vertical wavelengths (> 500 m), the KE values are more than an decade greater in the wake than in front of the storm because of the increased internal wave activity induced by the moving hurricane (Geisler, 1970).

The energy spectra are decomposed into clockwise (CW) and counter-clockwise (CCW) rotating components (Mooers, 1973). In the front of hurricane Norbert (AXCP 02), the CW- and CCW-rotating components are equal in magnitude (Fig. 5.5a). In the wake of Norbert (Fig. 5.5b), the CW-rotating energy exceeds the
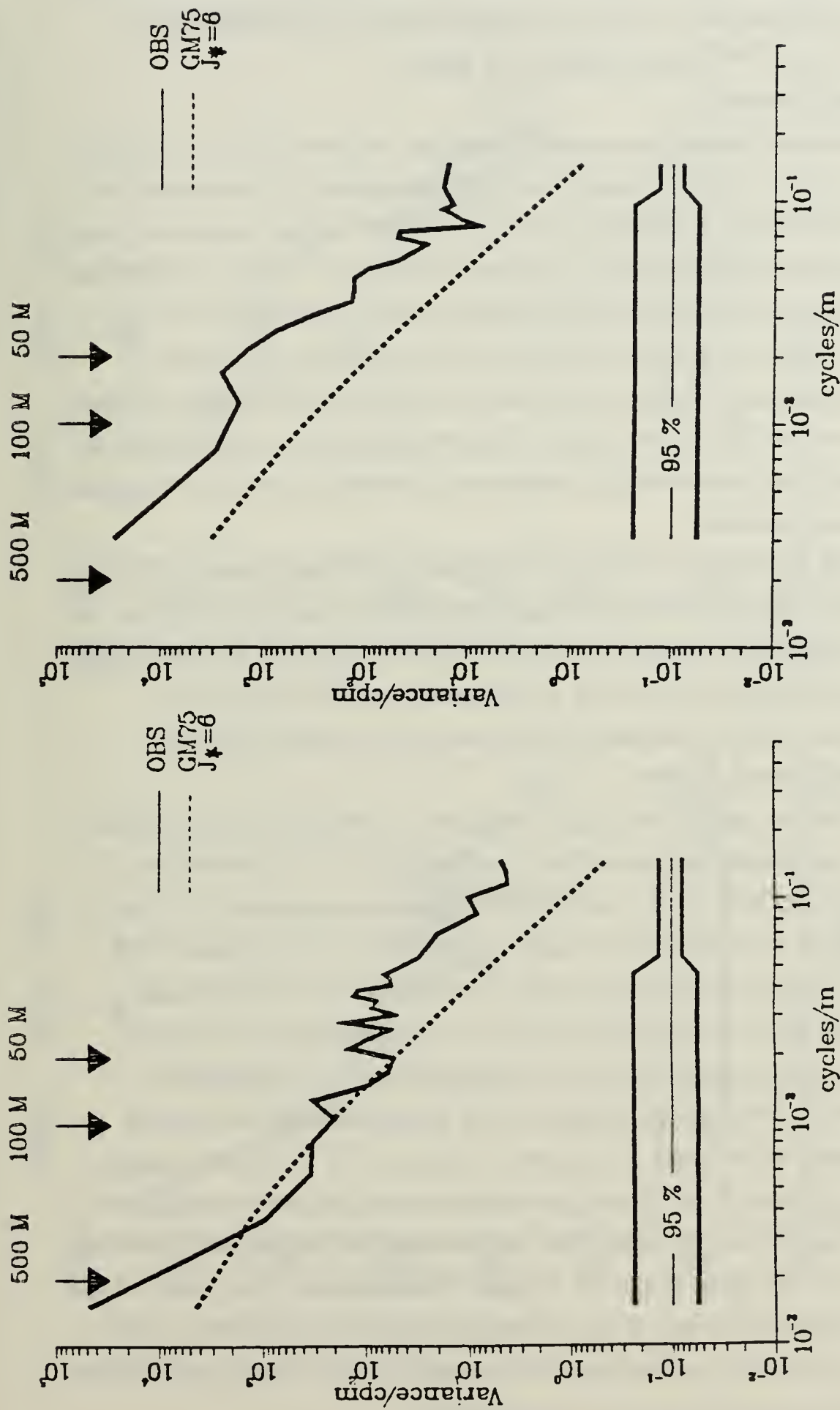
Figure 5.4 WKBJ-stretched vertical wavenumber (cpm) spectra of KE $(cm/s)^2/cpm$ (solid) in front of hurricane Norbert AXCP 02 (left) and in the wake of hurricane Norbert AXCP 20 (right). The Garrett and Munk (1975) spectrum is represented by the dashed line. The 95 % confidence limits are also shown.

97

CCW-rotating by an order of magnitude in the range of wavelength range of 50-200 m. At larger (> 500 m) and smaller (< 50 m) wavelengths, there is no preference of rotation as the CW and CCW rotating energies are equal.

2. Mean Current Profile

The spatial-mean currents are estimated from the Norbert AXCP's to separate the effects of the hurricane from the background current variability or pre-storm flow conditions. Prior to estimating the spatial mean, the vertical average is removed from each profile (Leaman and Sanford, 1975). Bootstrap methods are used to calculate the mean profiles of currents and Brunt-Väisälä frequency profiles in the uppper levels until less than nine profiles are available (Effrom and Gong, 1983). To estimate a deeper mean profiles, the mean profiles are calculated using arithmetic means until less than three profiles are available for averaging. This averaging process is concluded at 660 m. The uncertainities in estimating the mean are calculated by assuming a normal distribution of the mean currents.

The two-layer flow regime in the mean currents in hurricane Norbert (Fig. 5.6) is fairly consistent with the expected climatology north of the equatorial currents in the Pacific. Maximum mixed layer currents are about 16 cm/s towards the north-northeast with current reversals at about 100 m in the v-component and at 60 m for the u-component. Both mean current components approach zero as depth increases.

3. Near-Inertial Current Profiles

To isolate the near-inertial (and higher frequency) currents, the spatial-mean current profiles are subtracted from each of the profiles (Fig. 5.7). In front of the storm at $r = 2R_{max}$ (AXCP 31), the wind stress produces a u-component of 25 cm/s towards the west. There is considerable vertical structure in the v-component with vertical wavelengths of about 200 m superposed on the larger vertical wavelength features. In the center of the storm (AXCP 15), the wind is forcing a very large u-component towards the west. Since this probe descended slowly, the profile only extends to about 240 m. The vertical structure of the u-component is fairly simple compared to that associated with the v-component. Since AXCP 04 was deployed at roughly $r = 6 R_{max}$ in front of the storm, the wind stress and the ocean velocities are considerably weaker than those observed closer to the center of the Norbert. There are fairly strong currents in the upper ocean (< 100 m). The maximum upper ocean u and v components of currents are 20 and 40 cm/s directed towards the northwest. Below 200 m, the current components are nearly equal in amplitude (10-20 cm/s) with shorter vertical scale oscillations (100-200 m) in the v-component.
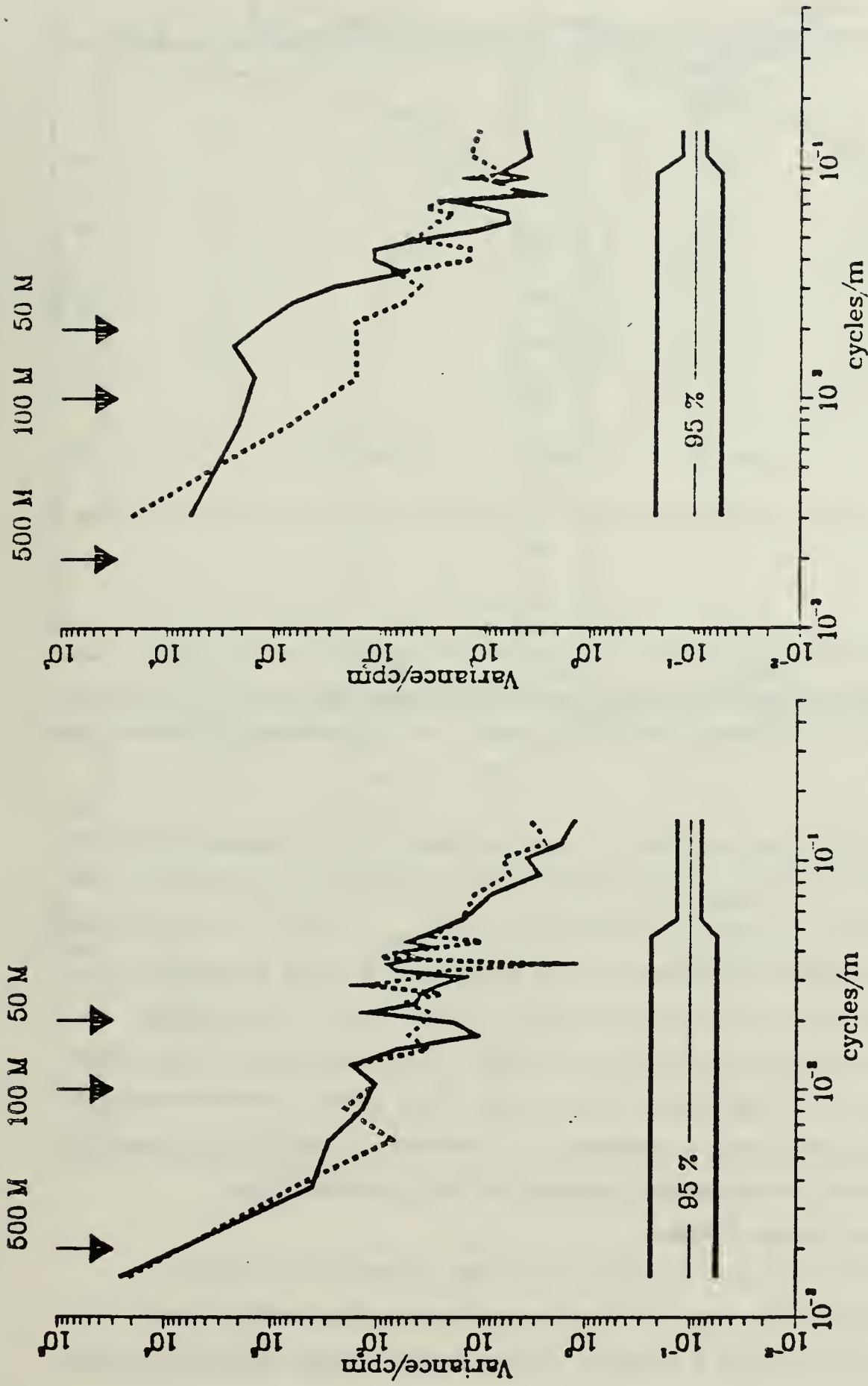
Figure 5.5 WKBJ-streched vertical wavenumber (cpm) spectra of the CW- (solid) and CCW-rotating (dashed) KE (cm²/cpm) spectra (cpm) for hurricanes Norbert AXCP 02 (left) and in the wake of hurricane Norbert at AXCP 20 (right). The 95 % confidence limits are also shown as in 5.4.
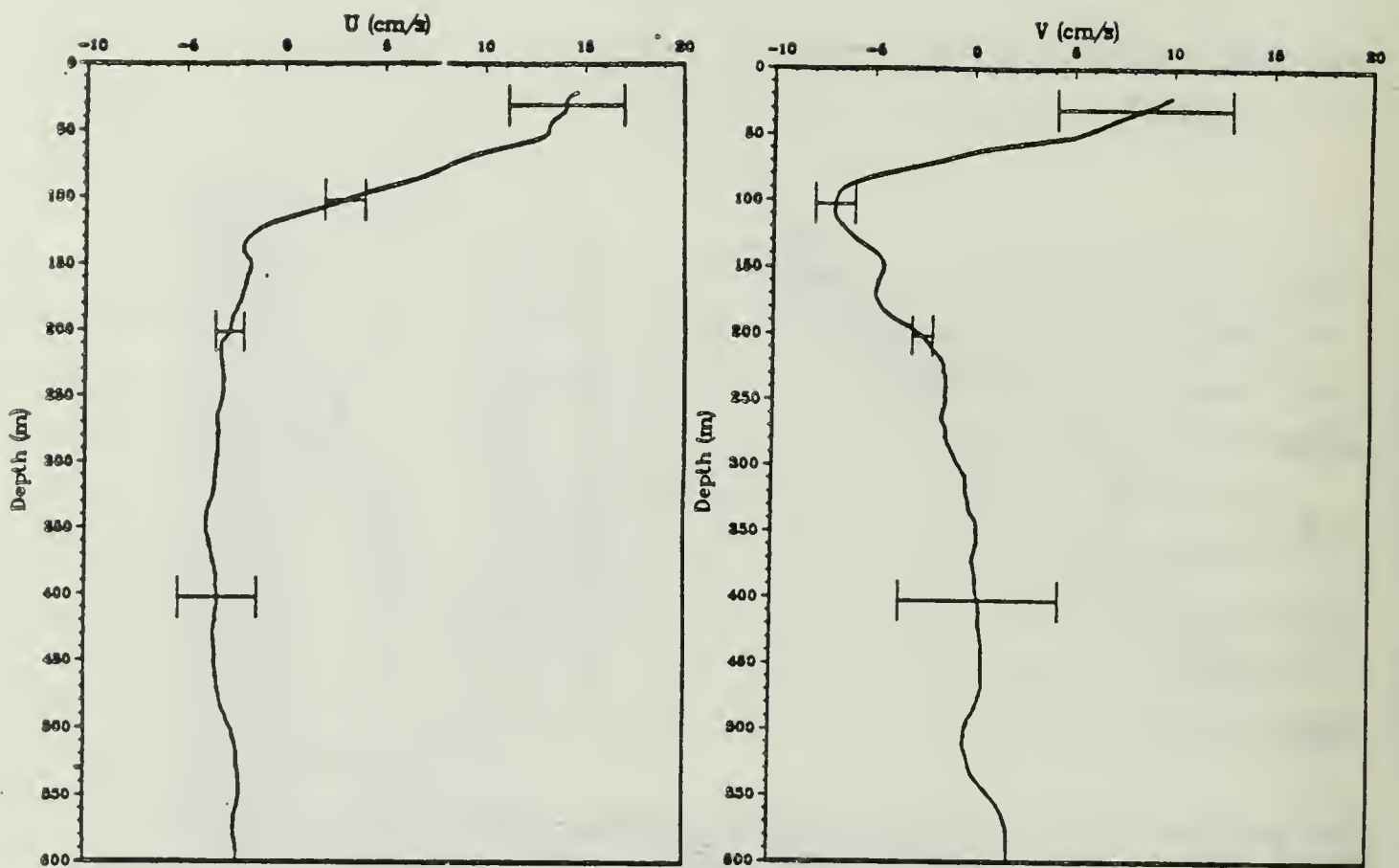
Figure 5.6 Spatially-averaged u-component and v-component (cm/s) for hurricane Norbert. The 95 % confidence limits are based on a Gaussian distribution and bootstrap methods.

One of the features predicted by numerical models is that maximum currents are in the region of $r = 2R_{max}$ to the right of the storm track (Chang and Anthes, 1978). In the right-rear quadrant of Norbert at $r = 3R_{max}$ (AXCP 14), the maximum horizontal current velocities are about 60 cm/s and suggest a simple vertical structure. In the wake of the storm in the left-rear quadrant (AXCP 20), the v-component increases to 40 cm/s towards the south in the upper ocean, whereas the u-component exceeds 75 cm/s and is flowing away from the track. This velocity pattern is indicative of divergent motion and upwelling processes. The velocities exceed 20 cm/s below 400 m, which may indicate vertical energy propagation from the mixed layer.

4. **Richardson Number Profiles**

In numerical models of the oceanic response to hurricanes, mixing is sometimes parameterized in terms of a Richardson number (Price, 1981). If the Richardson number falls below a certain critical value, momentum and heat are mixed between the two layers. Local gradient Richardson number profiles in Norbert can be calculated from the near-inertial profiles described in Fig. 5.7 and the estimated Brunt-Väisälä frequency profiles. The gradient Richardson number is given by
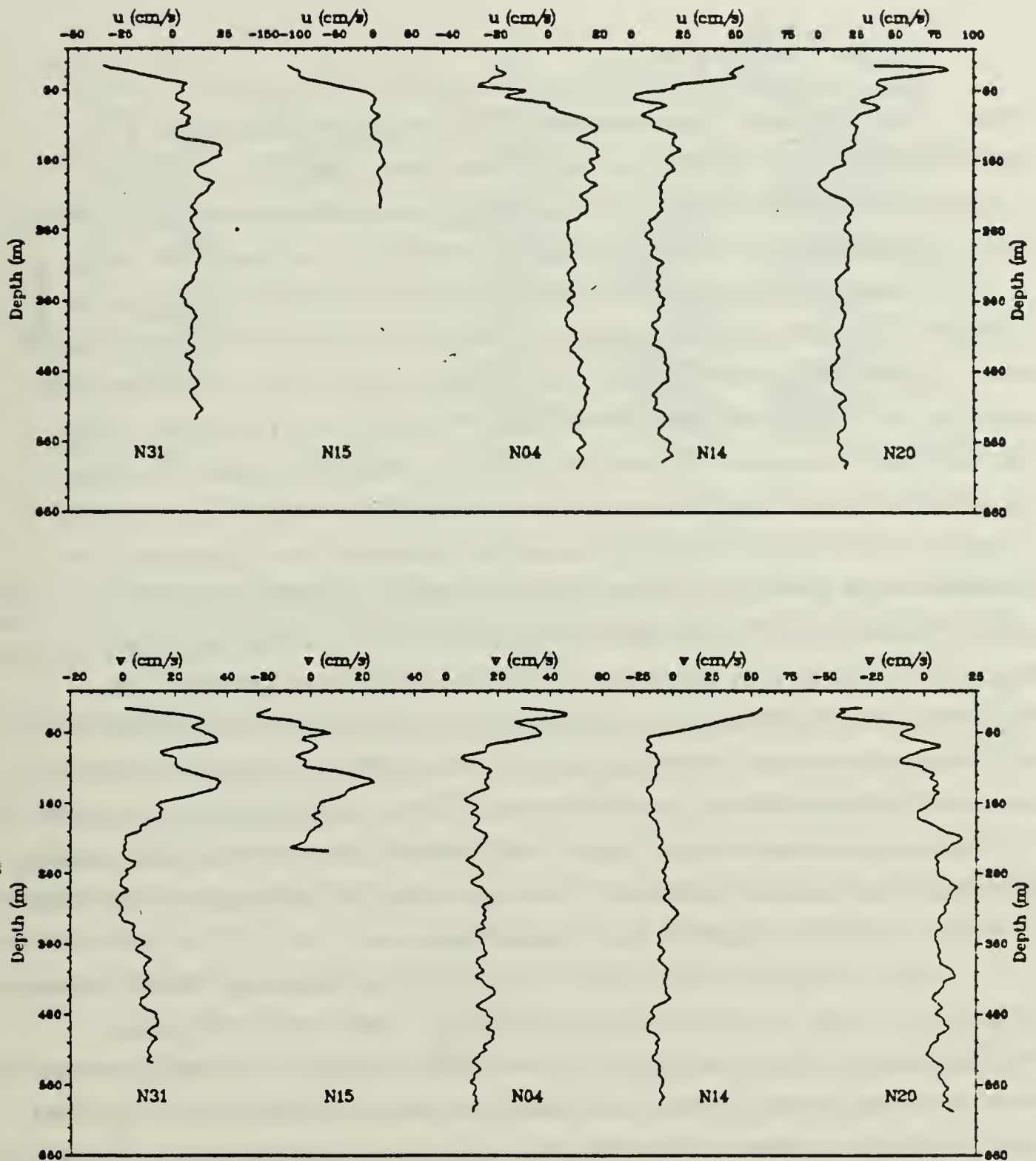
Figure 5.7 The near-inertial u-component (top) and v-component (lower) profiles (cm/s) from hurricane Norbert at selected locations as indicated in Fig. 2.6.

$$Ri(z) = \frac{N^2(z)}{u_z{}^2 + v_z{}^2} \quad , \tag{5.2}$$

where u_z and v_z represent the vertical shear of the near-inertial profiles in Fig. 5.7. Since large-scale, near-inertial waves are addressed here, a Δz of 9 m is chosen. D'Asaro (1985) argues that this interval represents a compromise between the inherent error in the measurement of velocity shear and temperature and an optimal scale.

Profiles of Richardson number (Fig. 5.8) tend to be erratic because of the possiblity of intermittent shear instabilities (Desaubies and Smith, 1982). For example, layers in which the gradient Richardson falls below a critical value of 1/4 suggests that conditions are favorable for shear instabilities. At AXCP 31 (in front of the storm), shear instability is enhanced between 100 and 200 m, which corresponds to a large change in the vertical temperature gradient from 0.12 °C/m to 0.07 °C/m. At AXCP 15 (center of the storm), the Richardson numbers fall below the critical value in the layer between 20 to 60 m and 120 m. Since the mixed layer depth at AXCP 15 is greater than 40 m (see Fig. 5.2), shear instability may be one of the mechanisms responsible for mixed layer deepening. At AXCP 04 (right-front quadrant), the Richardson number falls below the critical value intermittently between 200-300 m which suggests some small scale mixing events. The profiles of Richardson numbers are virtually identical in the upper 80-100 m at AXCP 15 and AXCP 14 . In the area of strong vertical advection (upwelling) at AXCP 20, the shear instability is apparently occurring throughout the thermocline. This region is still being strongly forced because the winds are high in a region of shallow mixed layers.

The near-inertial velocity profiles acquired during the passage Norbert indicate the presence of large vertical wavelength oscillations. Since these profiles were de᷈ᷜᷟᷝ᷍ed within the direct forcing regime or near-field, it is clear that vertical structure is not just a sum of the free baroclinic modes as in the far-field (Gill, 1984). The wind stress is a very potent source of near-inertial oscillations in the upper layers (D'Asaro, 1984). Thus, the current profiles should be expanded in terms of the applied atmospheric forcing, especially for comparisons in the near-field.

C.   MODAL ANALYSES

Gill (1984) noted that if the large scale limit (S > 1) is satisfied (see Table 4), the ocean response can be described by the first few free modes. As shown above, 55-65 % of the variance in the current meter observations in the far-field after the passage of
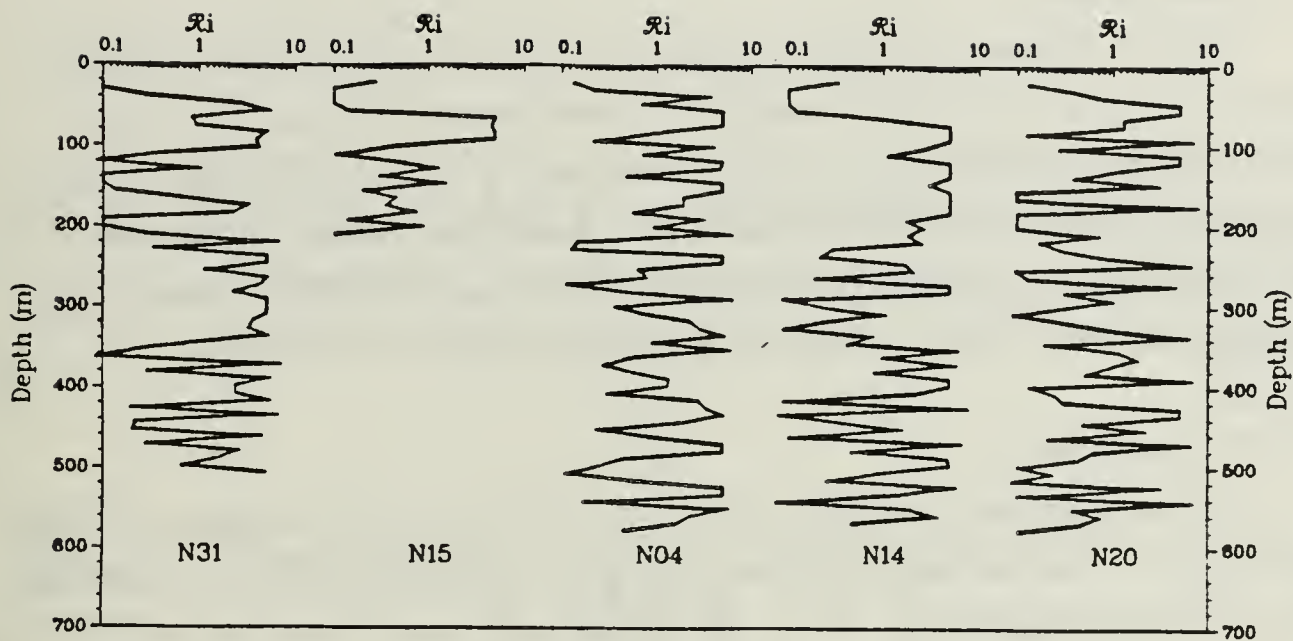
Figure 5.8 Richardson number profiles from hurricane Norbert based on the vertical shear of the profiles in Fig. 5.7 and the Brunt-Väisälä frequency profile at each location (as indicated on Fig. 2.6).

hurricane Frederic could be explained by a summation of the depth-averaged and first two baroclinic modes. However, the observations in Norbert are clearly in the near-field. Furthermore, mixed layer currents ($N(z)=0$) are set to zero when scaled according to WKBJ theory, which eliminates the most energetic current components. Thus, the near-inertial current velocities from the AXCP's should be compared to the forced baroclinic modes. The residual current (u_r) at each depth that cannot be explained by the forced model is given by:

$$u_r(x',y',z) = u_o(x',y',z) - \sum_n u_n(x',y')\varphi_{nz}(z) \quad , \tag{5.3}$$

where u_o is the observed u-component rotated 40 ° clockwise into storm coordinates (x',y') and u_n is the horizontal structure coefficient as a function of mode number n. The residual v-component has a similar expression. The vertical average is removed from the observations prior to the fitting procedures.

For each mode. the horizontal structure functions of velocity have three terms in (3.13) : the wind stress curl. divergence and Ekman-type terms. In the superposition process, the wind stress is divided by these equivalent forcing depths. Since the equivalent depths ($\int_{-D}^{0}\varphi_{nz}^{2}(z)dz$) for the first five baroclinic modes are 98, 334, 336, 421 and 592 m (see Table 6), the wind stress and the simulated horizontal velocity structure functions decrease as mode number increases.

1. Forced Modes

Any combination of the three forcing terms for each velocity can be used to construct a model profile at (x',y') using (3.9). Since the model is linear, the same terms for each mode must be used in the summation over n modes. Selected velocity profiles in the wake are compared in Fig. 5.9 to the analytical model profiles using three or four modes. These horizontal structure functions are based on physical processes calculated in (3.19), rather than as a least-square fit of orthogonal polynomials.

2. Vertical Profiles

On the right side of the track (AXCP 13 , see Fig. 2.6 for locations), all three forcing terms are used for both velocity components in a summation that included the first four baroclinic modes (Fig. 5.9a). The model profile can account for over 70 % of the observed variance using the first four near-inertial modes! In the near-surface layer (20-40 m), the observed velocities exceed the model velocities by only 15 cm/s. In the 50-70 m layer, there is a difference of 15-18 cm/s between the observed and model v-component, which suggests that higher order near-inertial baroclinic modes may be present, or that all of the surface wave energy has not been removed. The enhanced vertical shear between 80-100 m is associated with near-inertial processes. Within 10% uncertainity limits of the model storm parameters, the residuals in the upper layers are reduced below 15 cm/s. The depth-average residual current is 4 and 3 cm/s for the u and the v-components, which is indicative of a reasonably good fit. On the right side at AXCP 14 (Fig. 5.9b), a four baroclinic mode model also agrees a little better with the observed velocities in the enhanced vertical shear layer (50-70 m).

On the left side of the track at $r = 2R_{max}$ (AXCP 18), there is considerable agreement between a three mode model and the observed profiles (Fig. 5.9c). The v-component driven by the wind stress curl changes direction between the upwelling and downwelling peaks in the wake. The model u-component in the upper 100 m underestimates the observed profile by 18-20 cm/s although the depth-averaged residual is about 5-6 cm/s. Compared to the right side, the agreement between the observed and simulated profiles at this site is poor. Since hurricane Norbert changed both speed and direction (curving towards the west) in the vicinity of the AXCP deployments (Fig. 2.6), the oceanic response on the left side of the storm will be considerably more complex than on the right side.
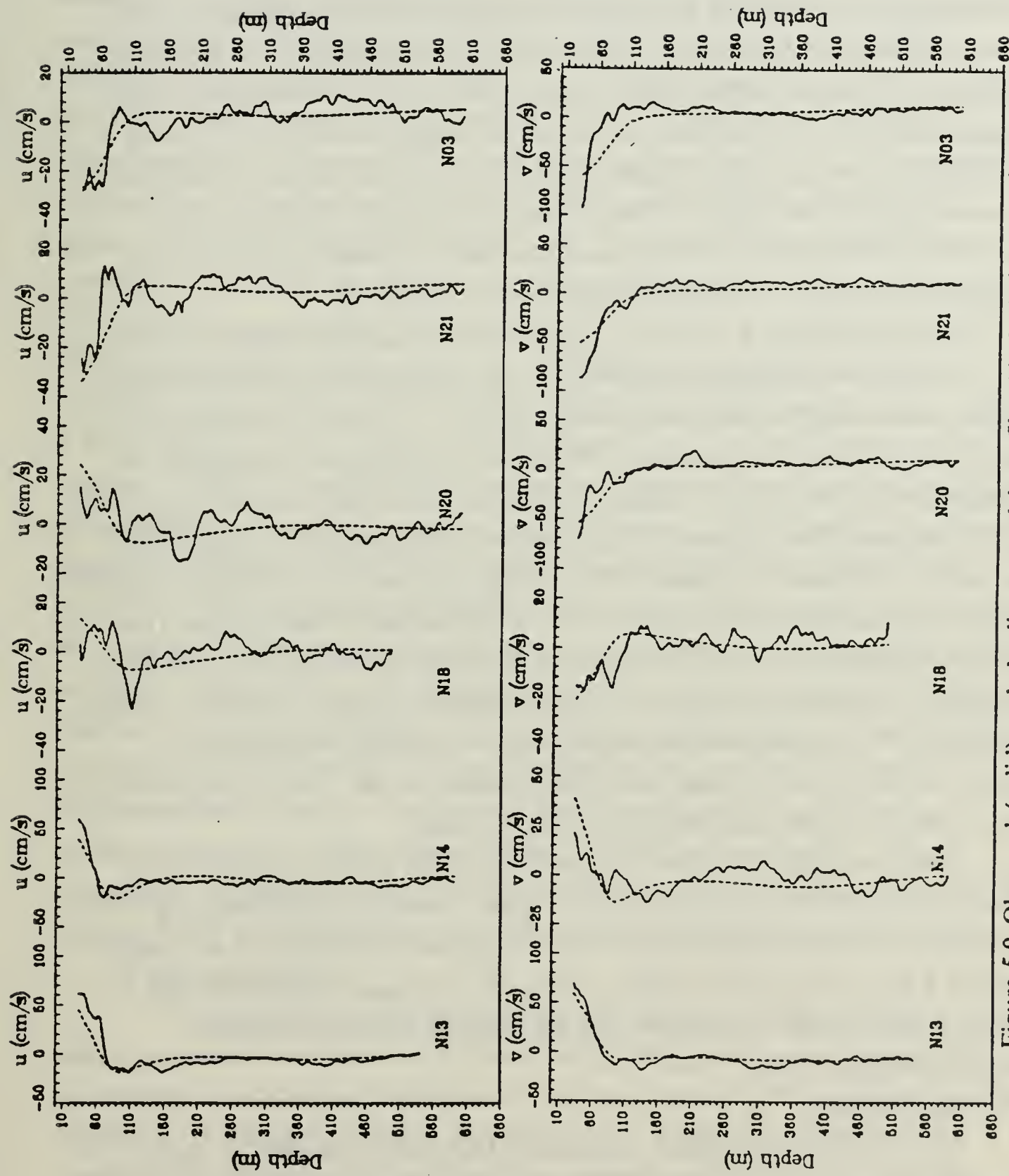
Figure 5.9 Observed (solid) and the linear model profiles (dashed) in cm/s for the u-component (upper) and the v-component (lower) for selected AXCP's deployed in the wake of hurricane Norbert. The model profiles are based on a summation of three or four baroclinic modes as discussed in the text.

In the left rear-quadrant at $r = 3R_{max}$(AXCP 20), the model profile with three modes overestimates the observed u-component in the mixed layer by 5-10 cm/s and underestimates the v-component by about 20 cm/s (Fig. 5.9d). Below the mixed layer, the residual velocities are within 5-10 cm/s and are represented reasonably well with the near-inertial model. However, there is a large discrepancy at 180 m between the model and observed profiles. Adding more vertical modes to the summation does not significantly reduce the residual profiles. In this region (see Figs. 5.1-5.3), there is a minimum in mixed layer temperatures and depth (18-24 m) as upwelled water from the thermocline is entrained into the mixed layer. The vertical velocity of the first mode (see Fig. 3.3) is positive, which is associated with an upwelling regime and the divergence in the upper ocean (relative maxima of u-component).

On the left side at $r = 3\text{-}4\ R_{max}$ (AXCP 21), considerable vertical structure exists in the observed u-component between 80 and 120 m that is not well resolved by the linear model using four baroclinic modes (Fig. 5.9e). The model u-component is within 8-10 cm/s of the observed profile. However, the mixed layer v-component is underestimated by over 30 cm/s. Slightly farther back in the wake ($r = 5\text{-}6\ R_{max}$), the model v-components are comparable to the observed v-component in the mixed layer (not shown). One possible explanation for the large discrepancy in this region could be associated with the wind shifts associated with the curved path of the hurricane (see Fig. 2.6), which should affect the profiles more on the left side than on the right side. Nevertheless, the averaged residuals are 4-5 cm/s for both profiles. The shorter vertical wavelengths (200 m) in the observed profiles cannot be resolved with only four baroclinic modes. However, these smaller scale features are not nearly as important in terms of energetics as the large vertical wavelength modes.

A three mode model follows the observed velocity profile on the left side of the storm at AXCP 03, except for the 200 m vertical wavelength oscillations (Fig. 5.9f). The residual u-component is less than 10 cm/s throughout the profile with an average residual of 4 cm/s using the three modes. Again, the very large v-component near the surface is underestimated by about 40 cm/s and there are fairly large residuals throughout the upper 100 m.

3. Kinetic Energy

The observed kinetic energy at selected AXCP sites is compared in Table 14 to the simulated energies for the model with three or four modes as discussed above. The most striking feature is that mode 1 contributes more to explaining the observed energy

than any other mode. On the right side of the storm, the model energy explains between 67-78 % of the observed energy at AXCP's 13 and 14 when the first four baroclinic modes and all of the forcing terms are used in the model. Thus, the stress divergence and Ekman-type terms contribute to the ocean current variability, but they are dominated by the wind stress curl terms in (3.19). A least-squares fit of the observed velocity profiles at AXCP 13 and 14 to the first three modes accounts for 80 and 55 % of the observed KE. On the left side of the storm, there is considerable spatial variability in observed KE, and the model accounts for 34-75 % of this energy. The minimum in the observed KE at AXCP 18 suggests that it was deployed in a region in which the v-component changes sign. The analytical model profiles with three baroclinic modes only explains 34 % of the observed kinetic energy as compared to 20 % in a least-squares fit. A least-squares fit of the first ten modes only explains 55 % of the observed kinetic energy. At AXCP 20 and 21, the analytical model explains over 60 % of the observed kinetic energy using three baroclinic modes. Thus, it is clear that the oceanic response changes dramatically over relatively short spatial distances (1-2 R_{max}). At AXCP 03, the model kinetic energy only explains half of the observed energy using either a three or four mode model. At this location, the least-squares fit explains about 65 % of the energy because the mode 1 coefficients are about 10-12 cm/s more than the simulations from the analytical model. Some of the discrepancies between the observed and analytical profiles are due to inherent spatial variability of the hurricane. For example, Norbert was changing both speed and direction just south of the vicinity where the AXCP's were deployed. For a hurricane curving towards the west (Fig. 2.6), the oceanic response on the left side will be considerably more complex. Furthermore, the actual wind stress fields were not available mainly due to limited observations in the left-front quadrants. A more quantitative comparison between the observed and model profiles may require that the Rankine vortex be replaced with the actual spatial distribution of the wind stress.

4. Model Sensitivity

To assess the impact of uncertainties in the observed storm parameters on the model simulations, the model forcing functions (τ_m, R_{max}, U_h, and inflow angles) are changed by ± 10 % for the first three baroclinic modes (Table 15). A composite of the changes in the simulated velocities for a 10% change in the storm parameters is combined for each baroclinic mode and then summed over the first three baroclinic modes. These changes in model parameters are combined into a composite value for

Probe	$\sum KE_1$	$\sum KE_{1\text{-}2}$	$\sum KE_{1\text{-}3}$	$\sum KE_{1\text{-}4}$
N13	72	80	82	78
N14	52	55	60	67
N18	22	30	34	--
N20	50	57	61	58
N21	63	72	75	76
N03	17	30	47	52

each mode. As expected, the differences in the simulated velocities are largest closest to the storm (3-7 cm/s) and are dominated by mode 1. Surprisingly, the uncertainties in the velocity for mode 3 exceed that in mode 2. Since the wavelength of mode 3 in the unforced case is about 78 km (compared to 130 km for the second baroclinic mode), the mode 3 wavelength is closer to the scale of the wind stress curl, which may account for the increased excitation of the modal amplitude.

TABLE 15

Change in the horizontal structure functions (cm/s)
for the first three baroclinic modes based a 10 % uncertainty in storm
parameters.

Probe	u_1	u_2	u_3	$\sum u_n$	v_1	v_2	v_3	$\sum v_n$
N13	2	2	3	7	1	1	1	3
N14	1	1	3	5	2	2	1	5
N18	1	1	3	7	3	1	1	1
N20	2	1	2	5	1	1	1	3
N21	2	1	1	4	0	1	4	5
N03	2	1	0	3	4	1	0	5

D. SUMMARY

The near-inertial response is isolated from the current profiles by subtracting the spatially-averaged mean currents. The frequency of the waves was determined using a mixed layer Burger number as in hurricane Frederic. The frequency of the near-inertial waves ($\sigma = 1.18f$) is within the internal wave band of $0.9f$-$1.2f$ (Mooers, 1975; Kunze, 1985).

On the right side of the storm track, the forced, linear model explains over 70% of the observed oceanic current variability using thé first four baroclinic near-inertial modes. The enhanced vertical shear between 50 -100 m appears to be associated with near-inertial wave processes. Some of the large differences between the observed and model velocities are due to uncertainities in the wind stress forcing that is used to represent the hurricane. Since the hurricane is modelled using a Rankine vortex, all the complexities and spatial variations in the wind stress are not reproduced. All of the terms (wind stress curl, stress divergence and Ekman-type) are used to explain the currents measured by the AXCP's 13 and 14.

On the left side of the storm track, the observed profiles are generally best fit with a model based on only three baroclinic modes. The mixed layer v-components on the left side are underestimated by 15-30 cm/s, whereas the u-components are within 10 cm/s of the observed. Since the path of hurricane Norbert curves to the left in the vicinity of the AXCP deployments, the ocean response of the left side is considerably more complicated than assumed in the model physics. The observed current profiles at AXCP 18 are particularly complicated because this position is in a strong upwelling and mixing regime. In a qualitative sense, the simulated v-component agrees with the observed profile. The residuals at both AXCP 18 and 20 are 4-6 cm/s and the enhanced shear layer is modelled fairly well at AXCP 20. Farther away from the storm ($r = 3$-$4R_{max}$), the model u-component nearly equals the observed velocity, even though the observed v-components are still 20-40 cm/s larger than predicted from the model. Below 100 m, the observed velocities are modelled fairly well with averaged residuals of 3-4 cm/s. Consequently, it appears more complicated dynamics are involved on the left side of Norbert, especially in the region of maximum shallowing of the mixed layer. As noted in Chapter II, the Rossby number for the Norbert storm was $O(0.5)$ which implies that the response may be moderately nonlinear. In particular, mixing and nonlinear effects that have been neglected in this simple treatment may be important near the center.

VI. NUMERICAL MODELING

Chang and Anthes (1978), Adamec *et al.* (1981), Hopkins (1982), Price (1983) and Greatbatch (1983) numerically modelled the baroclinic response to a translating hurricane by imposing a rigid lid at the sea-surface. A deep ocean was assumed in all cases except in the study by Hopkins (1982), who considered an ocean depth of 964 m. Hopkins simulated the dynamic response to a model hurricane moving at the same translation speed as Frederic. The simulated mixed layer currents agreed well with the observations. However, the computed magnitudes of the currents in the thermocline were too small. It is believed that one source of the discrepancies between the simulations and the observations is due to the neglect of the free surface and the barotropic mode, which is shown to be important in the Frederic moored current meter observations.

The primary motivation for using a numerical model here is to understand the role of the depth-averaged and baroclinic components in the ocean current response to hurricane passage. In addition, the numerical simulations provide a more complete (four-dimensional) picture of the hurricane-induced response than can only be inferred from sparse measurements. Because of the limited vertical sampling by the moored current meter arrays in Frederic, some of the higher mode energy may have been aliased into the estimates of the depth-averaged and first two baroclinic modes. The near-inertial components are isolated by demodulating the ocean current simulations and are fitted to the first few vertical modes. Many other interesting comparisons between these model simulations and the observations are left for future studies.

A. MODEL DESCRIPTION

A three-dimensional nonlinear, primitive equation model with a free surface and flat bottom has been developed by Chang (1985) to simulate the ocean's baroclinic and barotropic response to hurricane passage. The ocean is also assumed to be in hydrostatic balance, incompressible, and on an f-plane at 29 °N. The set of governing equations can be found in Chang (1985).

1. Model Grid and Storm

A staggered Arakawa-C grid (Haltiner and Williams, 1980) is used in the numerical model with a Δx of 20 km. The C grid has been shown to produce realistic

phase and group velocities in the geostrophic adjustment process (Schoenstadt, 1977). The model domain is 4000 x 1000 km with cyclic boundary conditions on the east and west sides and Neumann conditions on the north and south boundaries. A vertical grid with 17 levels is stretched for increased resolution in the upper ocean (Δz = 10 m) and a Δz = 80 m at depths below the thermocline. The total depth of the ocean is 605 m and the drag in the bottom boundary layer is treated using Rayleigh friction terms. The value of the friction is 2.3 x 10^{-6}, which corresponds to an e-folding scale of five days.

The model storm is represented by a Rankine vortex using the parameters observed in Frederic (Powell, 1982) which moves westward at 6.5 m/s. Since the inflow angle is 20 °, there can be a significant wind stress divergence (Mayer *et al.*, 1981).

2. Mode Splitting

Since the model includes a free surface, a barotropic mode will be excited by the model hurricane. Madala and Piasek (1977) treated the primitive equations in a free-surface model using a semi-emplicit formulation. By contrast, Chang (1985) introduced a mode-splitting technique by subtracting the weight of the fluid (hydrostatic approximation) from the total pressure to form a relative pressure $p_r(z)$. This term is decomposed into expressions for the mean relative and perturbation pressures:

$$p_r = \frac{1}{2}[\varepsilon]g\eta_s + g[\varepsilon z] + \rho_s g\eta_s$$

$$p_r' = p_r - [p_r] \quad , \tag{6.1}$$

where $[\ ] = 1/D\int_{-D}^{0}(\ )\ dz$ represents a vertical average, ε is the density deviation ($\rho - \rho_o$), η_s is the perturbation height of the ocean surface from a mean depth D and ρ_s is the ocean density near the surface.

The barotropic mode is treated in the momentum balance by separating the equations into a mean and perturbation quantities. The vertical mean pressure gradient excites a barotropic mode. Accordingly, the spatial gradients of the free surface height induce a "vertically-averaged" or a barotropic mode into the simulations. The perturbations of the relative pressure excite only the baroclinic part of the ocean response (Chang, 1985). Since the free-surface height enters into the pressure terms, a prognostic equation for η_s has to be derived by assuming that w=0 at z= -D and vertically integrating the conservation of mass equation

$$\frac{d\eta_s}{dt} = -D\left[\frac{\partial[u]}{\partial x} + \frac{\partial[v]}{\partial y}\right]. \tag{6.2}$$

111

The inclusion of the free surface in the ocean model requires a special time integration treatment because the speed of the barotropic mode is 100 times faster than the first baroclinic mode. To maintain numerical stability, the Courant-Frederichs-Lewy condition is

$$\frac{c_n \Delta t}{\Delta x} < \sqrt{2}, \tag{6.3}$$

where c_n is the phase speed of the waves to be resolved in the model. For a barotropic mode in 600 m of water, $c_o = 75$ m/s, whereas the phase speed of the first baroclinic mode is typically 1-3 m/s. For a grid spacing (Δx) of 20 km, the maximum time steps would be 267 and 6667 sec for the barotropic and first baroclinic modes, respectively. Hence, for every baroclinic mode time step, 25 time steps are required to integrate the barotropic mode so that the modes can interact.

The model is integrated in time using a leapfrog scheme and centered differencing in space with second order accuracy (Chang, 1984). As described above, there are two time steps: a 40 s time step for the barotropic integrations; and 1200 s for the baroclinic mode integration. A horizontal diffusion coefficient of 10^5 cm^2/s is applied to smooth the solutions. The total time integration in the following simulations is 132 h or roughly 5 IP.

3. Mixing Effects

In upper ocean response to hurricane studies, various types of mixing parameterizations have been proposed. Mixing effects were shown to be important in the oceanic thermal response to the passage of a hurricane (Elsberry *et al.*, 1976). Whereas O'Brien (1967) used K-theory (or first order closure) to close the system of equations, Elsberry *et al.* (1976) parameterized the net generation of turbulent kinetic energy in terms of the third power of the friction velocity (u_*^3) times an exponential decay factor that was proportional to the mixed layer depth. These studies revealed that advective processes dominate near the center of the storm, but mixing effects are more pronounced outside R_{max}. Chang and Anthes (1978) also parameterized mixing in terms of u_*^3. Adamec *et al.* (1981) embedded the mixed layer model of Garwood (1977) into the ocean general circulation model (OGCM) of Haney (1974). This study also demonstrated that mixing effects dominated advective effects outside R_{max}. In contrast, Price (1981) modeled the sea-surface temperature (SST) response to a moving hurricane using a parameterization in terms of velocity shear (δv) at the base of the mixed layer based on a bulk Richardson number approach (Pollard *et al.*, 1973). The

upward heat flux (ocean losing heat to the atmosphere) was only 15% of the entrainment heat flux $(\overline{w'T'})_h$ at the base of the mixed layer. Greatbatch (1984) showed that the surface sensible and latent heat fluxes were only 22% of the entrainment heat flux in a u_*^3 formulation.

In the present version of the Chang (1985) model, vertical mixing is parameterized using an eddy diffusivity K_z based on mixing length (l_m) and the local Richardson number (Ri):

$$
K_z = \begin{cases} (1-Ri)^{1/2} \left(\dfrac{\partial^2 u}{\partial z^2} + \dfrac{\partial^2 v}{\partial z^2} \right) l_m^2 & , Ri < 1 \\ 0 & , Ri > 1, \end{cases}
$$

where the gradient Richardson number is defined in (5.2). The mixing length is assumed to be the depth of the mixed layer, which thus represents a rather large eddy scale. The vertical fluxes at the top and bottom of the ocean are assumed to be zero in this model.

4. Initial Stratification

The model is initialized with a realistic salinity-temperature-depth (STD) profile acquired in the northern Gulf of Mexico at the Mobile OTEC site in the summer of 1977 (Starr and Maul, 1982). The maximum Brunt-Väisälä frequency is roughly 10 cph (Fig. 6.1) at 50 m, then decreases to roughly 2 cph over a vertical scale of 250 m and is a constant 1.5 cph below 400 m. This initial profile closely resembles the Brunt-Väisälä frequency profile estimated from climatology and the AXBT observations of Black (1983) (see Fig. 2.4b), except that the maximum Brunt-Väisälä frequency is shifted downward by 10 m.

The first five free baroclinic modes are calculated using the Brunt-Väisälä frequency profile and the Sturm-Liouville problem (Fig. 6.2). Rapid changes in the vertical structure of the φ_{nz}'s occur below the mixed layer for modes 3, 4 and 5. The corresponding phase speeds and horizontal wave lengths are quite similar to those calculated for the Brunt-Väisälä frequency profiles derived from the AXBT's (see Fig. 2.4). For example, the phase speeds are 2.9, 1.3, 0.8, 0.5 and 0.4 m/s for the first five baroclinic modes for the OTEC profile.

B. SIMULATED CURRENT AND TEMPERATURE STRUCTURE

The pattern of simulated mixed layer velocities (Fig. 6.3) is similar to that predicted from linear theory (Geisler, 1970). Upwelling and downwelling are associated with the convergent and divergent velocities. The wavelength of these cells is given by
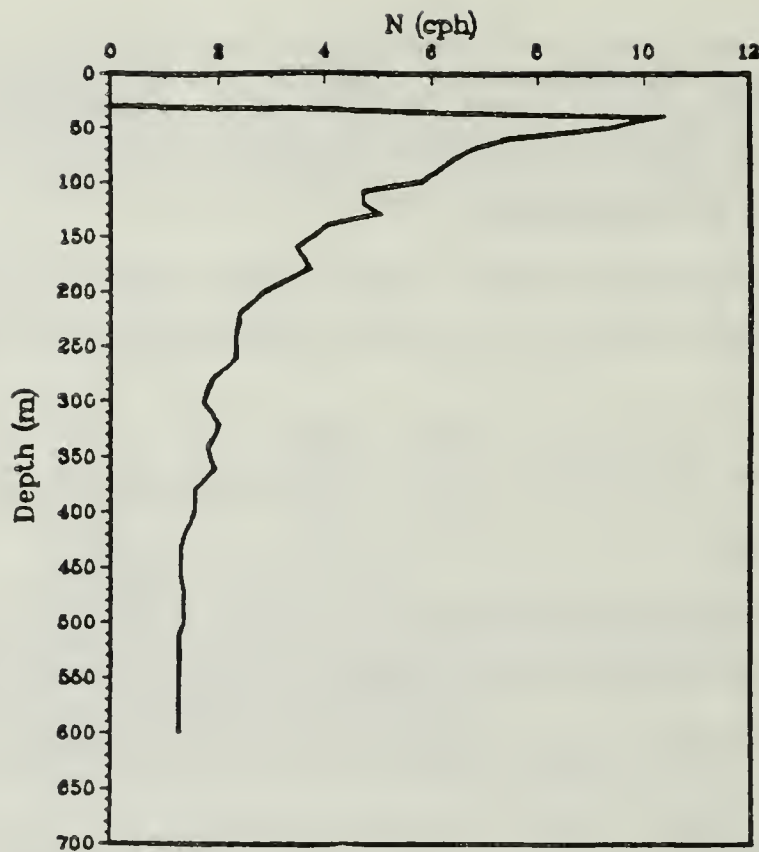
Figure 6.1 Brunt-Väisälä frequency (cph) profile from an OTEC STD station 10 at 29 °N and 88 °W.

product of the IP and U_h. The effect of the nonlinearities is to displace the velocity maximum to the right of the storm track (Chang and Anthes, 1978), since linear simulations using the same Rankine vortex have the maximum velocities along the storm track. Maximum velocities of 140 - 160 cm/s are simulated in the directly forced region. At the same distance ($r = 3-4$ R_{max}) from the storm center as Frederic data were acquired, simulated current velocities range between 100- 120 cm/s, which agrees with the observed mixed layer currents at CMA3 (see Fig. 2.4).

The pattern of velocities in the thermocline (285 m) differs considerably from the velocities in the upper ocean (Fig. 6.4). Maximum velocities are about 16 cm/s and are towards the west. However, the eastward velocities (located on the left side of the track) are elongated in the cross-track direction. These velocity perturbations are in (out) of phase with the baroclinic ridge to the right (left) of the storm track.

1. Along-Track Sections

Along-track sections of the v-component of velocity and temperature at $x = 4R_{max}$ are shown in Fig. 6.5a. The vertical coordinate (ξ) is scaled using WKBJ theory (3.7) to emphasize the processes occurring in the upper 200 m. This scaling stretches the grid spacing even more in the thermocline and shrinks it in the bottom layers. The horizontal wavelength in the simulations corresponds to the linear theory
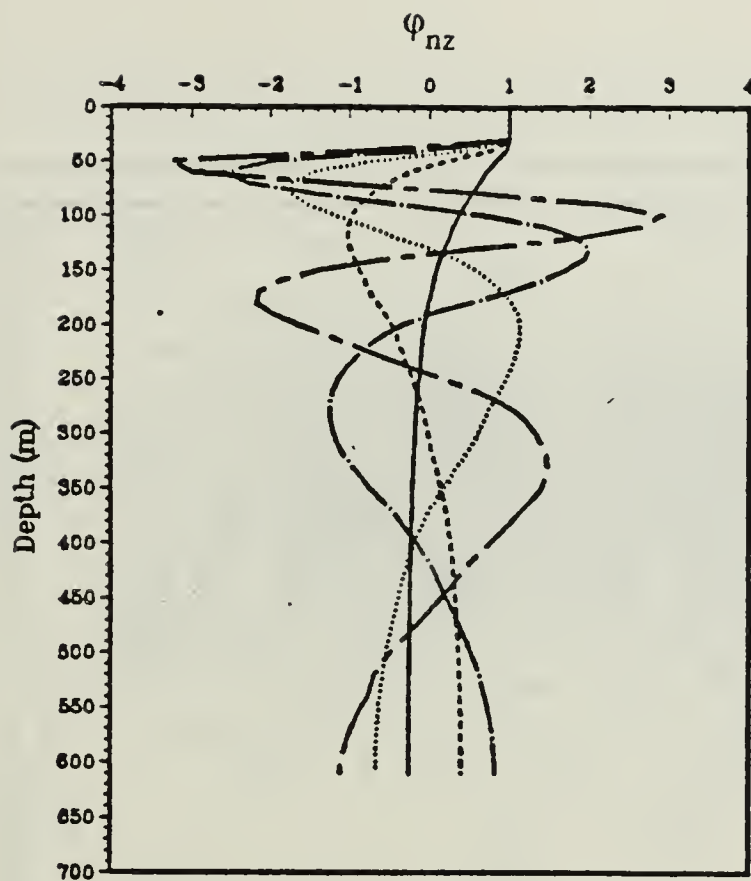
Figure 6.2 Amplitude of the horizontal velocity eigenfunctions for : mode 1 (solid), mode 2 (dashed), mode 3 (dotted), mode 4 (chain-dotted) and mode 5 (chain-dashed) based on Brunt-Väisälä frequency (Fig. 6.1).

wavelength of 580 km. Within the first IP (x = 2Λ), the ocean currents are excited throughout the water column because the free surface slope induces a depth-independent velocity component. This is the component that previous numerical modeling studies have ignored by imposing a rigid lid in the model. Notice that the slope of the phase lines is upward, which represents upward phase propagation and a downward energy propagation (Leaman and Sanford, 1976). Maximum velocites in the thermocline increase to 20-30 cm/s near 5 IP. The u-component also shows similar behavior in the phase tilt and amplitudes of the currents.

The along-section temperature changes (Fig. 6.5b) are modulated by the near-inertial cycle in the thermocline with maximum changes are about 1-1.2 °C. There is a rapid decrease in the mixed layer temperature during storm passage. The temperature increases in the thermocline are associated with downwelling processes outside of the main upwelling zone along the storm track.
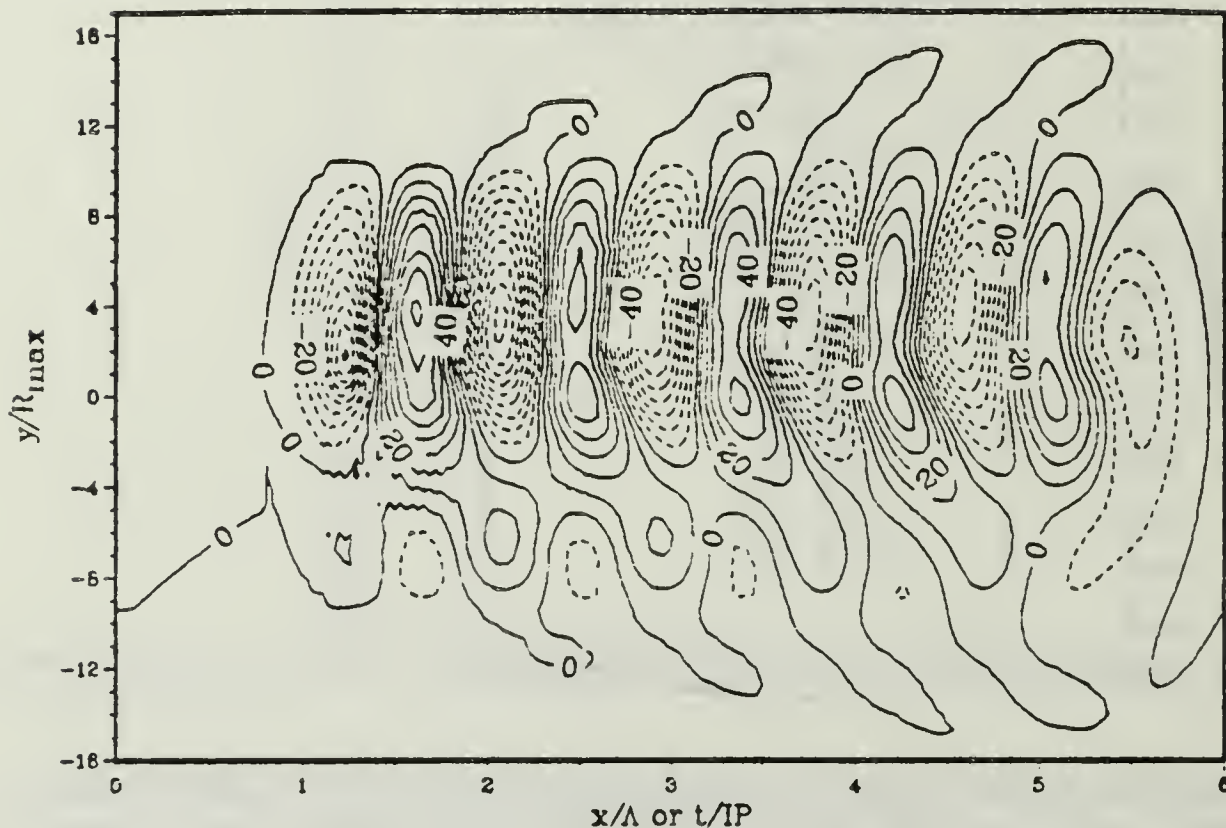
Figure 6.3 Simulated mixed layer u-component of current (cm/s) from the nonlinear model with a contour interval of 20 cm/s. The axes are scaled in terms of R_{max} (30 km) and Λ (580 km) and the storm is moving westward along $y=0$ at 6.5 m/s. The storm center is located at $x=\Lambda$.

2. Effects of the Free Surface

The deflection of the free surface simulated by the model is shown in Fig. 6.6. The maximum changes in the free-surface height are 12-14 cm and are centered along the storm track. This deformation in the free surface is caused by the mean mass divergence in the upper ocean which subsequently changes the mean vertical pressure gradient force. Thus, currents are excited throughout the water column via the pressure gradient force.

To understand the contribution of the free surface slope to the simulated ocean currents, the geostrophic velocity components are calculated from the gradient of the free surface (Fig. 6.7). On the right (left) side of the track, the maximum u-components are 12-14 cm/s in the direction of (opposite to) storm movement. These velocities are similar to those observed in the thermocline (Fig. 6.4). There also

116
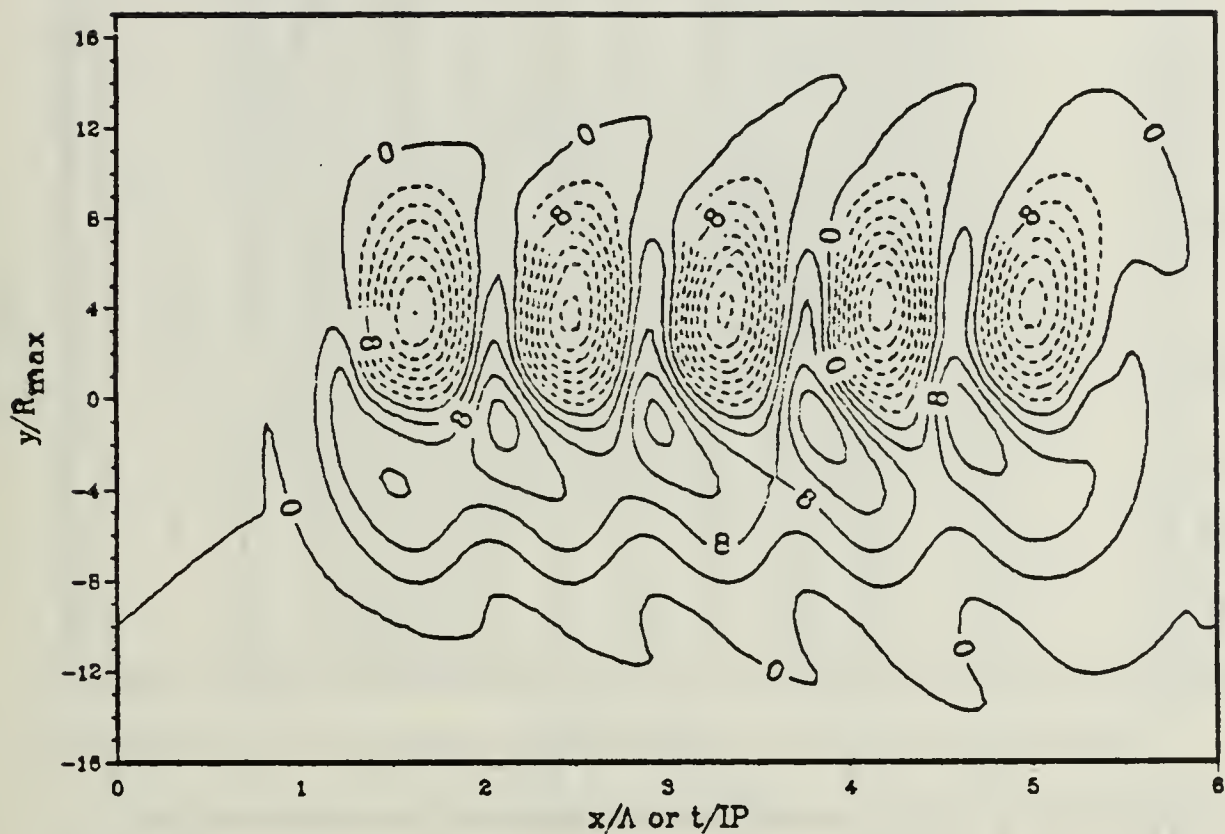
Figure 6.4 Simulated thermocline (285 m) u-component of current (cm/s) from the nonlinear model with a contour interval of 4 cm/s. The axes are scaled as in Fig. 6.3.

appears to be small cells within $y = \pm 4R_{max}$ that have a wavelength of 580 km. The maximum v-component velocities (Fig. 6.7b) are slightly weaker with amplitudes of 4-8 cm/s. However, there are also oscillations in the v-component that have near-inertial wavelengths of 580 km. Thus, near-inertial oscillations are included in the barotropic response.

In summary, these simulations have the rightward bias of the maximum current response at about $r = 2\text{-}4\ R_{max}$ with maximum mixed layer currents of · 120-140 cm/s in that region. Furthermore, the near-inertial wavelengths are about 580 km as predicted by linear theory. Thus, the simulated currents appear to have sufficient veracity to allow a comparison to the moored current meter observations.

117
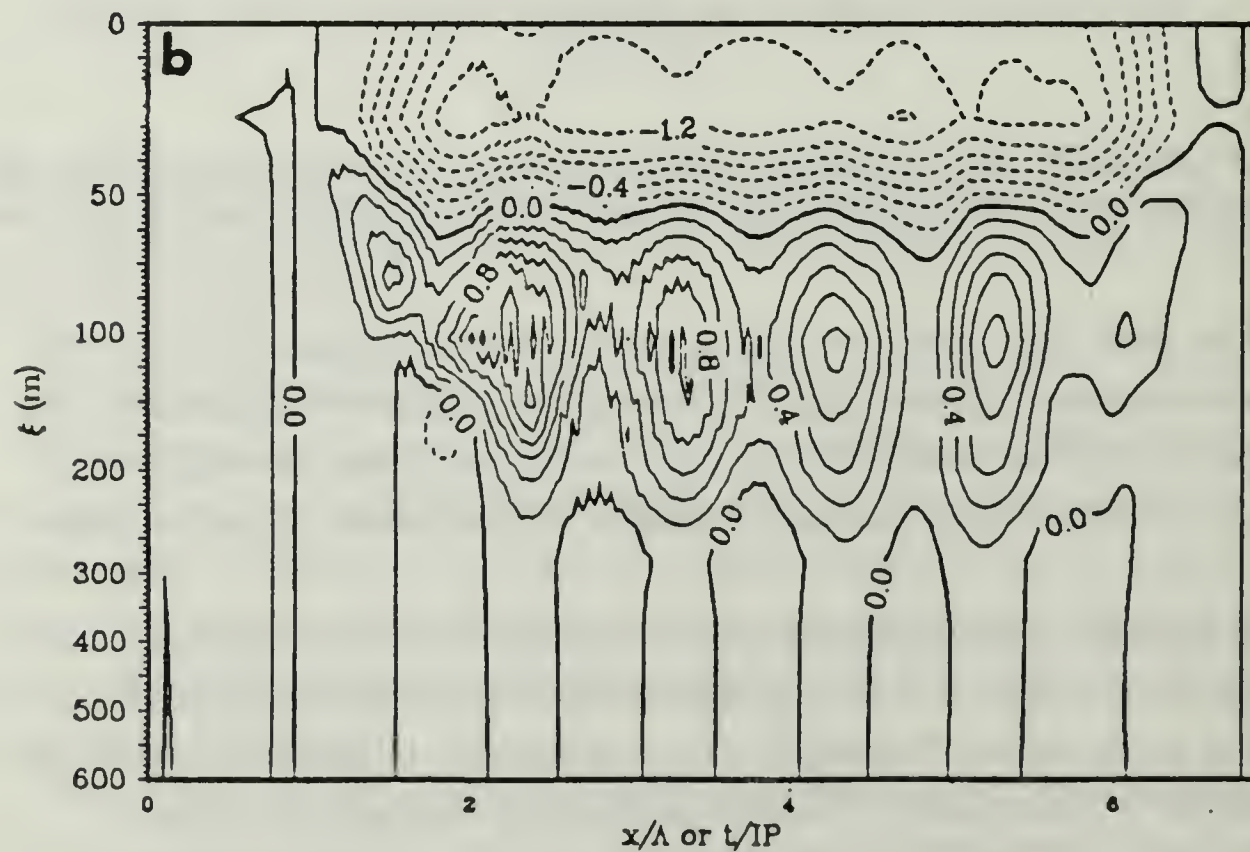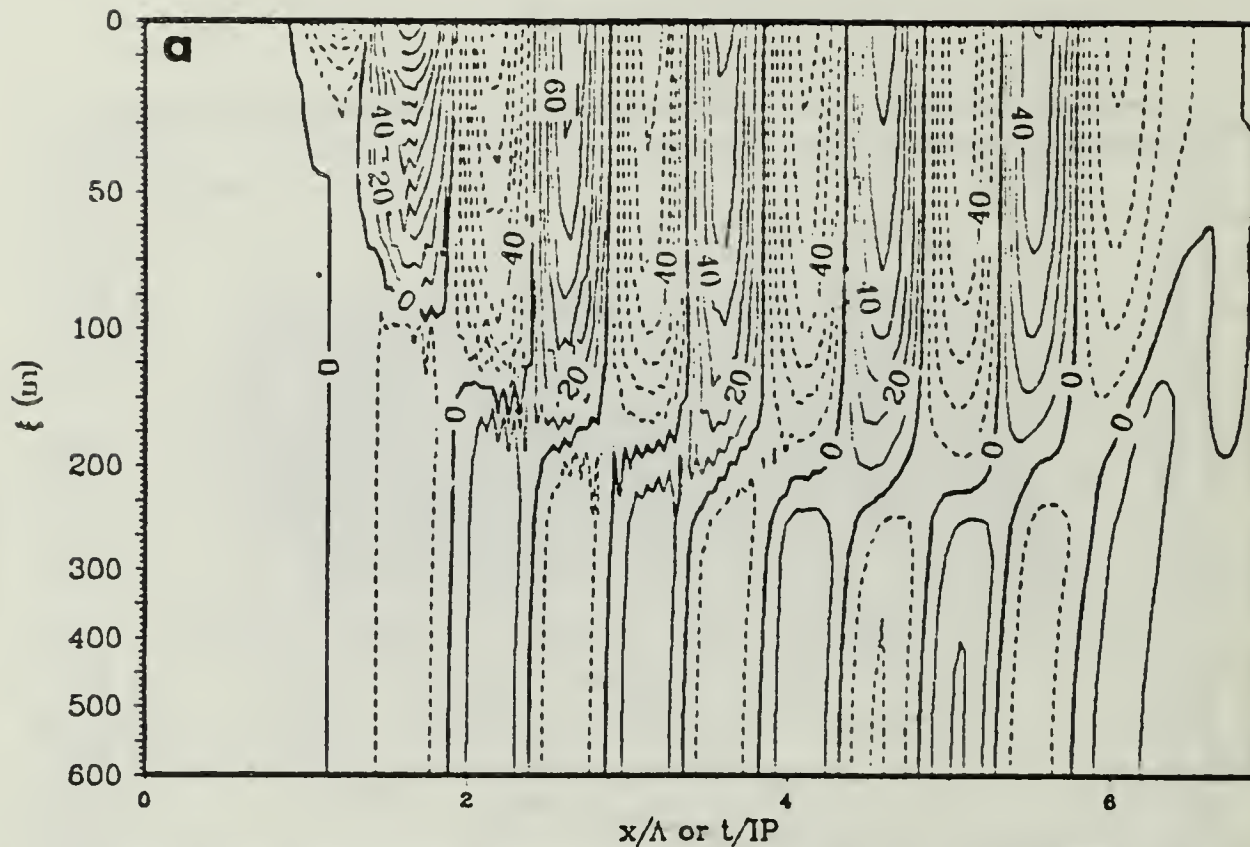
Figure 6.5 (a) Simulated v-component of current (cm/s) and (b) ΔT (°C) from the nonlinear model at $x = 4R_{max}$. The abscissa is scaled as in Fig. 6.3. and the ordinate is WKBJ-stretched using (3.7).
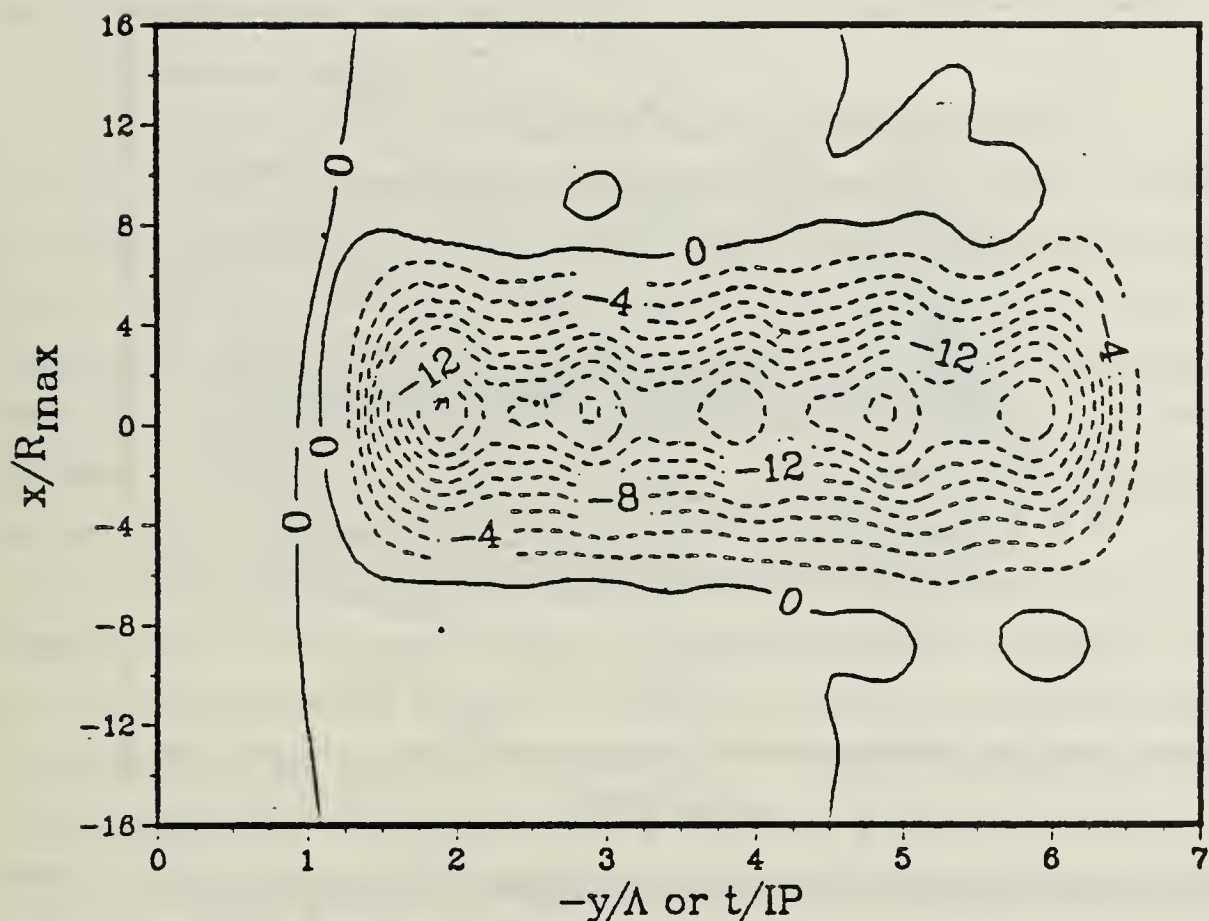
Figure 6.6 Deviations of the free surface height (cm) simulated by the model relative to the undisturbed height. The axes are scaled as in Fig. 6.3.

C.   DATA ANALYSIS

In this section, the simulated velocities are analyzed to determine the frequency of the near-inertial response. The frequencies of the waves should be blue-shifted above the local inertial frequency by the amount predicted from the mixed layer and thermocline Burger numbers (Price, 1984). In the Frederic observations, the vorticity of the mean flow could not be calculated because only two or three moorings were available. However, the mean flow vorticity can be estimated from the numerical simulations and compared to the diagnosed frequencies of the forced waves.

To simplify comparisons of the numerical simulations with the observed current meter observations in Frederic, the simulated data are rotated into a coordinate system with the storm moving towards the north. This can be done by simply rotating the simulated velocities clockwise by about 90 °. Since the model assumes an f-plane,

119
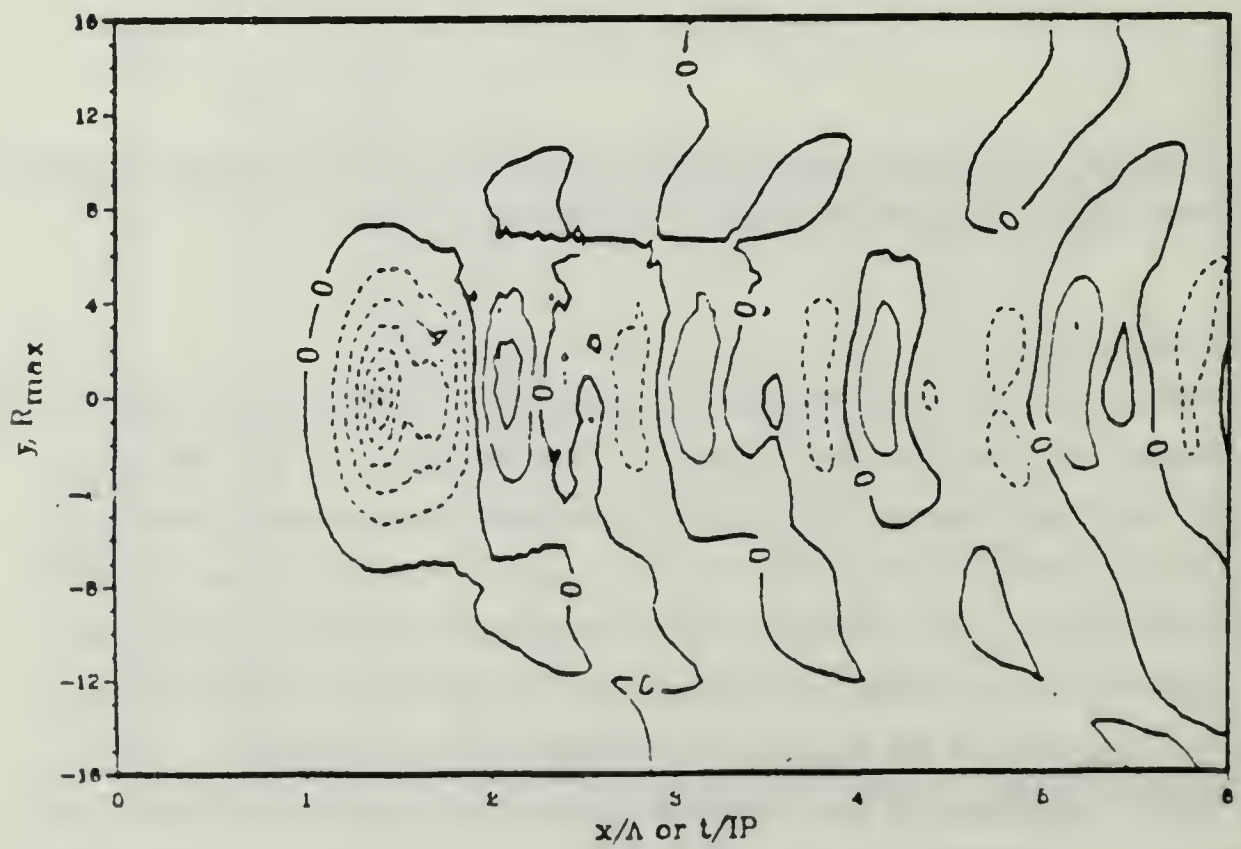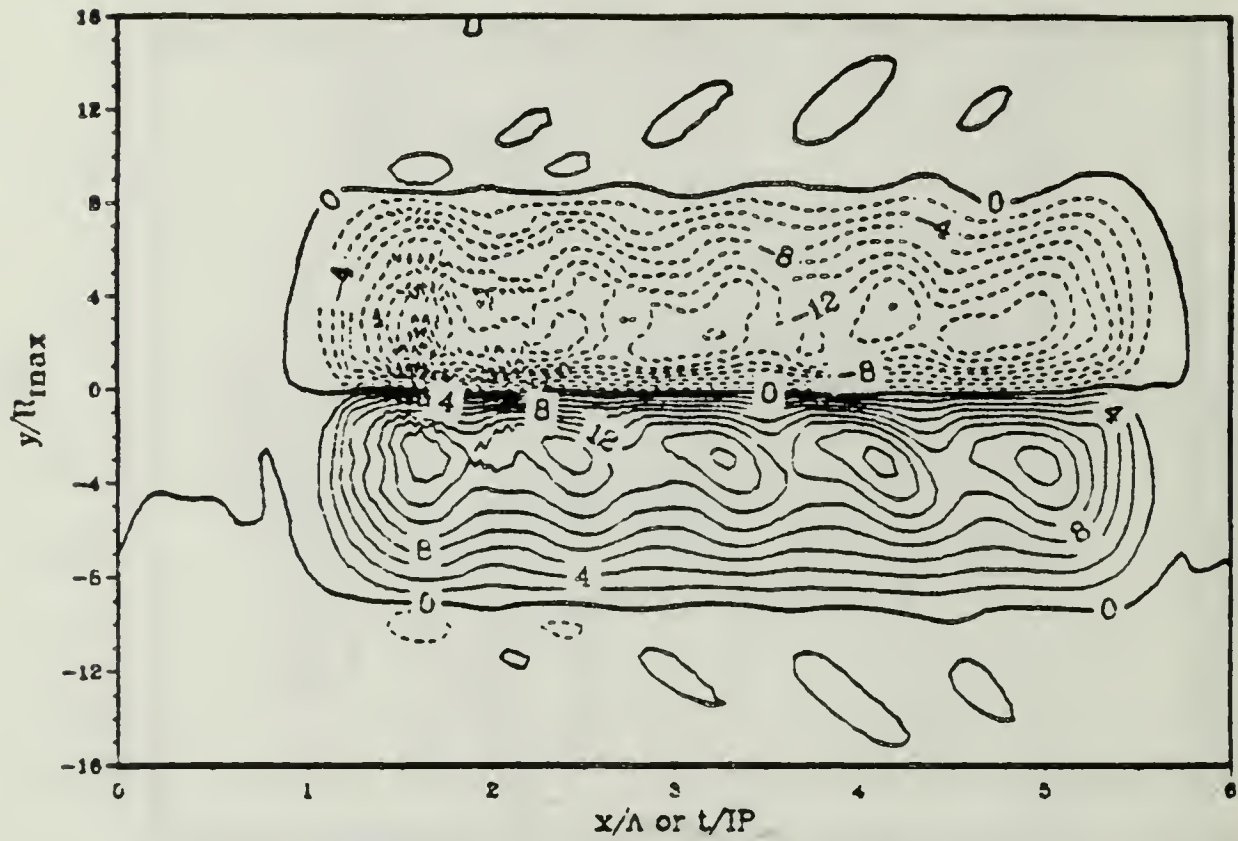
Figure 6.7 (a) The u-component (cm/s) and (b) the v-component (cm/s) of current induced by the slope of the free-surface simulated by the model. The axes are scaled as in Fig. 6.3.

beta-dispersion of inertial waves is not possible in the numerical simulation (Anderson and Gill, 1979).

1. Frequency Analysis

The horizontal velocities are first least-squares fitted with (4.1) to the model of Mayer *et al.* (1981) to diagnose the frequency of the oscillations over a 5 IP segment. The variance reduction curves from the simulated model velocities along $x = 4R_{max}$ are shown in Fig. 6.8. These variance reduction curves are very similar to those in Fig. 4.4, especially in the mixed layer. As noted in Chapter IV, the carrier frequency may not necessarily be aligned with these maxima, since it is defined to be the frequency that minimizes the covariance of the residual signals. Based on the mixed layer Burger number using the model parameters, the predicted frequency shift at 25 m is about 0.02 to 0.03f. The least-squares fit model can account for about 80% of the variance between 1.02 to 1.03 f and over 60 % of the simulated current variability in the upper part of the thermocline at 105 m. At 175 m (not shown), the maximum variances accounted for by the model are only about 45 %. Note in Fig. 6.8b that the horizontal velocity eigenfunction for the first mode is nearly zero between 135 and 175 m. At deeper levels (Fig. 6.8c and d), the least-squares model can again account for more of the variance of the simulated currents.

The diagnosed frequencies are generally blue-shifted between 1-6% above the local inertial frequency (Table 16), which is consistent with the mixed layer Burger number. This blue-shift in the frequency is evident in the upper ocean as the carrier frequency slowly changes from 1.01 f at the surface (5 m) to about 1.04 - 1.05 f at 135 m. Below the mixed layer, Price (1984) suggests that there is a blue-shift with depth that is proportional to the thermocline Burger number. Kundu and Thomson (1985) also found a consistent blue-shift with depth in the upper 200 m. The thermocline Burger number in the model is about 0.36 and the corresponding frequency shifts are proportional to T/4 or roughly 0.09f. Even with the uncertainities in the least-squares model of 0.02f, the frequency shift at 135 m is only 1.06f. Moreover, below this maximum, the diagnosed frequencies decrease slightly with depth, rather than increase as predicted from the scaling arguments. If only 3 or 4 selected levels are available as in Price (1984), a consistent blue-shift with depth might be inferred. However, it is clear the diagnosed frequencies do not show a consistent blue-shift with depth either in the simulated currents (see Table 17) or in the Frederic observations.
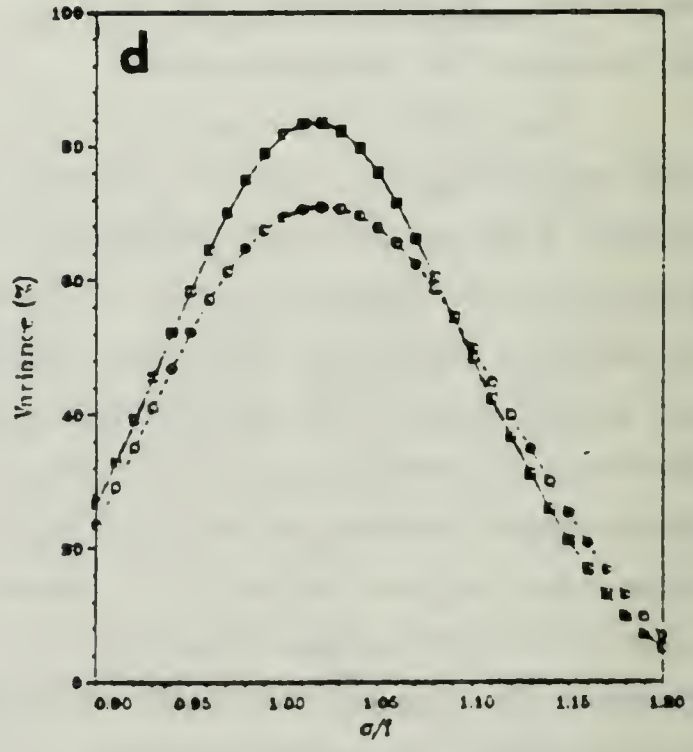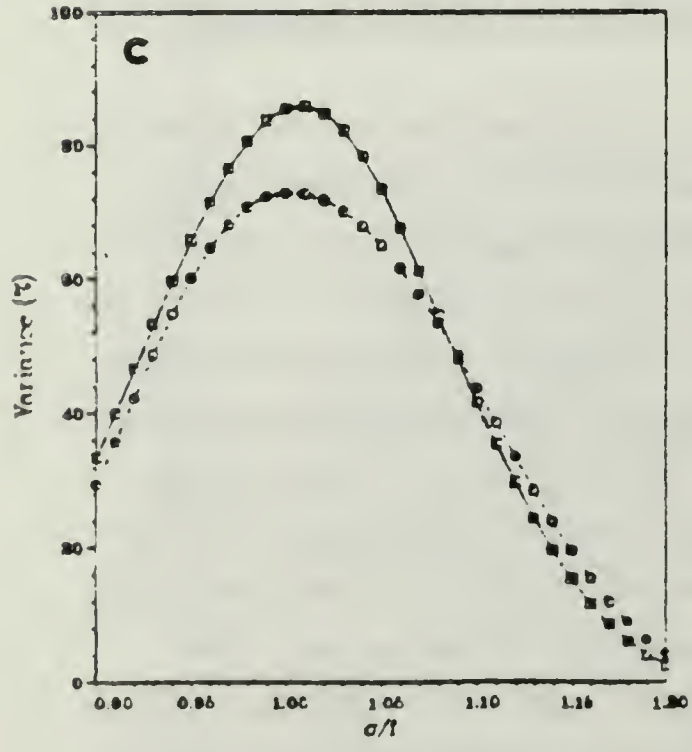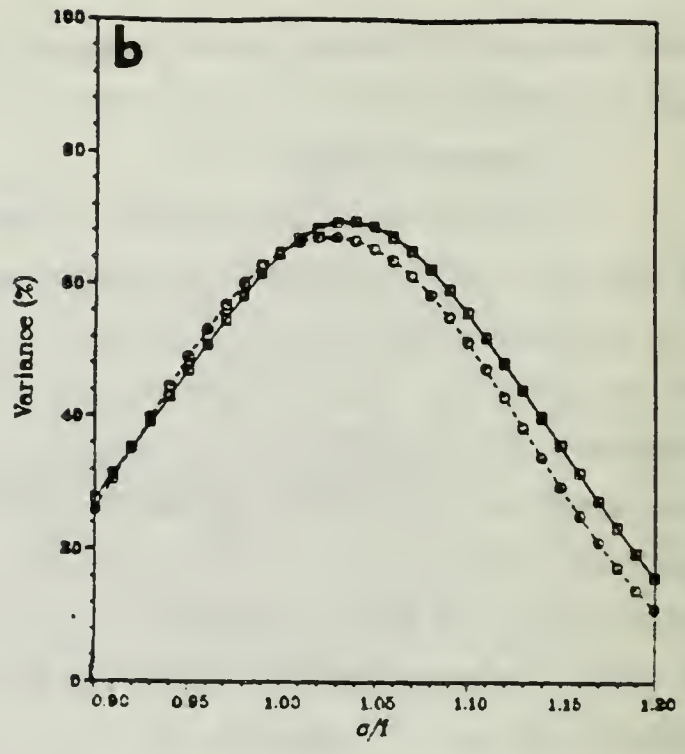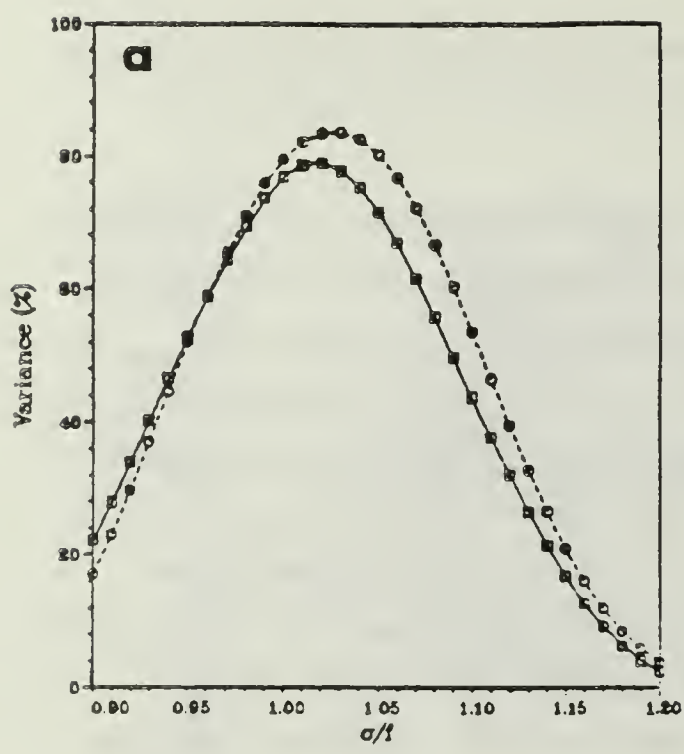
Figure 6.8 Explained variance (%) for the simulated cross-track (solid) along-track (dashed) velocity components at $x = 4R_{max}$ for trial frequencies normalized by the local inertial frequency (σ/f) at a) 25 m, b) 105 m, c) 285 m and d) 435 m.

TABLE 16

Near-inertial frequencies (periods) at which a maximum
response occurs in the simulated currents based on a least-squares fit over 5
IP.

Depth (m)	σ/f	Period (h)
5	1.01	24.5
15	1.02	24.2
25	1.02	24.2
35	1.02	24.2
45	1.02	24.2
55	1.03	23.9
70	1.03	23.9
90	1.03	23.9
105	1.04	23.7
135	1.04	23.7
175	1.02	24.2
225	1.03	23.9
285	1.03	23.9
355	1.03	23.9
435	1.04	23.7
515	1.06	23.3
595	1.06	23.3

2. Mean Flow

One possible mechanism for shifting the frequency of the near-inertial waves is the superposition of a sheared mean flow (Mooers, 1975; Kunze, 1985). If the variations of the mean flow are comparable to the wavelength of the propagating near-inertial waves, the relative vorticity of the mean flow can effectively shift the frequency of the near-inertial waves above (below) f in regions of cyclonic (anticyclonic) vorticity.

The simulated current fields are averaged using a simple running mean over an inertial wavelength (Fig. 6.9a). The cross-track scale of the mean flow in the mixed layer induced by the hurricane is about 8-10 R_{max} or about 300 km. The maximum v-component of velocity is 30-40 cm/s under the storm forcing. On the left side of the track, the v-component flows southward at about 10 cm/s whereas the flow is northerly at 10 cm/s on the right side of the track. In the mean currents at CMA3 in Frederic (see Fig. 4.3a), the v-component initially changed by 8-10 cm/s and then reversed direction towards the south within an IP to a maximum of 10-15 cm/s. In the model simulations, the magnitudes after an IP (y = -2Λ) are comparable, but are flowing in

opposite directions. By contrast, the mean u-component has a similar cross-track scale, but damps within an IP. Although some time-mean flows are evident in the deep layers, the magnitudes of the flow are only about 2-4 cm/s and the cross-track scales are about 2-4 R_{max}.

The relative vorticity (ζ) of the mean flow is calculated and normalizied by the local Coriolis parameter (2f) to form an effective Coriolis frequency shift (Kunze, 1985)

$$f_{eff} = \frac{\zeta}{2f} .$$

In the mixed layer (Fig. 6.9b), the cross-track width of the f_{eff} is only 120 km, as compared to the scale of the near-inertial oscillations of 580 km. Kunze (1985) shows that the scale of the vorticity field has to be comparable to the wavelength of the oscillations for the vorticity to shift the observed near-inertial frequency. The f_{eff} has a maximum value of about 0.02-0.03 f along the track and is cyclonically rotating which can also blue-shift the frequency of the waves. There are two small cells of anticyclonically rotating vorticity on either side of the track. However, they are transient features and damp quickly. As noted in Chapter IV, the vorticity of the mean flow could not be resolved with only the current meter arrays in Frederic.

The estimated frequency shifts from Table 17 and the f_{eff} are compared over depth in Fig. 6.10. It is clear that at x = 0, $2R_{max}$ and $4R_{max}$, the shifts in σ/f near the surface are out of phase with the f_{eff} vertical structure. In the upper levels (5-15 m), the f_{eff} is a maximum of 0.07 f, whereas the diagnosed frequencies are only 1.01-1.02 f. This estimate of f_{eff} may be somewhat misleading since the upper levels (5-15 m) are in the diffusion dominated zone in the model. As depth increases, f_{eff} decreases to nearly zero below 55 m. By contrast, the σ/f increases with depth to a maximum of 1.08 at 135-175 m along the track (x = 0). A similar increase with depth is apparent at x = $2R_{max}$. However, the maximum σ/f at $4R_{max}$ is only 1.04. The nearly uniform increase with depth of the σ/f agrees with predictions calculated from the Burger numbers (Price, 1984). The frequencies of the simulated near-inertial oscillations decrease with depth even directly along the track. Thus, the consistent blue-shift with depth may be limited to the upper ocean with vertical scales comparable to the thermocline.

D.   NEAR-INERTIAL RESPONSE

The simulated velocity data are demodulated at the carrier frequencies given in Table 17 to isolate the near-inertial response in the simulated current fields. The
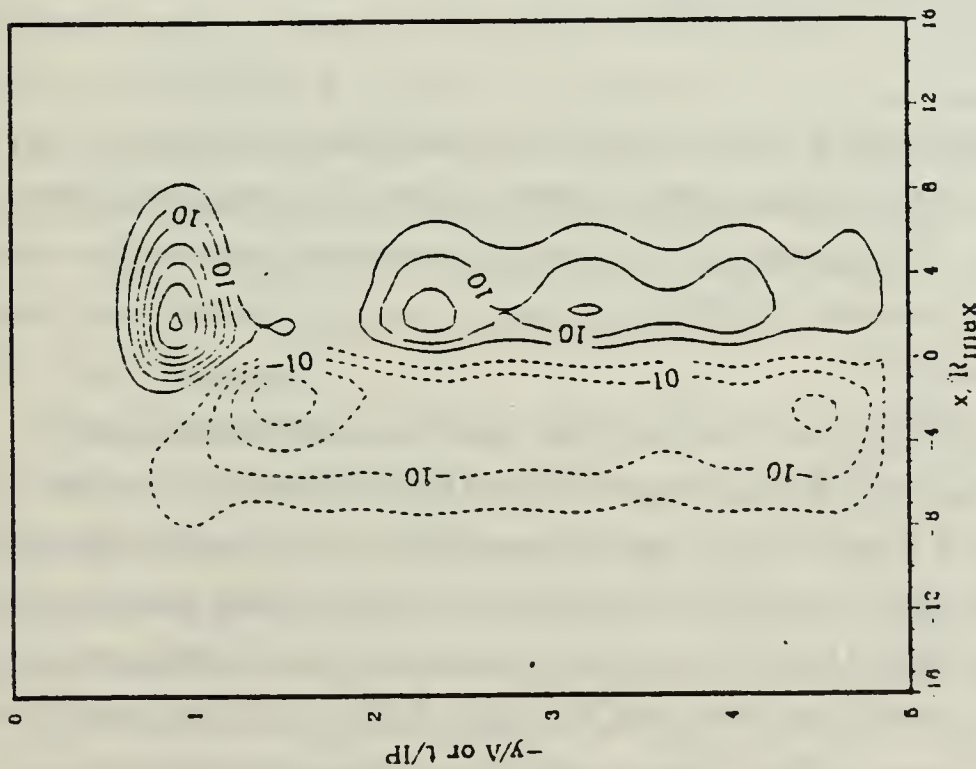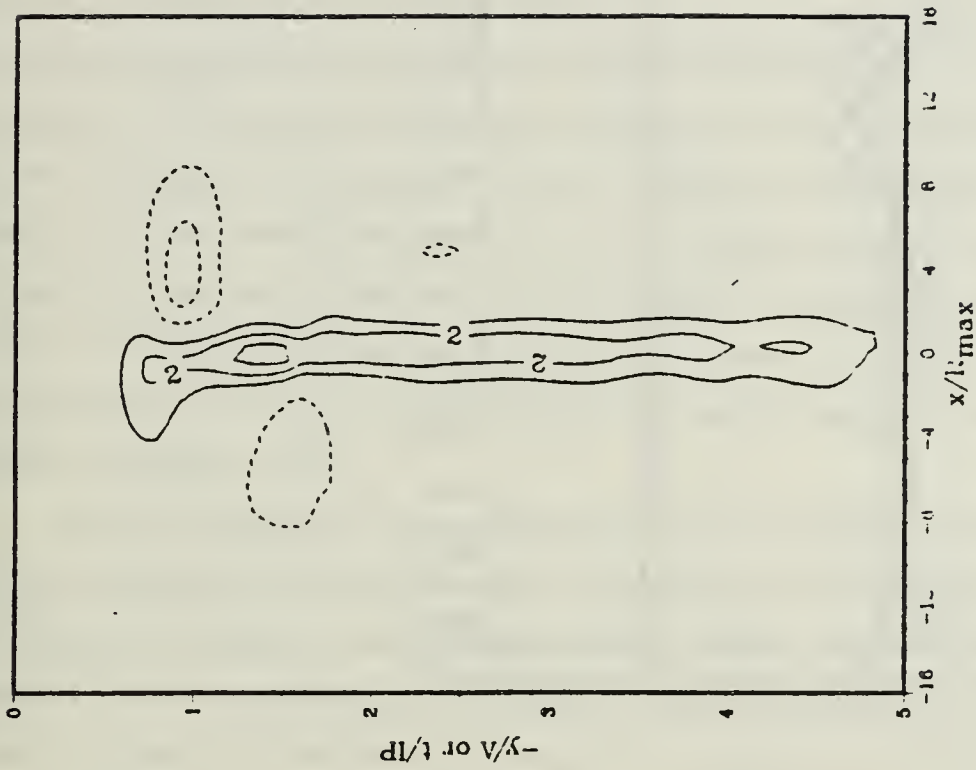
Figure 6.9 Mean simulated v-component (left) (cm/s) and nondimensional contours of f_{eff}(x100) at 25 m based on a running mean over an inertial wavelength. The axes are nondimensionally scaled in terms of R_{max} (30 km) and Λ (580 km) with the storm center now at (0,-1).
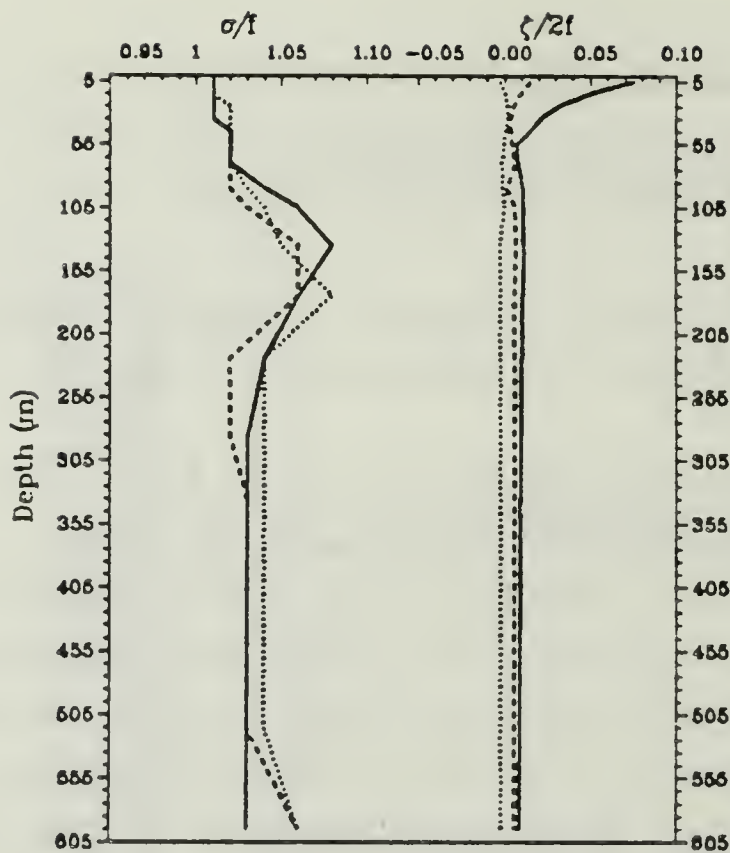
Figure 6.10 Vertical profiles of the normalized diagnosed frequencies σ/f (left) and the f_{eff} (right) at $x=0$ (solid), $x=2R_{max}$ (dotted) and $x=4R_{max}$ (dashed) based on simulated velocities from the 17-level model.

technique is similar to that used in Section 4.2 for the observations, except that the data are filtered using a simple running inertial period, rather than the Lanczos filter used in the observations. This change in the technique is necessary because the simulated time series only extends for 5 IP.

1. CW-rotating amplitudes

Since the demodulation process yields four amplitudes (cosine and sine for each velocity component), the CW-rotating amplitudes (Fig. 6.11) can be obtained following the treatment by Gonella (1972) and Mooers (1973). As expected, the largest CW-rotating amplitudes are to the right of the track in the upper ocean and exceed 100 cm/s in the mixed layer (Fig. 6.11a). The amplitudes decrease over e-folding scales of 2-3 IP, which agrees with the observations (see Fig. 4.5). For example, the maximum amplitudes in the mixed layer at CMA3 were about 85 cm/s after removal of the surface wave velocity components. Thus, there is fairly good agreement between the CW-rotating amplitudes in the upper ocean between the observations and the model.

At 70 m (Fig. 6.11b), the maximum CW-rotating amplitudes are about 50-60 cm/s, or about half the amplitude in the mixed layer. There is also a shift of about an IP between the maximum CW-rotating amplitudes in the mixed layer and thermocline. This time shift suggests a phase tilt with depth that is expected for vertical energy propagagtion. These amplitudes substantially agree with the amplitudes of 18-22 cm/s observed at 250 and 440 meters at CMA3. In the deep layers (Fig. 6.11c and d), there is a fairly signficant amplitude of 16-18 cm/s in the near-inertial frequency band! Presumably, these large amplitudes are due to the free-surface boundary condition. The CCW-rotating amplitudes are 2-8 cm/s (not shown) and when combined with the CCW amplitudes form near-inertial ellipses that enable energy to propagate vertically (LeBlond and Mysak, 1978).

The four amplitudes are combined to form the characteristics of the CW-rotating amplitudes and phases for direct comparison to the observations. In the mixed layer, the amplitudes and phases are fairly close. However, the simulated amplitude in the thermocline (180 m) is only 4 cm/s as compared to 15 cm/s observed at CMA2. There is a node point in the mode 1 amplitude (see Fig. 6.1) which may account for a large percentage of the difference. The observations and model near-inertial currents do seem to be in phase at 180 m. At 285 m, the model amplitudes are about 5 cm/s less than those observed and there is a difference in phase of about 100 °. However, the amplitudes at 435 m are underestimated, but the phases are within 2 °. Some of the discrepancies at these two levels have to be attributed to the sloping bottom, although the phases at the bottom are nearly equal. Although the model simulations have slightly less amplitude than the observations, it is encouraging that the model does predict significant currents below 200 m!

2. Modal Analyses

The simulated velocities in the near-inertial wave band are then least-squares fit (Fig. 6.12) to the barotropic mode (not shown) and first three baroclinic modes in Fig. 6.2. Notice that there is indeed a barotropic component of 4-6 cm/s within the near-inertial band, which agrees fairly well with the depth-averaged component estimated from the moored current meter arrays of 7-10 cm/s (see Fig. 4.12). Moreover, the mode 1 amplitudes along $x = 4R_{max}$ (Fig. 6.12b) is a maximum of about 30 cm/s as compared to 24 cm/s in the observations. The second baroclinic mode amplitudes (Fig. 6.12c) are also within 3-4 cm/s of the those estimated from the fits to the observational analyses. Unfortunately, the mode 3 amplitude could not be resolved
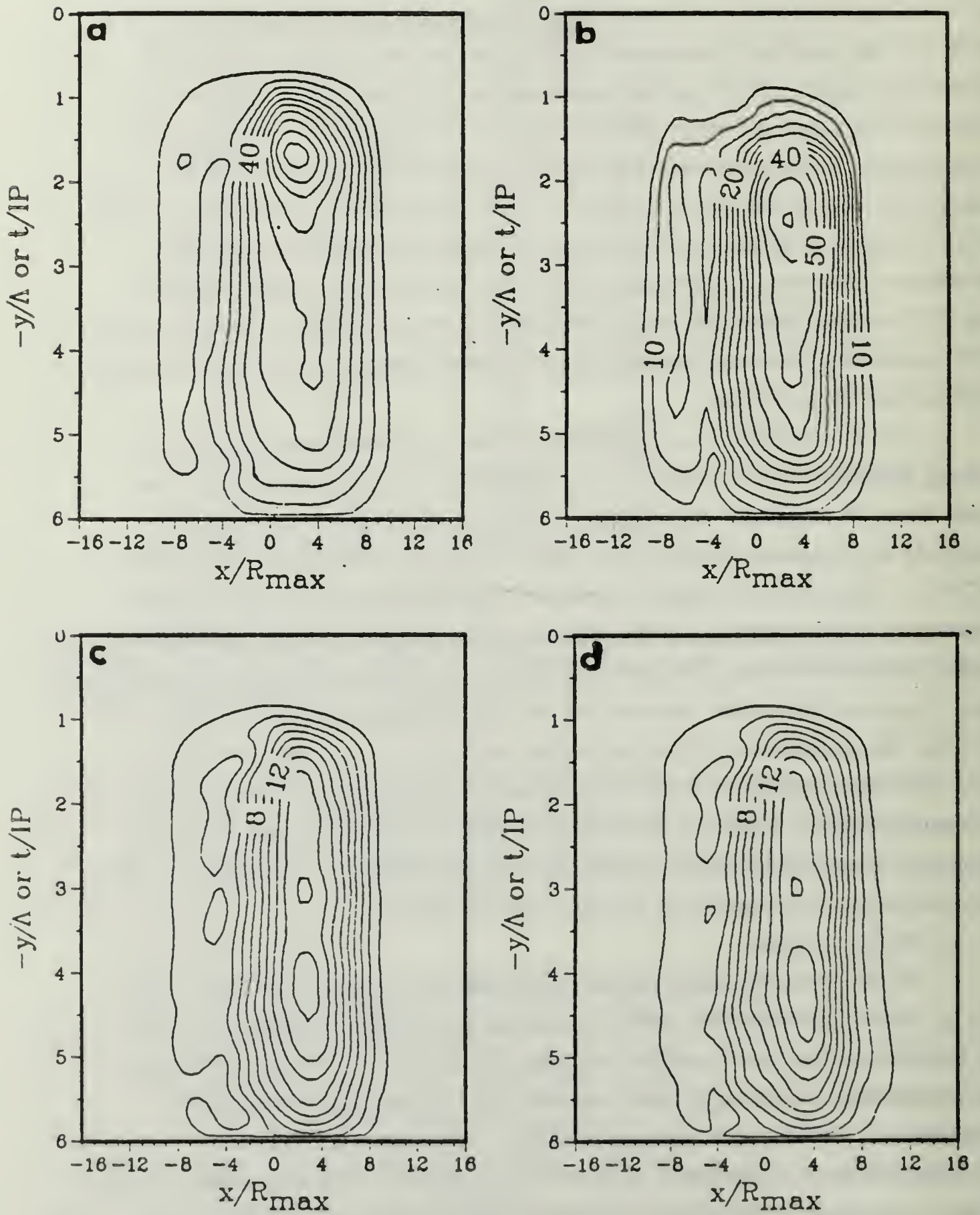
Figure 6.11 CW-rotating amplitudes from the simulated, demodulated velocities (cm/s) for the a) 25 m, b) 70 m, c) 285 m and d) 435 m. The axes are scaled as in Fig. 6.9 with storm center at (0,-1).

TABLE 17

Comparisons of the CW-rotating amplitudes and phases
between the Frederic observations and model simulations based on a 5 IP
average.

Depth	Observed		Model	
	CW	Θ	CW	Θ
(m)	(cm/s)	(°)	(cm/s)	(°)
25	70	142	60	104
175	15	-103	4	-131
285	20	27	14	-74
435	19	-69	14	-71

with the limited vertical sampling by the current meter moorings. However, the model suggests that the third baroclinic mode amplitudes are 4-6 cm/s.

E. SUMMARY

The simulated near-inertial response to a hurricane-like wind stress has very similar characteristics to the observations acquired in Frederic. For example, there is a blue-shift in the frequencies of the waves of 1-8% above f. It appears that the vorticity of the mean flow is not responsible for the frequency shifts. The mean (time) flows set up by the hurricane have similar magnitudes in the model and observations. The CW-rotating amplitudes throughout the water column also have similar magnitudes which is especially apparent in the near-bottom amplitudes of 16-20 cm/s.

The free surface slope that is induced by mean divergence of the currents excites a depth-independent component in the near-inertial frequency band. This barotropic component has amplitudes of 4-6 cm/s compared to 7-10 cm/s derived from the observations. Furthermore, the amplitudes of the first two baroclinic modes are within 3-5 cm/s of those estimated from the least-squares fits. Thus, it appears that the free surface model is simulating realistic ocean currents in response to strong atmospheric forcing.
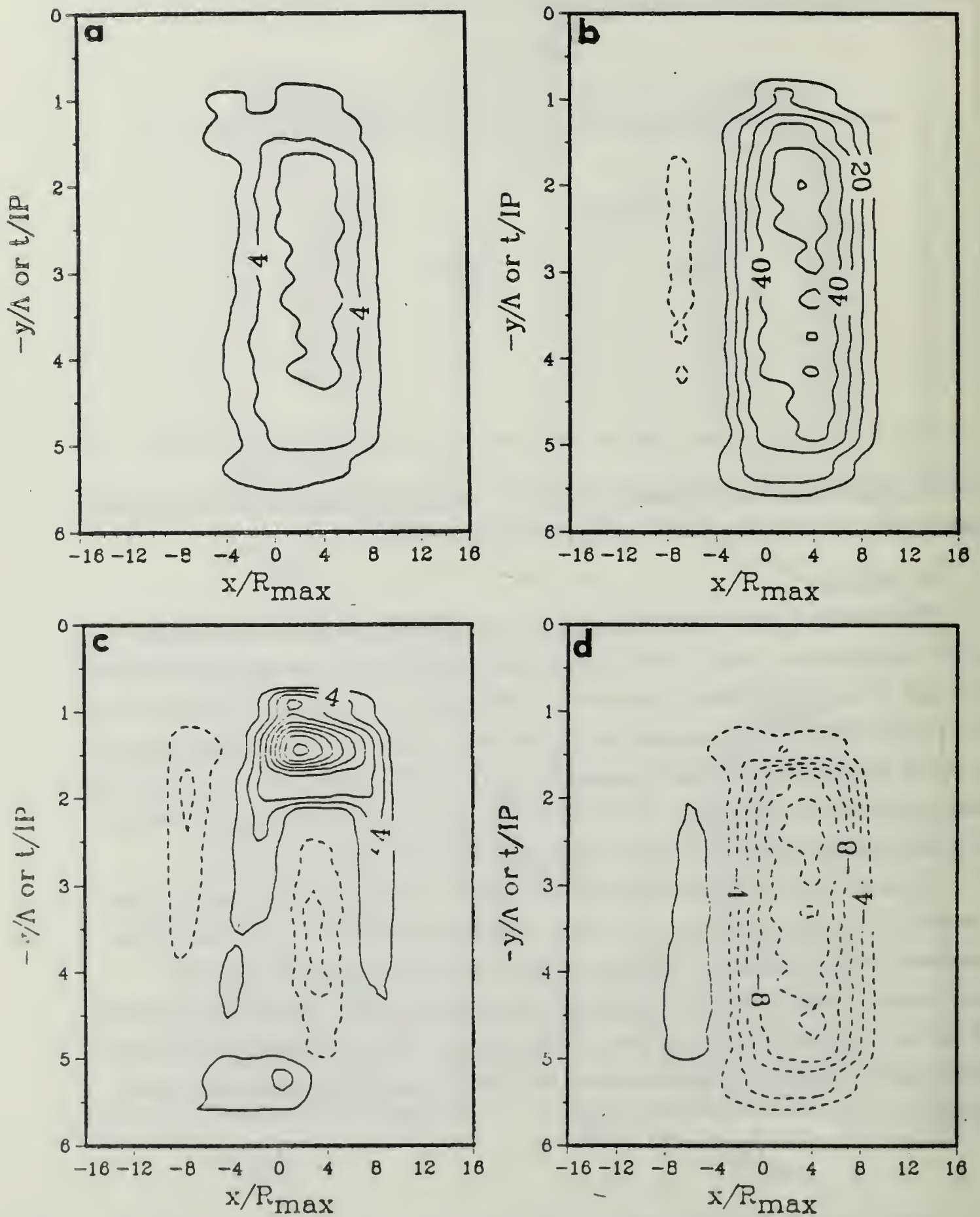
Figure 6.12 Velocity coefficients from the simulated, demodulated velocities (cm/s) for the a) barotropic mode, b) mode 1, c) mode 2 and d) mode 3. The axes are scaled as in Fig. 6.9 with storm center at (0,-1).

VII. CONCLUSIONS

The ocean current data collected during and subsequent to the passage of hurricane Frederic represented a unique opportunity to study the time evolution of the forced three-dimensional response. The Frederic data set included sufficient spatial and temporal sampling to understand the low-mode (large vertical wavelength) near-inertial response. A striking feature was the fairly good agreement in the near-inertial amplitudes with the time scales for the first two baroclinic modes as predicted from a linear, inviscid model (Gill, 1984). For instance, the first baroclinic mode maxima occurred within an IP and decreases rapidly as energy is propagated out of the source region in the mixed layer. A secondary increase in mode 1 amplitude at about 3-4 IP corresponds to the predicted time for the first mode to become in-phase with the higher order modes. This secondary increase in the mixed layer amplitudes about 3-4 IP following storm passage at the arrays also agrees with the numerical simulations of Kundu and Thomson (1985). Secondary increases in the clockwise rotating, near-inertial amplitudes 7-8 IP after storm passage were associated with the second baroclinic mode in the thermocline and near-bottom layers. Amplitudes in the thermocline started to decrease substantially after 15 IP which is consistent with predictions from Gill's theory.

The explained variances associated with the first and second baroclinic modes were nearly equal at Current Meter Array CMA3 when averaged over 7-10 IP, whereas the second mode dominated the response at CMA2 by almost a factor of three. These differences can be explained in terms of the differences in the bottom topography at the arrays. The inclusion of the bottom slope in the normal mode decomposition of the current meter data affects of the baroclinic modes that can be resolved in the current meter data. The first baroclinic slope-mode explained about 45 % of the near-inertial variance or roughly 5 % more than the first baroclinic, flat-bottom mode. The amount of variance contributed by the second baroclinic mode was about 6 % above the variance explained in the flat-bottom case. These increases in the explained variances due to the inclusion of slope effects generally agree with those by Lai and Sanford (1986).

One of the significant features observed in all of the current meter measurements was a rapid current increase throughout the column. Bottom currents increased significantly in the DeSoto Canyon region and at the OTEC site within hours of the upper ocean response, which began roughly 9 h prior to the point of closest approach of hurricane Frederic in the DeSoto Canyon region. Brooks (1983) also observed an ocean response to 700 m during the passage of hurricane Allen. Thus, the Frederic data provide important confirmation that a deep ocean response occurs much more rapidly than had been previously predicted on theoretical grounds.

Perhaps the most controversial aspect of the Frederic moored current meter data is the appearance of the depth-averaged component. Because of limited vertical sampling, these estimates of the depth-averaged response to hurricane Frederic may be contaminated by aliasing of higher-order baroclinic modes. Nevertheless, the depth-averaged flow accounted for about 20 % of the near-inertial variance at all the sites over the first 10 IP. The initial increase in the depth-averaged current (8 cm/s) may have been associated with a free-surface slope since the current increases were detected to the bottom at all arrays. However, these initial increases in the depth-averaged current only account for 30 % of the observed variance. It is concluded that the depth-averaged currents of 7-10 cm/s in the Frederic moored current meter arrays are consistently too large to be an aliasing problem, and thus are likely to be a real physical aspect of the ocean response to hurricanes.

The linear, two-layer model of Geisler (1970) has been extended to include a continuously stratified fluid with the wind stress superposed onto the first five baroclinic modes (Kundu and Thomson, 1985). Expressions for the 3-dimensional velocity structure have been derived that include the wind stress curl, the stress divergence and Ekman-type terms. The model hurricane is a Rankine vortex based on observed storm parameters. The forcing functions for each mode are convolved with the Bessel function to determine the horizontal structure of the 3-dimensional velocity field. In general, the wind stress curl dominates the ocean current response. However, the Ekman and stress divergence terms that were not treated in Geisler (1970) contribute to the near-inertial response within the direct forcing regime. These terms dampen quickly within one or two wavelengths of the forced regime, whereas the curl has more of a persistent effect on the ocean response.

For the first time, the vertical structure of the ocean current and temperature response to the passage of major hurricanes has been mapped using AXCP

measurements (Sanford *et al.*, 1987). These experiments demonstrate that AXCP's can provide ocean current and temperature data under extreme conditions. In this research, the vertical structure of the near-inertial response to hurricane Norbert is isolated from the ocean current profiles by first subtracting a spatially-averaged mean. The near-inertial profiles are then fit to the first three or four forced baroclinic modes from the extension of Geisler's model. The forced, linear model explains over 70 % of the observed current variance in the right-rear quadrant of the storm with only the first four baroclinic modes. Near-inertial processes appear to contribute to an enhanced vertical shear feature observed near the base of the mixed layer in most of the profiles under the direct forcing of the hurricane. In terms of the energetics, the KE based on the simulated profiles represent the observed KE reasonably well (67-80 %) on the left side of the storm. Thus, the major portion of the vertical structure of the ocean current response can be represented by only three or four vertical modes. Mixing and nonlinear effects that have been neglected in this treatment may be important in some areas.

Hopkins (1982) had attempted to simulate the ocean response to hurricane Frederic with a rigid lid, baroclinic model. Although there was good agreement with the mixed layer currents, the currents in the thermocline were underestimated in comparison to the observations. To assess the relative role of the barotropic (depth-averaged) and baroclinic modes on the oceanic response to hurricane, the near-inertial response to a hurricane-like wind stress is isolated from numerical simulations from a free surface model (Chang, 1985). This is the first model that includes both the barotropic and baroclinic response to hurricane forcing. The maximum simulated currents are displaced between $r = 2\text{-}4R_{max}$ to the right of the storm track, which agrees with previous numerical studies. The wavelength of the forced waves is equal to the predictions from linear theory. Thus, the model simulations appear to have sufficient veracity to allow comparisons to observations. In the free surface model simulations, the near-inertial response is detected throughout the water column because the slope of the free surface induces a depth-independent response. Typical bottom amplitudes of the CW-rotating currents were 15 cm/s compared to 18 cm/s observed in Frederic. Using the same techniques used with the observations, the near-inertial amplitudes are fit to the first few vertical modes. The modal amplitude of the barotropic component is 4-8 cm/s as compared to the estimate of 7-10 cm/s derived from the observations. Thus, it is suggested that the simulated barotropic response

supports the observations of the depth-averaged response despite the limited vertical sampling in the moored current meter arrays. There is also considerable agreement with the maximum amplitudes of the first two baroclinic modes in the simulations.

The combination of moored current meters to provide the detailed time evolution and the AXCP's to describe the instantaneous vertical structure in great detail has been very effective in increasing our understanding of the ocean response to hurricane forcing. It is particularly satisfying that the theoretical treatments agree in so many aspects with the observed time evolution and the vertical structure, including (for the first time) the forced response under hurricane Norbert. Simulations with realistic forcing provide a more complete three-dimensional and time-dependent representations of the ocean response. Applying the same analysis techniques as used in the observational data results in a satisfactory confirmation of many aspects of the ocean response. Thus, we have considerable confidence that a correct representation of the vertical structure of the ocean response has been derived from the sparse moored current meter and AXCP observations.

APPENDIX A
THREE-DIMENSIONAL VELOCITIES

1. VERTICAL VELOCITY

The vertical velocity horizontal structure function will be treated first because of it's implications with upwelling and downwelling regimes in the wake of a moving tropical cyclone. Differentiating (3.10) with respect to time and multiplying (3.11) by the Coriolis parameter f and adding yields:

$$\mathscr{L}_1 u_n = -\frac{\partial^2 p_n}{\partial x \partial t} + f\frac{\partial p_n}{\partial y} + \frac{\partial X_n}{\partial t} + fY_n$$

where

$$\mathscr{L}_1 = \frac{\partial^2}{\partial t^2} + f^2,$$

The corresponding equation for the v-component is given by:

$$\mathscr{L}_1 v_n = -\frac{\partial^2 p_n}{\partial y \partial t} - f\frac{\partial p_n}{\partial x} + \frac{\partial Y_n}{\partial t} - fX_n.$$

Without loss of generality, equation 3.15 can be operated on by $\mathscr{L}_1$

$$\mathscr{L}_1 c_n^2 \left\{ \frac{\partial u_n}{\partial x} + \frac{\partial v_n}{\partial y} \right\} + \mathscr{L}_1 \frac{\partial p_n}{\partial t} = 0$$

and because the problem is linear, the differentials can be rearranged

$$c_n^2 \left[\frac{\partial}{\partial x}\left(\mathscr{L}_1 u_n \right) + \frac{\partial}{\partial y}\left(\mathscr{L}_1 v_n \right) \right] + \frac{\partial}{\partial t}\left(\mathscr{L}_1 p_n \right) = 0 .$$

After differentiating and combining the terms, and dividing by c_n^2 the expression becomes

$$-\frac{\partial}{\partial t}\left\{ \nabla^2 p_n - \frac{1}{c_n^2} \mathscr{L}_1 p_n \right\} - f\nabla \times \tau_n - \frac{\partial}{\partial t}\nabla \cdot \tau_n$$

where ∇^2 is the horizontal Laplacian given by

$$\nabla^2 = \frac{\partial^2}{\partial x^2} + \frac{\partial^2}{\partial y^2}$$

and $\nabla \times \tau_n = \partial Y_n/\partial x - \partial X_n/\partial y$ and $\nabla \cdot \tau_n = \partial X_n/\partial x + \partial Y_n/\partial y$ which represent the wind stress curl and divergence, respectively. Substituting for the pressure term from (3.15), the governing equation for the vertical velocity for the nth baroclinic mode becomes

$$c_n^2 \left\{ \frac{\partial^2}{\partial x^2} + \frac{\partial^2}{\partial y^2} - \frac{1}{c_n^2}\frac{\partial^2}{\partial t^2} - \alpha_n^2 \right\} w_n = f\nabla \times \tau_n + \frac{\partial}{\partial t}\nabla \cdot \tau_n , \qquad (A.1)$$

135

where $\nabla \times \tau_n = \partial Y_n/\partial x - \partial X_n/\partial y$ and $\nabla \cdot \tau_n = \partial X_n/\partial x + \partial Y_n/\partial y$. Equation (A.1) is analogous to equation (10) in Geisler (1970) except that the phase speed (c_n) and the inverse deformation radius (α_n) are for the nth mode.

2. HORIZONTAL VELOCITY

The spatial distribution of the horizontal velocity eigenfunctions is sought using (3.10),(3.11) and (3.15) (Longuet-Higgins, 1965). Differentiate equations (3.10 and 3.11) with respect to time and substitute for pressure from (3.15):

$$\frac{\partial^2 u_n}{\partial t^2} - f\,\frac{\partial v_n}{\partial t} = -c_n^2\,\frac{\partial}{\partial x}\left[\frac{\partial u_n}{\partial x} + \frac{\partial v_n}{\partial y}\right] + \frac{\partial X_n}{\partial t} \qquad , \qquad (A.2)$$

$$\frac{\partial^2 v_n}{\partial t^2} + f\,\frac{\partial u_n}{\partial t} = -c_n^2\,\frac{\partial}{\partial y}\left[\frac{\partial u_n}{\partial x} + \frac{\partial v_n}{\partial y}\right] + \frac{\partial Y_n}{\partial t} \qquad , \qquad (A.3)$$

A vorticity equation is formed by cross differentiating equations (A.2) and (A.3)

$$\frac{\partial^2}{\partial t^2}\left\{\frac{\partial v_n}{\partial x} - \frac{\partial u_n}{\partial y}\right\} + f\,\frac{\partial}{\partial t}\left[\frac{\partial u_n}{\partial x} + \frac{\partial v_n}{\partial y}\right] = \frac{\partial}{\partial t}\left\{\frac{\partial Y_n}{\partial x} - \frac{\partial X_n}{\partial y}\right\} \qquad (A.4)$$

and solving for v_n yields

$$\frac{\partial^2}{\partial t^2}\frac{\partial v_n}{\partial x} + f\left[\frac{\partial}{\partial t}\frac{\partial v_n}{\partial y}\right] = \frac{\partial^2}{\partial t^2}\frac{\partial u_n}{\partial y} - f\left[\frac{\partial}{\partial t}\frac{\partial u_n}{\partial x}\right] + \frac{\partial}{\partial t}\left[\frac{\partial X_n}{\partial x} - \frac{\partial Y_n}{\partial y}\right] \qquad . \qquad (A.5)$$

Next, take the partial with respect to time of (A.2) and add it to the product of Coriolis parameter and (A.3) to form

$$\frac{\partial}{\partial t}\mathscr{L}_1 u_n = c_n^2\,\frac{\partial}{\partial x}\frac{\partial}{\partial t}\left[\frac{\partial u_n}{\partial x} + \frac{\partial v_n}{\partial y}\right] + fc_n^2\left[\frac{\partial}{\partial y}\left[\frac{\partial u_n}{\partial x} + \frac{\partial v_n}{\partial y}\right]\right]$$

$$+ \frac{\partial^2 X_n}{\partial t^2} + f\,\frac{\partial Y_n}{\partial t} \quad ,$$

and taking the partial once more with respect to time and substituting (A.4) for v_n forms an equation with only one unknown

$$\frac{\partial^2}{\partial t^2}\mathscr{L}_1 u_n = c_n^2\left[\frac{\partial^2}{\partial t^2}\nabla^2 u_n\right] + c_n^2\left\{\frac{\partial}{\partial t}\frac{\partial}{\partial y}\nabla \times \tau_n\right\} + \frac{\partial^2}{\partial t^2}\left[\frac{\partial X_n}{\partial t} + fY_n\right] \quad ,(A.6)$$

Dividing by c_n^2 and integrating twice with respect to time forms

$$\frac{1}{c_n^2}\mathscr{L}_1 u_n - \nabla^2 u_n = \frac{\partial}{\partial y}\left\{\int \nabla \times \tau_n dt\right\} + \frac{1}{c_n^2}\left[\frac{\partial X_n}{\partial t} + fY_n\right] \quad ,(A.7)$$

Equation A.7 can then be simplified further invoking the steady-state and transforming into the coordiate system defined in Chapter III. Thus, the governing equation for the horizontal structure of the u-component is

$$\mathcal{L}_2 u_n = - \frac{1}{U_h \alpha_n^2} \nabla \times \tau_n + \frac{1}{f^2}(fY_n - U_h \frac{\partial X_n}{\partial y}) \tag{A.8}$$

and the governing equation for the v-component is developed in a similar manner

$$\mathcal{L}_2 v_n = \frac{1}{U_h \alpha_n^2} \int \frac{\partial}{\partial x} \nabla \times \tau_n dy \quad \frac{1}{f^2}(fX_n + U_h \frac{\partial Y_n}{\partial y}) \tag{A.9}$$

In these equations, the second terms represent those components that are driven by the wind stress, Y_n/f and $-X_n/f$ or the Ekman type velocities. The third terms in the u and v equations represent a sink of vorticity and the y-component of the divergence, respectively. Similarly, the effect of the divergence term is to augment the curl term because the minus sign makes the term of the same sign.

APPENDIX B
HYPERBOLIC OPERATOR

The inversion of the integral (page 53) yields a fundamental solution or a Green's function (Stakold, 1979). The double integral (INT) is given by

$$INT = \frac{1}{4\pi^2} \int_{-\infty}^{\infty}\int \frac{1}{(k^2-l^2+1)} e^{-ikx'}e^{-ily'} dk\ dl$$

as defined in the Chapter III above. This integral can be recast into the cosine transforms

$$INT = \frac{1}{\pi^2} \int_{0}^{\infty}\int \frac{1}{(k^2-l^2+1)} \cos(kx')\cos(ly')\ dk\ dl .$$

or

$$INT = \frac{1}{\pi^2} \int_{0}^{\infty} \left[\int_{0}^{\infty} \frac{\cos(ly')}{(k^2+1)-l^2}\ dl \right] \cos(kx')\ dk .$$

The transform in brackets is given by

$$\int_{0}^{\infty} \frac{\pi}{2}\ \frac{1}{(k^2+1)} \sin(\sqrt{(k^2+1)}\ y')$$

(Erdelyi et al., 1954) which renders the integral equation as

$$INT = \frac{1}{2\pi} \int_{0}^{\infty} \frac{\sin(\sqrt{(k^2+1)}\ y')}{(k^2+1)} \cos(kx')\ dk .$$

This inverse transform can be found in Erdelyi et al., (1954) as

$$\frac{\pi}{2} J_0((y'^2-x'^2)^{1/2})$$

where J_0 represents the zero order Bessel function. Thus the inversion of the transform yields

$$INT = \frac{J_0}{4} ((y'^2-x'^2)^{1/2}) .$$

The Bessel function of order 0 is the fundamental solution (Green's function) to the integral equation which is valid for $0 < x' < y'$. In terms of the atmospheric scaling ($2R_{max}$), the inverse transform is

$$INT = \frac{J_0}{2} ((y'^2-x'^2)^{1/2}) .$$

APPENDIX C
ERROR ANALYSIS

The amount of aliasing of low-mode, baroclinic energy by limited vertical sampling is addressed using the predicted currents from a 15-level, primitive equation model (Adamec *et al.*, 1981). The model is externally forced by a fast-moving hurricane (8.5 m/s) and integrated over 3 IP. Since the storm speed exceeded the first baroclinic mode phase speed (3 m/s), a baroclinic response is expected (Geisler, 1970). A rigid lid is imposed in the model and the vertically-averaged flow is required to be zero at each grid point. The variance reduction method was performed on the depth-time series over 3 IP in the near-inertial frequency band. A depth series containing the real part of the velocity was formed prior to the modal decomposition.

To assess the amount of bias due to limited vertical sampling, the depth series was vertically averaged using all the 15 and only 3 levels of data respectively. Using 15 levels, the depth-averaged, near-inertial component was about 3 cm/s. Thus, this depth-averaged component is assumed to be correct since the model requirement of a zero vertical average is valid only over the total frequency range. The depth series was subsampled at levels that correspond to the current meters on the NAVOCEANO arrays (3 levels). The depth-averaged, near-inertial component was 1 cm/s or a change of 2 cm/s from the 15 level case. Thus, limited vertical sampling induces a 2 cm/s bias in the estimation of the depth-averaged current.

A depth-averaged component is subtracted from the near-inertial profile prior to least-squares fitting of the first two baroclinic modes. The first mode coefficient in the 15-level case was 17 cm/s as compared to 23 cm/s for the 3-level experiment. Thus, the bias in the first mode amplitude due to limited vertical sampling is about 6 cm/s. The second baroclinic mode amplitudes were 14 and 10 cm/s for the 15 and 3-level experiments, respectively. Thus, the bias in amplitude with only 3 observation levels is approximately 4 cm/s for the second baroclinic mode. It should also be noted that first baroclinic mode was overestimated and the second mode coefficient was underestimated due to limited vertical sampling. The total amount of energy in the vertical average and first two modes was conserved in both experiments. In summary, the biases of this magnitude in the depth-averaged and first two baroclinic mode amplitudes are not large enough to negate the conclusions of this study. It is

concluded that Frederic excited a non-zero depth-averaged component and energetic baroclinic modes 1 and 2 that have been inferred from the limited ocean current data.

140

LIST OF REFERENCES

Adamec, D., R. L. Elsberry, R. W. Garwood, Jr. and R. L. Haney, 1980: An embedded mixed-layer ocean circulation model. *Dyn. of Atmos. and Oceans, 6,* 69-96.

Anderson, D. L. T., and A. E. Gill, 1979: Beta-dispersion of inertial waves. *J. Geophys. Res., 84,* 1836-1842.

Arfken, G., 1970: *Mathematical Methods for Physicists.* Academic Press, New York, 815 pp.

Beardsley, R.C., W. Boicourt, L. C. Huff and J. Scott, 1977: CMICE 76 : A current meter intercomparison off Long Island in February-March 1976. Report no. 77-62, Woods Hole Oceanographic Institution, Woods Hole, MA 02543, 123 pp.

Black, P. G., 1983: Ocean temperature changes induced by tropical cyclones. Ph. D. dissertation, The Pennsylvania State Univ., State College, PA 16802, 278 pp.

_____, R. L. Elsberry, L. K. Shay, R. Partridge and J. Hawkins, 1987 : Hurricane Josephine surface winds and ocean response determined from air-deployed drifting buoys and concurrent research aircraft data. *J. Atmos. and Oceangr. Tech.* (accepted)

Brooks, D., 1983: The wake of hurricane Allen in the western Gulf of Mexico. *J. Phys. Oceanogr., 13,* 117-129.

Chang, S. W., 1985: Deep ocean response to hurricanes as revealed by an ocean model with a free-surface. Part I: axisymmetrical case. *J. Phys. Oceanogr. 15,* 1847-1858.

_____, and R. A. Anthes, 1978: Numerical simulations of the ocean's nonlinear, baroclinic response to translating hurricanes. *J. Phys. Oceanogr., 8,* 468-480.

Daddio, E., W. J. Wiseman Jr. and S. P. Murray, 1978: Inertial currents over the inner shelf near 30 N. *J. Phys. Oceanogr. 8,* 728-733.

D'Asaro, E., 1984: Wind-forced internal waves in the North Pacific and Sargasso Sea. *J. Phys. Oceanogr., 14,* 781-794.

_____, 1985: Upper ocean temperature structure, inertial currents, and Richardson numbers observed during strong meteorological forcing. *J. Phys. Oceanogr., 15,* 943-962.

Doodson, A. T., and H. D. Warburg, 1941: *Admiralty Manual of Tides.* Her Majesty's Stationery Office, London, England, 270 pp.

Effrom, B., and G. Gong, 1983: A leisurely look at the bootstrap, jacknife and cross-validation. *Amer. Statist., 37,* 36-48.

141

Elsberry, R. L., T. Fraim, and R. Trapnell, 1976: A mixed layer model of the ocean thermal response to hurricanes. *J. Geophys. Res.*, *81*, 1153-1162.

Erdelyi, A., W. Magnus, F. Oberhettinger, and F. G. Tricomi, 1954: *Tables of Integral Transforms, Vol. I*. McGraw-Hill, New York, 391pp.

Fjeldstad, J. E., 1958: Ocean current as an initial problem. *Geophysiske Pub.*, *20*, 1-24.

Fofonoff, N. P., 1969: Spectral characteristics of internal waves in the ocean. *Deep-Sea Res.*, Suppl. 16, 59-71.

_____, and Y. Ercan, 1967: Response characteristics of a savonius rotor current meter. Report no. 67-33,Woods Hole Oceanographic Institution, Woods Hole, MA 02543, 36 pp.

Gaul, R. D., 1967: Circulation over the continental margin of the northeast Gulf of Mexico. Report no. 286-d, Texas A&M University, College Station, TX 77843, 116 pp.

Garrett, C. R., and W. Munk, 1972: Space-time scales of internal waves. *Geophys. Fluid Dyn.*, *3*, 225-264.

_____,_____, 1975: Space-time scales of internal waves- a progress report. *J. Geophys. Res.*, *80*, 291-297.

Garwood, R. W., Jr., 1977: An oceanic mixed-layer model capable of simulating cyclic states. *J. Phys. Oceanogr.*, *7*, 455-468.

Geisler, J. E., 1970: Linear theory on the response of a two layer ocean to moving hurricane. *Geophys. Fluid Dyn.*, *1*, 249-272.

Gerald, C. F., 1983: *Applied Numerical Analysis*. Addison-Wesley, Reading, Massachusetts, 518 pp.

Gill, A. E, 1982: *Atmosphere-Ocean Dynamics*. Academic Press, New York, 662 pp.

_____, 1984: On the behavior of internal waves in the wakes of storms. *J. Phys. Oceanogr.,14*, 1129-1151.

Gonella, J., 1972: A rotary component method for analyzing meteorological and oceanographic time series. *Deep-Sea Res.*, *19*, 833-846.

Greatbatch, R. J., 1983: On the response of the ocean to a moving storm: the nonlinear dynamics. *J. Phys. Oceanogr.*, *13*, 357-367.

_____, 1984: On the response of the ocean to a moving storm: parameters and scales. *J. Phys. Oceanogr.*, *14*, 59-77.

Halpern, D., R. D. Pillsbury and R. L. Smith, 1974: An intercomparison of three current meters operated in shallow water. *Deep-Sea Res.*, *21*, 489-497.

Haltiner, G. J., and R. T. Williams, 1980: *Numerical Prediction and Dynamic Meteorology*. John Wiley and Sons, New York, New York, 477 pp.

Haney, R. L., 1974: A numerical study of the response of an idealized ocean to large scale heat and momentum flux. *J. Phys. Oceanogr.*, *2*, 145-167.

Hasselman, K., 1970: Wave driven inertial oscillations. *Geophys. Fluid Dyn.*, *1*, 463-502.

Hebert, P., 1979: Preliminary report: hurricane Frederic Aug 29 - Sept. 14,1979. NOAA National Hurricane Center, Coral Gables, FL 33149, 10 pp.

Holland, G. J., 1987: Mature structure and structure change. *Chap. 2, A Global View of Tropical Cyclones*, R. L. Elsberry, ed., Univ. of Chicago Printing Press, 13-50.

Hopkins, C., 1982: Ocean response to hurricane forcing. M. S. Thesis, Naval Postgraduate School, Monterey, CA 93943, 89 pp.

Johnson, A., and S. Renwick, 1981: Buoy observations during the passage of hurricane Frederic 1979. Data Report, NOAA Data Buoy Office, NSTL Station, MS 39529, 28 pp.

Kase, R. H., and D. J. Olbers, 1979: Wind driven inertial waves observed during phase III of GATE. *Deep-Sea Res.*, *261*, 191-216.

Krauss, W., 1972: Wind generated internal waves and inertial period motion. *Dtsch. Hydrogr. Z.*, *25*,241-250.

Kuo, H.-H., and T. Ichiye, 1977: A numerical study of the response of a barotropic ocean to a moving hurricane. *Tellus*, *29*, 561-571.

Kundu, P. K., and R. E. Thomson, 1985: Inertial oscillations due to a moving front. *J. Phys. Oceanogr.*, *15*, 1076-1084.

Kunze, E., 1985: Near-inertial wave propagation in geostrophic shear. *J. Phys. Oceanogr.*, *15*, 544-565.

Lai, D., and T. B. Sanford, 1986: Observations of hurricane generated slope modes. *J. Phys. Oceanogr.*, *16*, 657-666.

Large, W., and S. Pond, 1981: Open ocean momentum flux measurements in moderate to strong winds. *J. Phys. Oceanogr.*, *11*, 324-336.

Leaman, K. D., 1976: Observations on the vertical polarization and energy flux of near-inertial waves. *J. Phys. Oceanogr.*, *6*, 894-908.

_____, and T. B. Sanford, 1975: Vertical energy propagation of inertial waves - a vector spectral analysis of velocity profiles. *J. Geophys. Res.*, *80*, 1975-1978.

Leblond, P. H., and L. A. Mysak, 1978: *Waves in the ocean.* Elsevier, Amsterdam, 638 pp.

Leipper, D., 1967: Observed ocean conditions and hurricane Hilda, 1964. *J. Atmos. Sci.*, *24*, 182-196.

Longuet-Higgins, M. S., 1965: The response of a stratified ocean to a stationary or moving wind systems. *Deep Sea Res.*, *12*, 923-973.

Lighthill, M. J., 1967: On waves generated in dispersive systems by travelling forcing effects with applications to the dynamics of rotating fluids. *J. Fluid Mech.*, *27*, 725-752.

Madala, R. V., and S. A. Piacsek, 1977: A semi-implicit numerical model for baroclinic oceans. *J. Comp. Phys.*, 23, 167-178.

Mayer, D., M. O. Mofjeld and K. D. Leaman, 1981: Near-inertial internal waves on the outer shelf in the middle Atlantic Bight in the wake of hurricane Belle. *J. Phys. Oceanogr.*, *11*, 86-106.

Molinari, R. L., and D. A. Mayer, 1982: Current meter observations on the continental slope at two sites in the eastern Gulf of Mexico. *J. Phys. Oceanogr.*, *12*, 1480-1492.

Mooers, C. N. K., 1973: A technique for the cross spectrum analysis of complex valued time series with emphasis on properties of polarized components and rotational invariants. *Deep-Sea Res.*, *20*, 1129-1141.

_____, 1975: Several effects of a baroclinic current on the cross-stream propagation of inertial-internal waves. *Geophys. Fluid Dyn.*, *6*, 245-275.

Morse, P. M. and H. Fesbach, 1953: *Methods of Theoretical Physics.* McGraw-Hill Book Company Inc., New York, 1978 pp.

Munk, W., 1981: Internal waves and small scale processes. *Evolution of Physical Oceanography: Scientific Surveys in honor of Henry Stommel*, C. Wunsch, ed., The MIT press, 264-291.

O'Brien, J., and R. O. Reid, 1967: The nonlinear response of a two layer baroclinic ocean to a stationary, axially-symmetric hurricane, I: Upwelling induced by momentum transfer. *J. Atmos. Sci.*, *24*, 208-215.

Otnes, R. K., and L. Enochson, 1978: *Applied Time Series Analysis.* Wiley-Interscience, New York, pp. 449.

Perkins, H., 1970: Inertial oscillations in the Mediterranean Sea. Ph.D. dissertation, Massachusetts Institute of Technology, Woods Hole Oceanographic Institution, Woods Hole, MA 02543, 123 pp.

Pollard, R. T., 1970: Surface waves with rotation: an exact solution. *J. Geophys. Res.*, *75*, 5895-5898.

_____, 1980: Properties of near-surface inertial oscillations. *J. Phys. Oceanogr.*, *10*, 385-398.

_____, P. B. Rhines, and R. Thompson, 1973: The deepening of the wind mixed layer. *Geophys. Fluid Dyn.*, *3*, 381-404.

Powell, M. D., 1982: The transition of the hurricane Frederic boundary-layer wind field from the open Gulf of Mexico to landfall. *Mon. Wea. Rev.*, *110*, 1912-1932.

Price, J. F., 1981: Upper ocean response to a hurricane. *J. Phys. Oceanogr.*, *11*, 153-175.

_____, 1983: Internal wave wake of a moving storm, Part I, Scales, energy budget and observations. *J. Phys. Oceanogr.*, *13*, 949-965.

_____, 1984: Internal wave wake of a moving storm. Part II, Parameters and scales. *submitted to J. Phys. Oceanogr.*

Robinson, E. A., and M. T. Silvia, 1981: *Digital foundation of time series analysis. Vol II: wave-equation, space-time processing.* Holden Day, San Francisco, CA, 534 pp.

Sanford, T. B., R. G. Drever, J. H. Dunlap and E. A. D'Asaro: 1982, Design, operation and performance of an expendable temperature and velocity profiler (XTVP). Applied Physics Lab., Univ. of Washington, APL-UW 8110., 83 pp.

_____, P. G. Black, J. Haustein, J. W. Fenney, G. Z. Forristall and J. F. Price, 1987:Ocean response to hurricanes, Part I: Observations. *J. Phys. Oceanogr. (in press)*

Schoenstadt, A. L., 1977: The effect of spatial discretization on the steady state and transient behavior of the dispersive wave equation. *J. Comp. Phys. 23*, 364-379.

Shay L. K., 1983: Observations of inertio-gravity waves in the wake of hurricane Frederic. M. S. Thesis, Naval Postgraduate School, Monterey, CA 93943, 120 pp.

_____,and R. L Elsberry, 1985: Effect of an initial current regime on the oceanic response to hurricanes. MMS Proceedings: Sixth Annual Gulf of Mexico Information Transfer Meeting, U. S. Dept. of Interior, Minerals Management Service.

_____, and R. L. Elsberry, 1987a: Near-inertial ocean current response to hurricane Frederic. *J. Phys. Oceanogr. 17*, 1249-1269.

_____, R. L. Elsberry and P. G. Black, 1987b: Vertical structure of the ocean current response to hurricanes. *submitted to J. Phys. Oceanogr.*

Stakold, I., 1979: *Green's Functions and Boundary Value Problems.* John Wiley and Sons, New York, 638 pp.

Starr, R. B., and G. A. Maul, 1982: Physical oceanographic observations in the eastern Gulf of Mexico 1979-1980 for a potential OTEC Site. NOAA Tech. Mem. ERL-AOML-50, Atlantic and Meteorological Laboratories, Miami, FL 33149, 205 pp.

Thomas, G. G., S. M. Minton and R. L. Molinari, 1979: Data from the Atlantic and Meteorological Laboratories OTEC Plant Site in the Gulf of Mexico. NOAA Tech. Mem. ERL-AOML-34, Atlantic and Meteorological Laboratories, Miami, FL 33149, 135 pp.

Wahl, R. J., and W. J. Teague, 1983: Estimation of Brunt-Väisälä frequencies from temperature profiles. *J. Phys. Oceanogr., 13*, 2236-2240.

Veronis, G., 1956: Partition of energy between geostrophic and non-geostrophic oceanic motions. *Deep Sea Res., 8*, 157-177.

Willoughby, H. E., F. D. Marks Jr. and R. W. Feinberg, 1984: Stationary and moving convective bands in hurricanes. *J. Atm. Sci., 41*, 3189-3211.

Withee, G. W., and A. Johnson, 1976: Data report: buoy observations hurricane Eloise (September 19 to October 11, 1975). U. S. Dept. of Commerce, NOAA, NSTL Station, MS, 21 pp.

Wunsch, C., 1968: On the propagation of internal waves up a slope. *Deep-Sea Res., 25*, 251-258.

_____, 1969: Progressive internal waves up a slope. *J. Fluid Mech., 35*, 131-144.

_____, and A. E. Gill, 1976: Observations of equatorially trapped waves in Pacific sea level variations. *Deep Sea Res.*, *23*, 371 - 390.

Zetler, B. D., and D. V. Hanson, 1972: Tides in the Gulf of Mexico. *Contributions in the Physical Oceanography of the Gulf of Mexico*, Vol. 2, L. R. A. Cappuro and J. L. Reid, *Eds.*, Gulf Publishing Company, Houston, TX 77001, 288 pp.

INITIAL DISTRIBUTION LIST

		No. Copies
1.	Defense Technical Information Center Cameron Station Alexandria, VA 22304-6145	2
2.	Library, Code 0142 Naval Postgraduate School Monterey, CA 93943-5002	2
3.	Professor Curt A. Collins, (Code 68Co) Department of Oceanography Naval Postgraduate School Monterey, CA 93943	1
4.	Professor Robert J. Renard, (Code 63Rd) Department of Meteorology Naval Postgraduate School Monterey, CA 93943	1
5.	Professor Russell L. Elsberry, (Code 63Es) Department of Meteorology Naval Postgraduate School Monterey, CA 93943	5
6.	Professor R. W. Garwood Jr., (Code 68Gd) Department of Oceanography Naval Postgraduate School Monterey, CA 93943	1
6.	Professor E. B. Thornton, (Code 68Tm) Department of Oceanography Naval Postgraduate School Monterey, CA 93943	1
7.	Professor R. T. Williams, (Code 63Wu) Department of Meteorology Naval Postgraduate School Monterey, CA 93943	1
8.	Professor A. L. Schoenstadt, (Code 53Zh) Department of Mathematics Naval Postgraduate School Monterey, CA 93943	1

9. Professor Robert L. Haney, (Code 63Hy)   1
    Department of Meteorology
    Naval Postgraduate School
    Monterey, CA 93943

10. Dr. Christopher N. K. Mooers   1
    Institute of Naval Oceanography
    Bldg. 1100
    NSTL Station, MS 39522

11. Dr. Peter G. Black   1
    Hurricane Research Divison
    NOAA/AOML
    15 Rickenbacher Causeway
    Miami, FL 33149

12. Dr. Simon Chang   1
    Atmospheric Sciences Group
    Space Sciences Div.
    Naval Research Lab.
    Washington, DC 20375

13. Dr. Tom B. Sanford   1
    University of Washington/Applied Physics Lab.
    1013 NE 40th St.
    Seattle, WA 98105

14. Dr. George Forristall   1
    Shell Development Company
    Box 481
    Houston, TX 77001

15. Dr. Andrew Willmott   1
    Department of Mathematics
    University of Exeter
    North Park Road
    Exeter EX4 4QE England

16. Dr. William Hart, Code 8000   1
    Naval Oceanographic Office
    NSTL Station
    Bay St. Louis, MS 39522

17. Mr. Lynn K. Shay, (Code 63Sh)   5
    Dept. of Meteorology
    Naval Postgraduate School
    Monterey, CA 93943

18. Director   1
    Naval Oceanography Division
    Naval Observatory
    34th and Massachusetts Avenue NW
    Washington, D.C. 20390

19.	Commander Naval Oceanography Command NSTL Station Bay St. Louis, MS 39522	1
20.	Commanding Officer Naval Oceanographic Office NSTL Station Bay St. Louis, MS 39522	1
21.	Commanding Officer Fleet Numerical Oceanography Center Monterey, CA 93940	1
22.	Commanding Officer Naval Ocean Research and Development Activity NSTL Station Bay St. Louis, MS 39522	1
23.	Commanding Officer Naval Environmental Prediction Research Facility Monterey, CA 93940	1
24.	Chairman, Oceanography Department U.S. Naval Academy Annapolis, MD 21402	1
25.	Chief of Naval Research 800 N. Quincy Street Arlington, VA 22217	1
26.	Office of Naval Research (Code 480) Naval Ocean Research and Development Activity NSTL Station Bay St. Louis, MS 39522	1
27.	Scientific Liaison Office Office of Naval Research Scripps Institution of Oceanography La Jolla, CA 92037	1
28.	Library Scrippps Institution of Oceanography P.O. Box 2367 La Jolla, CA 92037	1
29.	Library Department of Oceanography University of Washington Seattle, WA 98105	1

30. Library   1
    CICESE
    P.O. Box 4803
    San Ysidro, CA 92073

31. Library   1
    School of Oceanography
    Oregon State University
    Corvallis, OR 97331

32. Library   1
    Coastal Studies Institute
    Louisiana State University
    Baton Rouge, LA 70603

33. Commander   1
    Oceanographic Systems Pacific
    Box 1390
    Pearl Harbor, HI 96860

34. Commander (Air-370)   1
    Naval Air Systems Command
    Washington, D. C. 20360

35. Chief, Ocean Services Division   1
    NOAA
    8060 13th Street
    Silver Springs, MD 20910